3-10-2010

Positron Annihilation Ratio Spectroscopy (PsARS) Applied to Positronium Formation Studies

Robert C. Slaughter

POSITRON ANNIHILATION RATIO SPECTROSCOPY (PsARS) APPLIED TO POSITRONIUM FORMATION STUDIES

THESIS

Robert C. Slaughter, 2nd Lieutenant, USAF
AFIT/GNE/ENP/10-M07

DEPARTMENT OF THE AIR FORCE
AIR UNIVERSITY

AIR FORCE INSTITUTE OF TECHNOLOGY

Wright-Patterson Air Force Base, Ohio

The views expressed in this prospectus are those of the author and do not reflect the official policy or position of the United States Air Force, Department of Defense, or the United States Government.

AFIT/GNE/ENP/10-M07

POSITRON ANNIHILATION RATIO SPECTROSCOPY (PsARS) APPLIED TO POSITRONIUM FORMATION STUDIES

THESIS

Presented to the Faculty

Department of Engineering Physics

Graduate School of Engineering and Management

Air Force Institute of Technology

Air University

Air Education and Training Command

In Partial Fulfillment of the Requirements for the

Degree of Masters of Science

Robert C. Slaughter

2nd Lieutenant, USAF

March 2010

AFIT/GNE/ENP/10-M07

POSITRON ANNIHILATION RATIO SPECTROSCOPY (PsARS) APPLIED TO POSITRONIUM FORMATION STUDIES

Robert C. Slaughter
2nd Lieutenant, USAF

Approved:

	Date
Dr. Larry W. Burggraf, PhD (Chairman)	
Dr. James Petrosky, PhD (Member)	
Capt Benjamin Kowash, PhD (Member)	
Dr. Ioana Pavel, PhD (Member)	

Abstract

A Positron Annihilation of Radiation Spectrometer (PsARS) was developed and characterized. PsARS spectroscopy as well as digital Positron Annihilation Lifetime Spectroscopy (PALS) was applied to measure positronium formation on gold nanoparticles deposited through an evaporative method onto a thin capillary tube. This gold coated capillary tube was designed to be used for positronium lifetime studies in local electric field experiments. High local electric fields can polarize a positron-electron pair, which may result in an extended lifetime of the positron. These fields may be created through the interaction of an external electric field with silver nanoparticles deposited onto the surface of gold coated capillary tubes. The capability to control size and distribution of silver nanoparticles on such a surface is demonstrated. PsARS analysis of potassium dodecahydrododecaborate (dodecaborate) solutions was also performed to verify positronic dodecaborate species as well as potential positronium quenching.

To my beautiful bride to be

Acknowledgements

I want to thank my advisor Dr. Larry Burggraf for his motivation and never ending insight throughout this thesis experience. The countless number of extended conversations has lead me to a deeper understanding of the world around me. I want to thank my committee members Captain Benjamin Kowash and Dr. James Petrosky for their assistance throughout this thesis process. I also want to especially thank my other committee member Dr. Ioana Pavel and all of her students, for opening up her chemistry laboratory to me. Your continual shared expertise in a subject matter that I was not at all originally familiar with has greatly broadened my education. I also would like to especially thank Lt. Col Chris Williams for setting me up to hit the ground running on my thesis. Your time, assistance, and collaboration are insurmountably appreciated. Also, Mr. Eric Taylor who assisted me through a countless number of day to day technical issues, Dr. Michael Lindsay for his expertise regarding digital PALS and the opportunity to go TDY to Eglin AFB as well as present at the IEEE NSS.

I most certainly also am grateful for the AFIT clean room expertise of Mr. Rick Patton and Mr. Rich Johnson whose technical expertise on the AFIT SEM and plasma deposition systems were essential in order for this research project to come to fruition. For Dr. Daniel Felker for his expertise and oversight for experimentation within the chemical hood, and Lt. Nick Herr for sharing his hard earned expertise on the AFM machine.

I would also like to especially acknowledge Eglin AFRL Energetic Materials branch for their sponsorship, the Air Force Office of Scientific Research (AFOSR), and the Nation Nuclear Security Administer (NNSA) for their financial support of this research.

Robert Slaughter

Table of Contents

Page

List of Figures

Figure Page

Figure Page

Figure Page

Figure Page

List of Tables

POSITRON ANNIHILATION RATIO SPECTROSCOPY (PsARS) APPLIED TO POSITRONIUM FORMATION STUDIES

1 Introduction

1.1 Motivation

Positron Annihilation Spectroscopy (PAS) has been an effective experimental technique used for material characterization for several decades. The main techniques currently used in laboratories are Angular Correlation of Annihilation Radiation (ACAR), 1D or 2D Doppler Broadening of Annihilation Radiation (2D DBAR), Positron Annihilation Lifetime Spectroscopy (PALS), Positron Annihilation Induced Auger Spectroscopy (PAES), and Positron Annihilation Ratio Spectroscopy (PsARS). These experimental techniques have been used for a variety of military and civilian applications such as semiconductor defect studies [1] [2] [3], Positron Emission Tomography (PET) improvements [4], material defect characteristics of explosives [5], electronic surface structure analysis [2], and aging nuclear weapon stockpile characterizations [6].

At the Air Force Institute of Technology (AFIT) located at Wright Patterson Air Force Base, Ohio, a fast-fast coincidence PALS system as well as simultaneous ACAR and 2D DBAR capabilities have been developed [5] [7]. PALS measures the lifetime of a positron before it annihilates with electrons of a material. The positron lifetime decreases with increasing electron density, and increases with the onset of defects or voids within a material in which the positron resides. ACAR and 2D DBAR measure the energy and momentum of the positron-electron pair in the laboratory reference frame just prior to annihilation. At AFIT PALS, ACAR, and 2D DBAR have been applied to investigate radiation effects in semiconducting materials.

The knowledge base and expertise gained through this development, as part of an Air Force Office of Scientific Research (AFOSR) sponsored research program headed by Dr. Larry Burggraf, has lead the initiative to expand the current capability to include digital PsARS as well

as positronium lifetime analysis in electromagnetic fields. The study of positronium interactions in electromagnetic fields is essential in developing the expanding knowledge base necessary to assess the potential of antimatter applications, in particular the potential use of positrons as a gamma ray source for futuristic missile defense systems [8].

1.2 Overview

A Positron Annihilation of Radiation Spectroscopy (PsARS) system was assembled and characterized. PsARS is used to determine the 3γ/2γ annihilation radiation ratios of a material, an experimentally determined quantity that can be used for positronium, quasi-stable positron-electron pair, formation studies. Positronium formation can provide insight into several key material characteristics such as porosity and defect concentration. PsARS as well as digital PALS was then applied to measure positronium formation on gold nanoparticles deposited through an evaporative method onto a thin capillary tube. This gold coated capillary tube was designed to be used for positronium lifetime studies in high local electric fields. High electric field environments may be created through silver nanoparticle deposition onto the surface of these gold coated capillary tubes. The capability to control size and distribution of these nanoparticles is demonstrated. PsARS analysis of potassium dodecahydrododecaborate (dodecaborate) solutions was also performed to verify positronic dodecaborate species as well as potential positronium quenching.

A digital PsARS system was developed for material characterization. The PsARS system was constructed using a sodium-iodine (NaI) scintillating ring connected to six photomultiplier tubes (PMTs). These six PMTs were then connected to six XIA channels. These XIA channels were used to transform the current pulses produced from the PMT into a digital pulse. Due to the relative ratio of photon quanta resulting from positronium annihilation, 3γ/2γ annihilation

radiation ratios were used to determine ortho-positronium annihilation intensities. Ortho-positronium is a quasi-stable positron electron pair in the triplet state.

Ortho-positronium intensities can be used for characterization of all substances, in particular defects, voids, or local environmental factors such as pressure or electromagnetic fields. The photon annihilation counts corresponding to 3γ decay within an energy range of 130-380 keV were used to develop a coincident PsARS system. A known sample of copper was used for initial validation. Copper, similar to other single crystal metals, does not form positronium and therefore a 3γ/2γ of $\frac{1}{372}$ is expected. This $\frac{1}{372}$ ratio is the theoretically predicted and experimentally verified relative cross section for three-to-two quanta events for an incident positron. An additional non-coincident PsARS system was also developed. The non-coincident PsARS method uses the spectrum of counts in the 340-400 keV region (3γ counts) relative to 511 keV region (2γ counts), normalized to a copper sample.

These two PsARS methods, coincident and non-coincident, were also used for positronium annihilation studies in potassium dodecahydrododecaborate (dodecaborate) solutions. Previous PALS measurements indicate that dodecaborate demonstrated interesting interactions with positrons. In particular, PALS measurements were interpreted to conclude that above a 10^{-2} M concentration of dodecaborate, para-positronium was quenched. Para-positronium is a quasi-stable positron electron pair in the singlet state. Due to the short lifetime of para-positronium (120 ps), para-positronium quenching is a phenomena that is generally not observed in materials. Both coincident and non-coincident PsARS measurements were applied to investigate what further information regarding para-positronium quenching can be obtained through 3γ/2γ analysis. If ortho-positronium is quenched the 3γ/2γ should be significantly reduced with increasing dodecaborate concentration. If para-positronium is quenched the 3γ/2γ ratio should increase with dodecaborate concentration. PsARS measurements were also used to provide further evidence to support positronic dodecaborate formations [5] [9].

Additional PsARS experiments were conducted in order to determine the potential for positronium formation within silver nanoparticle arrays on gold coated capillary tubes. Silver nanoparticles may interact with external electric fields to produce large local field effects that may polarize positronium and consequently increase positronium lifetimes. Silver nanoparticles of approximately 10-15 nm in size were synthesized through a $AgNO_3$ and $NaBH_4$ solution. A Scanning Electron Microscope (SEM) and Atomic Force Microscope (AFM) were used to characterize how these silver nanoparticles could be distributed on the surface. For experimentation, a 100 nm layer of gold was evaporated onto the surface of a capillary tube constructed by Polymicro. Radioactive sodium-chloride was then evaporated on the inner surface, depositing small amounts of ^{22}Na, a β^+ (positron) emitter. PALS as well as PsARS measurements were taken to determine the amount of positronium formation on the surface. In particular PALS and PsARS measurements were used to determine the effectiveness of this gold coated capillary tube to in moderating positrons to energies favorable for positronium formation to occur within silver nanoparticle clusters located on the surface.

One intention of this ongoing research is to apply a voltage to the outer layer of the capillary tube with an intended array of silver nanoparticles on the surface. Electric fields, resulting from a potential difference between the vacuum chamber (ground) and capillary tube (approximately -1000 V), converge onto the small silver nanoparticles (15 nm) producing high local electric fields. These high local electric fields should polarize the positronium. Due to the increased separation of the positron and electron there may be an increase in the positron lifetime as measured through a PALS system, as well as a potential change to the $3\gamma/2\gamma$ ratio as measured through PsARS. These measurements could serve as experimental confirmation of theoretical predictions of positron lifetime extensions due to polarization resulting from applied external electromagnetic fields [10] [11].

The main objective of this research was to produce, calibrate and demonstrate functionality of a PsARS spectrometer and apply it to measure positronium formations. This research demonstrates the capability to deposit silver nanoparticle arrays on the surface of gold coated capillary tubing. As measured through PALS and PsARS, these gold coated capillary tubes were also shown to allow positronium formations on the surface. Surface positronium formation is essential for determining the lifetime changes resulting from high local electric fields.

2 Positron Theory

2.1 History

Positrons, the antiparticle to electrons, have served the scientific community in a variety of functions since discovered in 1932 by Carl Anderson [12]. Originating as the first antiparticle ever discovered, positrons transitioned from a particle principally used in high energy particle accelerator experiments, to a particle with unique properties capable of extracting a variety of material information, mainly used as an investigation tool for semiconductor research [13]. Material information is obtained by an understanding of the positron's interaction with the surrounding material at low energies and analyzing only the byproducts of positron-electron annihilation, photon emissions. More recently the positron has been used as an investigative tool of nuclear chemistry known as positronium chemistry [14].

2.2 Positron Sources

Laboratory positron sources generally create positrons through either pair production or β^+ emission [15]. One of the most commonly used positron sources is ^{22}Na, in particular for PALS measurements. ^{22}Na undergoes a β^+ decay, positron emission, to Ne^{22}. A β^+ decay is a radioactive process that converts a proton into a neutron, emitting a positron and a neutrino, as

demonstrated by Equation 1 [16]. ^{22}Na has several other decay modes with intensities demonstrated by Table I.

Table I: ^{22}Na Decay Modes

Process	Intensity (%)	End Point Energy (keV)
β^+	90.326	545.7
β^+	0.056	1820.3
Auger K	8.74	0.82
X-Ray	0.16	0.849
Gamma-Ray	99.941	1274.5

Most notably, the high intensity gamma-ray at 1274 keV, serves as the birth gamma (start time) for a vast majority of PALS measurements. For most experimentation the higher energy mode β^+ for ^{22}Na is generally ignored due to the low probability. The lower order β^+ follows the decay

$$^{22}\mathrm{Na} \rightarrow {}^{22}\mathrm{Ne} + e^+ + \nu \qquad (1)$$

in which over 0.5 Mev of binding energy is released in the form of kinetic energy split between the positron and the neutrino. The spectrum of energies and normalized probability for the energy of positron emission is demonstrated by Figure 1.

Due to the high electromagnetic cross section, at ^{22}Na β^+ kinetic energies, the positron can only penetrate solid materials on the order of 50-200 microns. This greatly influences the number of applications that positrons can be used for. In particular, positrons are generally not used for deep penetrating experiments without the use of a particle accelerator.

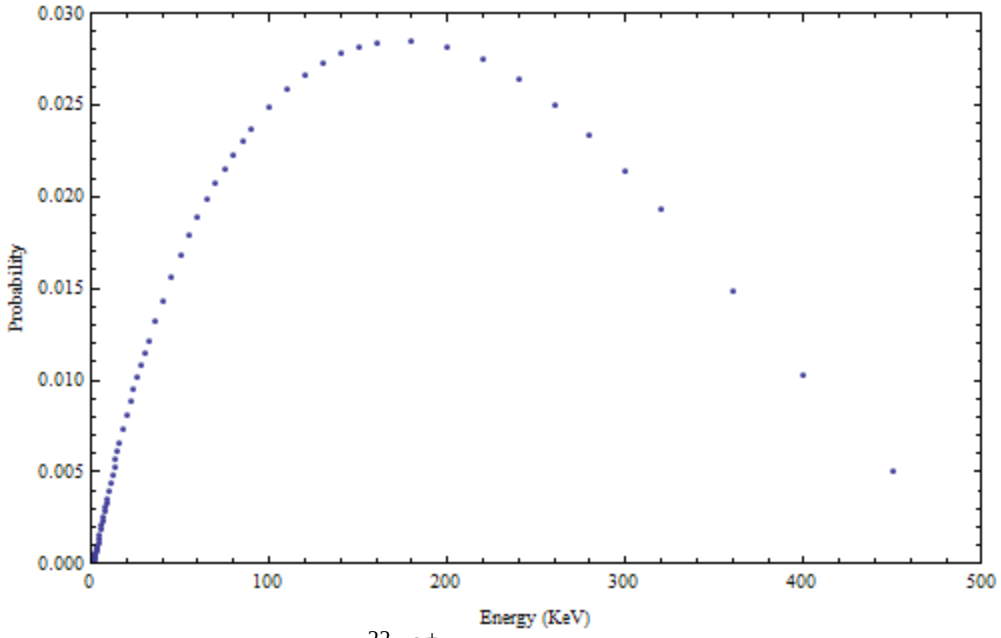

Figure 1: Na^{22} β^+ Positron Energy Spectrum

2.3 Annihilation

A positron is identical to an electron, only with polar opposite quantum numbers. In particular the fundamental distinction between a positron and electron is a difference in electrical charge and lepton number. Similar to an electron, the positron is a stable particle. However, when the wave function of a positron and an electron overlap the two particles annihilate. Due to the high density of electrons in the known universe, the lifetimes of positrons from thermalization to annihilation are on the order of hundreds of picoseconds.

Positrons can annihilate through several seemingly different mechanisms. They can undergo prompt decay with lifetimes of 2×10^{-10} s, or they can interact with surrounding electrons in a variety of ways that may result in lifetimes of up to tens of nanoseconds [17]. If an accurate wave function can be determined, the annihilation rate of these longer lived states can be calculated based upon an effective annihilation operator [14] . The annihilation rate given in bra-ket notation is [14]

$$\lambda = \langle \Psi \left\| \sum_{\mathrm{e,p}} \hat{\lambda}_{e,p} \right\| \Psi \rangle \tag{2}$$

where $\hat{\lambda}_{e,p}$ is defined as

$$\hat{\lambda}_{e,p} = 8\pi \sum_{S,M} D_s \| \sigma_{S,M} \delta^3(r_{\mathrm{ep}}) \langle \sigma_{S,M} \| \tag{3}$$

where Ψ is the wavefunction of the positron-electron pair, $\sigma_{S,M}$ is the cross section for annihilation, r_{ep} is the mean separation between the positron and electron, and D_s is a normalization constant. The most probable decay mode of which is 2 photon (2γ) annihilation [18], with a cross section given by Equation (4), originally derived by Dirac in 1930.

$$\sigma_{2\gamma} = \frac{4\pi r_o}{\gamma + 1} \left(\frac{\gamma^2 + 4\gamma + 1}{\gamma^2 - 1} \mathrm{Ln}(\gamma + \sqrt{\gamma^2 - 1}) - \frac{\gamma + 3}{\sqrt{\gamma^2 - 1}} \right) \tag{4}$$

$$r_o = \frac{q^2}{4\pi \epsilon_o m c^2} \tag{5}$$

$$\gamma = \frac{1}{\sqrt{1 - \frac{v^2}{c^2}}} \tag{6}$$

Where q, m, and v are the charge, mass and velocity of incident positron and ϵ_o is the permittivity of free space. For non-relativistic velocities this cross section reduces to [18]

$$\sigma_{2\gamma} = \frac{4\pi {r_o}^2 c}{v} \tag{7}$$

where r_o is the classical radius of an electron.

Equation (7) demonstrates the familiar relationship that at low energies the cross section for positron annihilation approaches ∞. At relativistic velocities the cross section drastically decreases, yet remains finite.

Upon annihilation the electron and positron energy is conserved by the release of gamma rays according to

$$E = \sqrt{2m_e c^2 + \mathrm{KE}_p + \mathrm{KE}_e} \tag{8}$$

where KE is the kinetic energy of the positron (p) and electron (e).

For 2γ annihilation, if the electron and positron momentum is taken to be zero, each gamma ray will be emitted with 511 keV of kinetic energy approximately 180^o apart. In addition to energy conservation, angular momentum must also be conserved according to

$$(-1)^{n_\gamma} = (-1)^{L+S} \tag{9}$$

where L and S are the total spin and orbital angular momentum quantum numbers, and n_γ is the total number of photons. The most probable events are 2γ or 3γ events. 2γ events occur for singlet states of positron-electron pairs, spins are anti-parallel (S=0). 3γ events occur for triplet states of positron-electron pairs, spins are parallel (S=1).

2.4 Positronium

Similar to the hydrogen atom at low energies a positron and electron can form a quasi-stable neutral particle known as positronium. Positronium (Ps) can form when an incident positron interacts with a target atom within an energy range higher than the ionization potential of positronium and lower than the ionization potential for the weakest bound valance electron. Due to the reduced mass of positronium, the binding energy of such a system is 6.8 eV, exactly half that of the hydrogen atom. For ground state positronium formation, incident positron energy must be within

$$E_i > E_{e^+} > 6.8\text{eV} \tag{10}$$

Positronium can exist in two states, S =0 (singlet) or S = 1 (triplet). The triplet state is referred to as ortho-positronium, while the singlet state is referred to as para-positronium. For ground state annihilation events, in accordance with Equation (9), para-positronium can only precede by emission of an even numbers of photons, while ortho-positronium states only by an odd number. Because the most probable events are either 2γ or 3γ events, the measured ratio between recorded 3γ events relative to 2γ events can provide indication to the amount of ortho-positronium formation that was present within a material.

Due to the conservation of spin and momentum, two vastly different annihilation rates occur for ortho and para-positronium.

$$\Gamma_{2\gamma}(n_{\text{ps}}{}^1S_0) = \frac{1}{2}\frac{\text{mc}^2}{\hbar}\frac{\alpha^5}{n_{\text{ps}}^3} \tag{11}$$

$$\Gamma_{3\gamma}(n_{\text{ps}}{}^3S_1) = \frac{2}{9}(\pi^2 - 9)\frac{\text{mc}^2}{\hbar}\frac{\alpha^6}{n_{\text{ps}}^3} \tag{12}$$

Where α is the fine structure constant, $\hbar$ is the reduced Planck constant, and n_{ps} is the positronium energy state. The lifetimes, the reciprocal of annihilation rate, are 140 ns for ortho-positronium and 125 ps for para-positronium. The formation ratio of ortho-positronium to para-positronium for a free electron gas is 3 to 1. However, this is only a formation ratio for an ideal free electron system, and actual physical systems can differ. Combining annihilation rates with the 3 to 1 formation ratio results in a mean lifetime of approximately 500 ps. Although not a true value of any real system, many physical systems contain system lifetimes in close proximity to this value.

2.5 Positron Interactions with Metals

Several metals have the capability of binding with positrons to form positronium compounds [19]. A positron with an initial kinetic energy propagating through a material undergoes multiple scattering events until it either exits or thermalizes within the material. At the surface, positrons can be trapped by surface potential wells and annihilate as positronium. Similar to electrons, positrons can also be emitted with a characteristic energy equal to the positron work function (ϕ_+) of the material. This is only possible for negative positron work functions, present in such materials as gold (-1.63 eV) [20].

Positrons near the surface of metals can also be emitted as positronium states. Positronium emission near the surface of metals occurs when the positronium potential is negative, as is true for most metals. The positronium potential can be calculated by [21]

$$\phi_{\mathrm{Ps}} = \phi_+ + 2\phi_- + E_g \qquad (13)$$

where ϕ_- is the electron work function for the material and E_g is the Ps^- ground state energy -6.96 eV [21]. Materials with negative positronium potentials can be used as positronium beams, emitting positronium at a precise energy. Negative positron work functions can be as positron beams, emitting positrons at a precise energy. More important to this work, materials with negative work functions can emit positrons or positronium at an energy that may be favorable for positronium formation species at surface abnormalities.

2.6 3γ/2γ Positron Annihilation Ratios

In addition to direct 2γ annihilation, direct 3γ annihilation can also occur. The cross section for 2γ annihilation was previously given by Equation (4). The cross section ratio for 3γ to 2γ annihilation events for a positron interacting with a free electron gas is directly proportional to

the ratio of ortho to para lifetimes as demonstrated by Equation (14). The factor of 3 is required because ¾ of all positron electron collisions at low energies are in triplet states.

$$\frac{\sigma_{3\gamma}}{\sigma_{2\gamma}} = 3\frac{\tau_1}{\tau_3} = \frac{1}{372} \tag{14}$$

Solids in particular single crystal metals have been used to experimentally verified this $\frac{1}{372}$ ratio. Single crystal metals are effective at reproducing this cross section ratio because the tight binding of the atoms and molecules in a lattice does not allow for the space required for positronium formation [22]. Because positronium does not form, the annihilation cross section is near identical to that for free electrons. However, for other materials, on surfaces, or in defects this ratio can be altered. For example in a solid, if a void exists room for positronium formation may be present.

Another influencing mechanism is known as "pick off" annihilation. Pick off occurs when the positron bound in a positronium system, annihilates with an adjacent electron. Other interactions of positronium with surrounding electrons may also result in conversion processes. For example O_2 is known to suppress ortho-positronium annihilations by conversion to the singlet para-positronium state [23]. The reverse conversion process, para to ortho, generally is not observed because of the vast time difference between ortho and para positronium (140 ns to 124 ps) species.

For triplet positron electron states, upon annihilation, the 3 quanta of energy must conserve energy and momentum according to

$$k_1 + k_2 + k_3 = 2m + \delta \tag{15}$$

$$\bar{k_1} + \bar{k_2} + \bar{k_3} = \bar{\delta} \tag{16}$$

where δ is a small deviation, m is the mass of the positron and $\bar{k_i}$ and k_i are the momentum and kinetic energy of each individual photon. The spectrum of energies resultant from 3 photon annihilation ,originally derived by Ore and Powel, can be determined by Equation 17 [24].

$$F(k) = 2(k\frac{(m-k)}{(2m-k)^2} - \frac{2m(m-k)^2}{(2m-k)^3}\mathrm{Ln}(\frac{m-k}{m} + \frac{2m-k}{k} + \frac{2m(m-k)}{k^2}\mathrm{Ln}(\frac{m-k}{m}))) \tag{17}$$

Figure 2 is a graphical representation of Equation 17 applied where m is represented in terms of energy (511 keV).

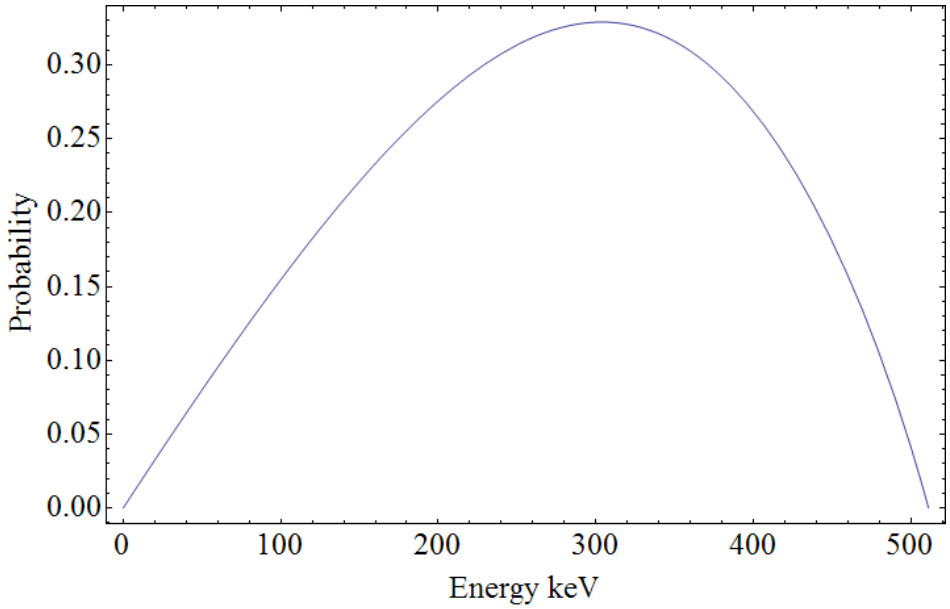

Figure 2: Normalized probability for 3 quanta emissions as a function of energy

In addition to a spectrum of energies, positron annihilation forming 3 quanta also results in photons with a variety of momentum vectors, corresponding to varying angle separations. The resulting relative number of photons per unit solid angle and unit frequency emitted by ortho-positronium are dependent upon the state of the magnetic moment, either m = ±1 or m = 0. The two formulas originally derived by Drisko are demonstrated by [25]

$$m = 0: P(\theta) = \frac{1}{2}\left(\mathrm{Sin}(\theta)^2\psi(k) + 0.5 * (3\mathrm{Cos}(\theta)^2 - 1)\phi(k)\right) \tag{18}$$

$$m = \pm 1: P(\theta) = \frac{1}{4}\left((1 + \mathrm{Cos}(\theta)^2)\psi(k) - 0.5 * (3\mathrm{Cos}(\theta)^2 - 1)\phi(k)\right) \tag{19}$$

where

$$\psi[\mathrm{k}\ \ ]:= 8\left(\frac{2-k}{k} + \frac{2(1-k)}{k^2}\mathrm{Log}[1-k] + \frac{k(1-k)}{(2-k)^2} - 2\frac{(1-k)^2}{(2-k)^3}\mathrm{Log}[1-k]\right) \tag{20}$$

$$\phi[\mathrm{k\_}]:= 8\left(\frac{k}{2(2-k)^2} - \frac{(1-k)}{(2-k)^3}\mathrm{Log}[1-k] - 4\frac{(1-k)}{k^3} - \frac{(2-k)^2}{2k^3} - 3(2-k)\frac{(1-k)}{k^4}\mathrm{Log}[1-k]\right) \tag{21}$$

are graphically represented by Figure 3.

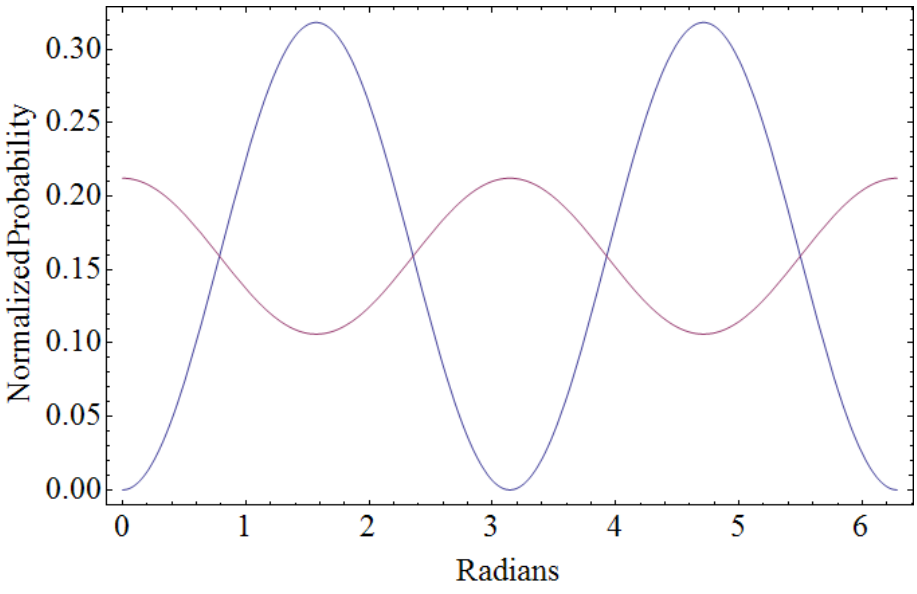

Figure 3: Normalized probability for 3 quanta emission for m=0 (blue) and m=1 (red) as a function of angle in the annihilation quanta plane

In order to determine the probability that a photon within a range of energy will be emitted following ortho-positronium annihilation, Equation (18) and (19) are integrated over the angle of interest. The normalized fraction of all threefold annihilation can be calculated by [26]

$$\frac{dP}{P} = \frac{3((1-\mathrm{Cos}(\alpha))^2 + (1-\mathrm{Cos}(\beta))^2 + (1-\mathrm{Cos}(\gamma))^2)}{2\pi(\pi^2-9)} \frac{\mathrm{Sin}(\alpha)\mathrm{Sin}(\beta)\mathrm{Sin}(\gamma)}{(\mathrm{Sin}(\alpha)+\mathrm{Sin}(\beta)+\mathrm{Sin}(\gamma))^3} d\Omega d\alpha d\beta \quad (22)$$

where $\frac{dP}{P}$ is the normalized probability that 3γ annihilation results in 1 photon between k_1 and dk_1 plus another photon between k_2 and dk_2, and α, β, and γ are the angles between k_2 and k_3, k_3 and k_1, and k_1 and k_2.

2.7 Positron Lifetimes in External Fields

The applications that utilize the unique characteristics of positrons are greatly limited due to the short lifetime of the positron. In vacuum, electromagnetic fields can be introduced to maintain velocities that decrease the cross section for positron annihilation. Devices have been assembled that use these electromagnetic fields to store positrons for weeks [27] [28]. These storage techniques can provide the extended lifetimes necessary to increase the distribution and number of positron applications. However, due to the columbic repulsion the density of positrons has a theoretical maximum limit of 5 x 10^{12} cm^{-3} for a 1 tesla magnet [29]. It has been theoretically demonstrated that for a neutral positron system such as positronium, external electromagnetic fields can produce an environment in which positron lifetimes can far exceed the lifetime of positronium in a vacuum [10]. Although other complications arise, these neutral long lives states would not suffer the same theoretical limitations due to columbic repulsion [10]. In order to

enhance positron lifetime and storage densities a better understanding of neutral positronic species interactions with external fields is necessary.

The annihilation lifetime of positronium is largely dependent upon the separation distance between the positron and electron. When an external electric field is applied, these two oppositely charged particles should polarize, increasing separation and thus increasing positron lifetimes. However, previous research has demonstrated that positron lifetime experiments conducted in the presence of external electric fields do not show any increase in lifetimes. In fact, experiments have demonstrated that there is a decrease in the formation of positronium for non-polar samples, decreasing ortho-positronium and therefore decreasing the average lifetime [30]. These studies have also concluded that positronium formation does not appear to be altered for polar samples [31]. These experiments were conducted using mainly polymers, which generally contain voids. These voids allow for positronium formations. Once formed, within a finite sized void, polarization effects will only be so effective. The polarization effects will alter the lifetime of some positronium states, broadening the lifetime distribution. However, the mean lifetime will remain nearly unchanged.

However, for isolated systems positronium separation can be maximized, and polarizing effects due to external fields should increase positronium lifetimes. Theoretical calculations have shown for crossed electric and magnetic fields large mean separation distances for positronium atoms can occur resulting in extended annihilation lifetimes [32]. For positronium the pseudo-momentum can be calculated by

$$K = m_e \dot{r}_{e^+} + m_p \dot{r}_{p^-} - \frac{q}{c} B \times (r_{e^+} - r_{e^-}) \tag{23}$$

where B is the magnetic field, $r_{e^+} - r_{e^-}$ is the separation distance between the positron and electron, and $\dot{r}_i$ is the positron or electron velocity, given by

$$\dot{r}_i = \frac{i}{h}[H, r_i] \tag{24}$$

where H is the total Hamiltonian operator defined as

$$H = \frac{p^2}{2} + \frac{1}{4}(K + B \times (r_{e^+} - r_{e^-})^2) - \frac{1}{\|r_{e^+} - r_{e^-}\|} + E \cdot (r_{e^+} - r_{e^-}) \tag{25}$$

where p is the positron momentum and E is the external electric field. Theoretical analysis of positronium systems conclude that for [10]

$$K > \sqrt[3]{\frac{27B}{2}} \tag{26}$$

there exists the formation of outer wells, stable energy states that have a large separation distance from bound electron. This is demonstrated by Figure 4. Pseudomomentum and magnetic field values of 0.4 au and 10^{-5} au result in theoretical lifetimes several orders of magnitude longer than the longest lifetimes of positronium in a vacuum, 140ns.

Figure 4 demonstrates how the introduction of a crossed magnetic and electric field can create magnetically distorted quantum wells. These fields create ground state energies that allow for large separations between positron and electrons, reducing annihilation rates, and also increasing binding energies, allowing the system to be more stable against external energy events.

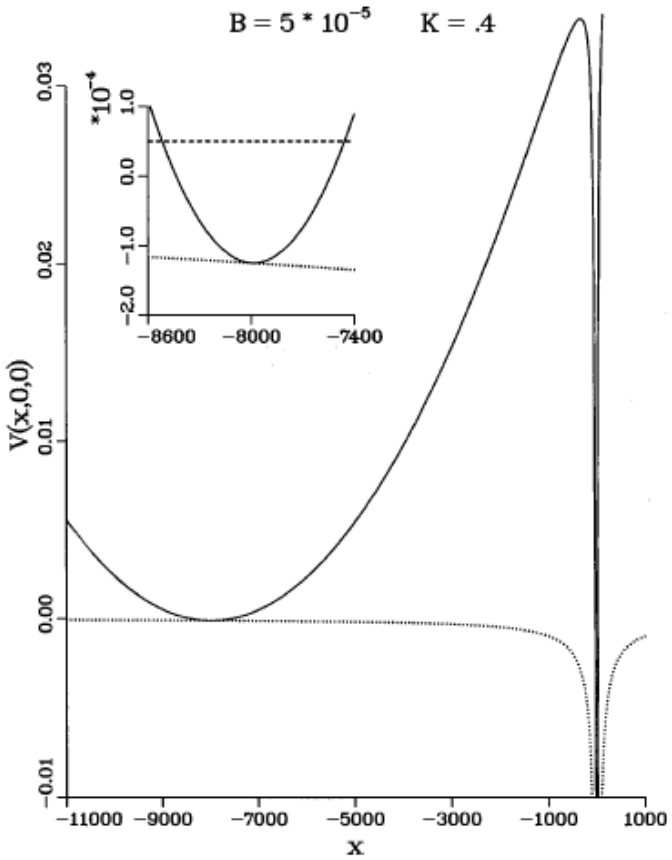

Figure 4: Graphical representation of quantum energy states for large values of crossed electromagnetic fields (B = $5x10^{-4}$ a.u. and K=0.4 a.u.). Of particular interest is the large separation distance between ground state and saddle point [10].

Additional theoretical research has shown that by applying only an external electric field, positronium systems can be polarized to the extent that a change in lifetime can be observed. This exponential increase in lifetime is demonstrated by Figure 5.

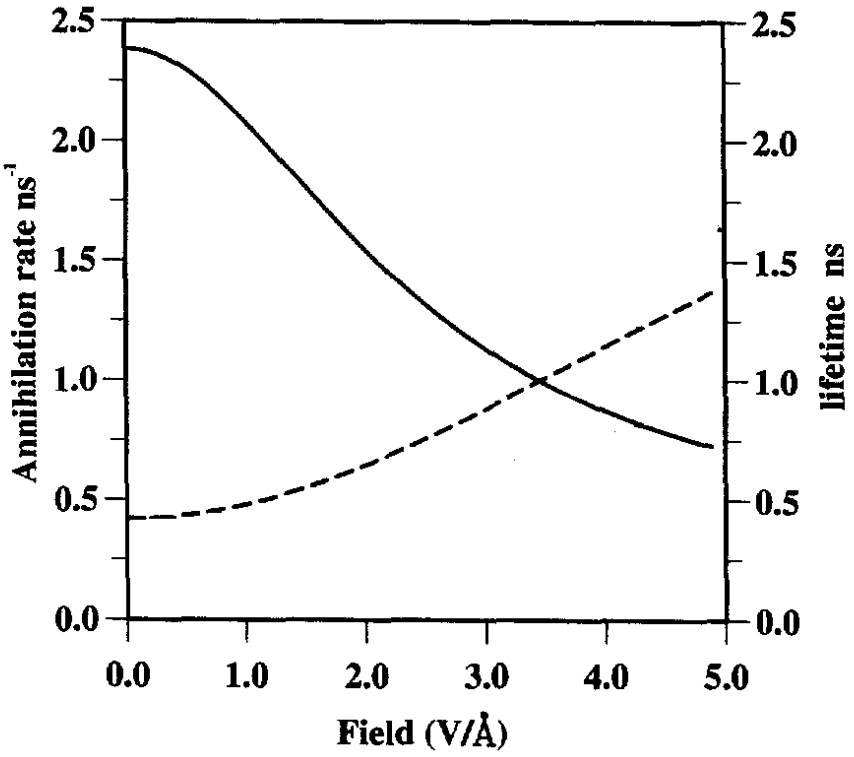

Figure 5: Graphical representation of the increase in positron lifetime (dotted line) and decrease in annihilation rate (solid line) for a PsH [11]

As Figure 5 illustrates for high local electric fields on the order of a few volts per angstrom, an increase in the lifetime of a PsH molecule should be observed. The binding energy of the positron in a PsH system is approximately 1 eV [11]. For molecules with lower binding energies the positron should have a higher polarizability in the presence of external fields, therefore lifetime effects may be encountered at lower voltage ranges.

3 Design and Implementation of a PsARS Detector

3.1 3γ/2γ Positron Annihilation Ratios

3.1.1 3γ/2γ Positron Annihilation Experiment Overview

A PsARS detector was constructed using a cylindrical NaI ring scintillation cylinder. NaI was chosen as a suitable scintillating material because it has high-quality photon capture efficiency with acceptable energy resolution of approximately 10% for 662 keV photons [33]. The NaI ring detector used for experimentation is 18 cm long, has a 20 cm diameter, and is 3 ½ cm thick as depicted by Figure 6. The large size and geometry of this NaI ring detector was ideal for radically symmetric experiments as well as detector efficiency.

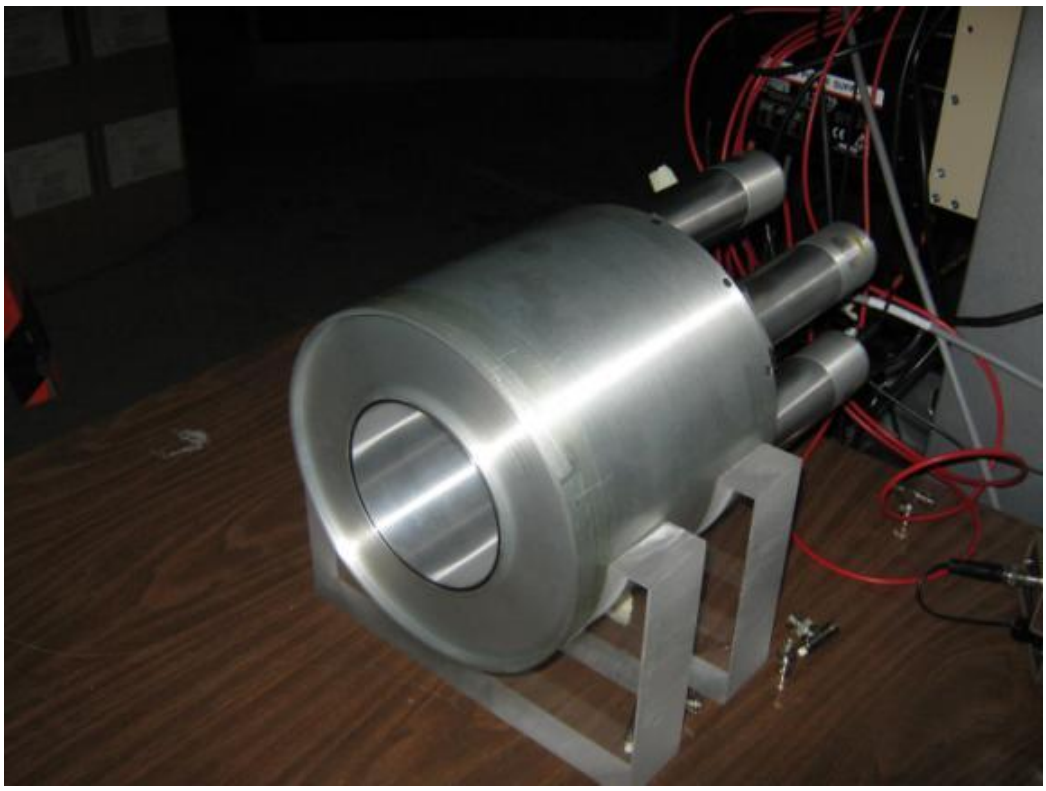

Figure 6: Picture of NaI ring detector used for 3γ/2γ experimentation.

The signal from each of the six PMTs were sent to six ORTEC (Model 113) pre-amplifiers and then connected to separate digital channels. Measurements were taken using a XIA DGF-4C digital system. A digital system was preferred due to the expected dependence of results on post process analysis. The use of a digital signal allows the user to take one measurement and analyze

the triggered data points through different filtration methods. Two XIA cards were connected in series with 6 channels corresponding to the 6 PMTs attached to the NaI ring. The XIA cards are operated through a CAMAC controller connected to a PC which processes data analysis through an Igor Pro GUI. Figure 5 demonstrates the depicted configuration.

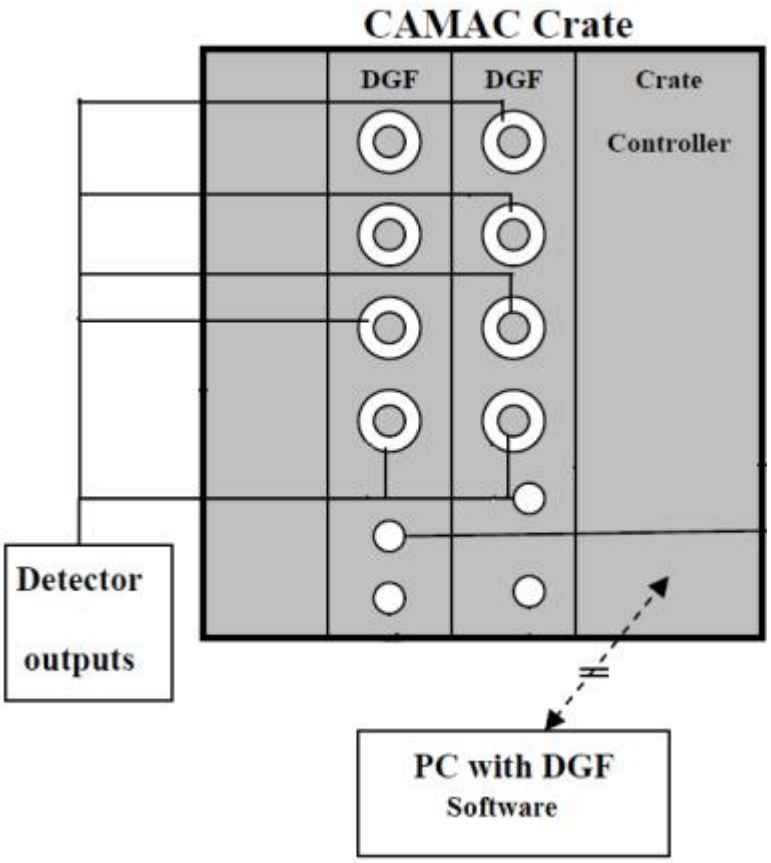

Figure 7: Simplified diagram of experimental setup connecting the NaI Ring Detector PMTs to the XIA system

The XIA cards were set with jumper configurations denoted in Table II.

Table II: DGF-4C hardware jumper configuration

	Module 1 - 1240	Module 1 - 1244
Jumper 1	Installed	Removed
Jumper 2	Installed	Removed
Jumper 3	Removed	Installed
Jumper 4	Removed	Installed
Jumper 5	Board Clock	External

The data collection spectrum was set to record time and energy digital units, with digital filters conducted through the Igor Pro GUI. Every coincident event trigger recorded on any of the PMTs within a module, triggered all other PMTs in that module. Figure 8 shows the experimental setup.

The 3γ/2γ annihilation ratio can be determined by recording 3 quanta and 2 quanta events within the detector and applying both experimentally and theoretically determined correction factors. The 3γ/2γ annihilation ratio with applied correction factors can be determined by

$$\frac{\sigma_{3k}}{\sigma_{2k}} = \frac{N\,(3\gamma)}{N\,(2\gamma)} \frac{\epsilon_{2\gamma1}\epsilon_{2\gamma2}}{\epsilon_{3\gamma1}\epsilon_{3\gamma2}\epsilon_{3\gamma3}} \frac{\mathrm{P}}{\mathrm{dP}} \tag{27}$$

Where N is the number of coincident counts of either 3γ or 2γ radiation and ϵ_1, ϵ_2, and ϵ_3 corresponds to the relative absolute efficiency of each triggered detector relative for 3γ radiation (energy) or 2γ radiation (energy) , and $\frac{\mathrm{dP}}{p}$ is the normalized fraction of threefold annihilation.

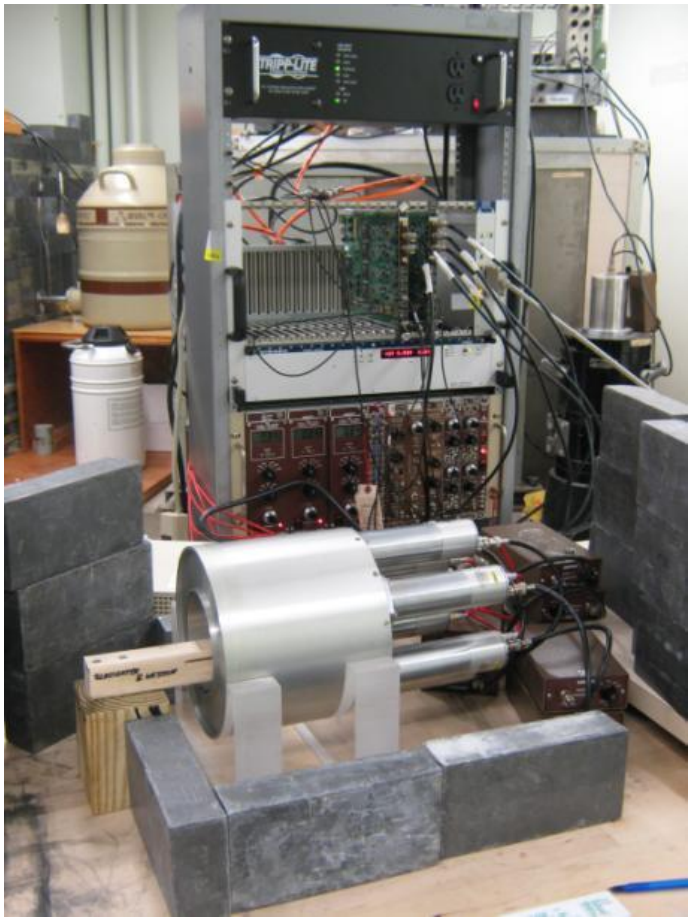

Figure 8: 3γ/2γ Experimental setup

A coordinate system is chosen to reside within the plane of all quanta, requiring that

$$\alpha + \beta + \gamma = 2\pi. \tag{28}$$

All quanta of radiation are referenced in a coordinate system in which each quanta subtends to the same plane. In practice the true 3γ/2γ annihilation ratio can be determined by applying several weighting values to Equation (27) to account for a multitude of detector correction terms.

3.1.2 PsARS Detector Calibration, Efficiency, and Resolution

The initial step taken to develop the PsARS detector, was to determine the optimum bias necessary to maximize count rate. An analog system consisting of an ORTEC model 142 preamplifier, ORTEC model 556 high voltage (HV) power supply, ORTEC model 671 linear amplifier, a ORTEC model 551 single-channel analyzer (SCA), and an ORTEC model 996 counter were connected to each PMT. Figure 9 illustrates the experimental setup.

A ^{22}Na source was used to generate the desired positrons and ultimately the 511 keV photons. A Tektronix DP07104 Oscilloscope was connected to each PMT in order to determine the cutoff voltage to set on the SCA to signal a 511 keV photon. The ORTEC counter was adjusted to count for a total of 60 s. At the conclusion of each 60 s the HV power supply bias was adjusted accordingly. The results of experimentation are detailed by Table IX located in the Appendix A. Because the ORTEC HV power supplies each have two HV connections in the back, PMTs that had similar responses were paired. The HV power supplies were all set to 0.844 kV for PMT numbers 1 and 4, 0.840 kV for 3 and 6, and 0.837 kV for 2 and 5.

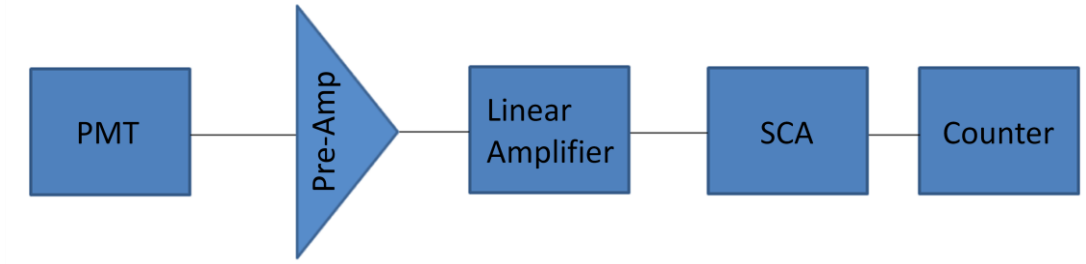

Figure 9: Diagram of analog setup used to optimize detector bias

Following detector bias optimization the NaI detector PMTs were connected using RG62A/U connectors to six identical Ortec preamplifiers, and connected directly to the DGF-4C channels. An Ortec 672 Spectroscopy Amplifier and two Ortec 655 Dual Spectroscopy Amplifiers were used to power the preamplifiers. Several digitally controlled detector trigger and

filtering responses were determined through recommendations made throughout the DGF-4C manual [34] as well as experimentally determined by minimizing the full-width at half-maxim (FWHM) of all peaks. Adjusting trigger parameters to minimize FWHM will in turn minimize detector resolution. All determined values were then verified with previous researchers DGF-4C settings using a similar experimental setup [35] [36]. Table X, Appendix B, outlines the pulse shape discrimination attributes applied for all experimentation with DGF-4C modules. Gain values on the DGF-4C were chosen and decay lengths determined by the auto fit routine.

A total of two DGF-4C modules were connected to a CAMAC crate using an auxiliary 16 pin header on the backside of each module. For energy and time data acquasitions involving two or more modules, unidentified noise or interference peaks were present in the spectrum. Figure 10 illustrates the presence and characteristics of these noise peaks.

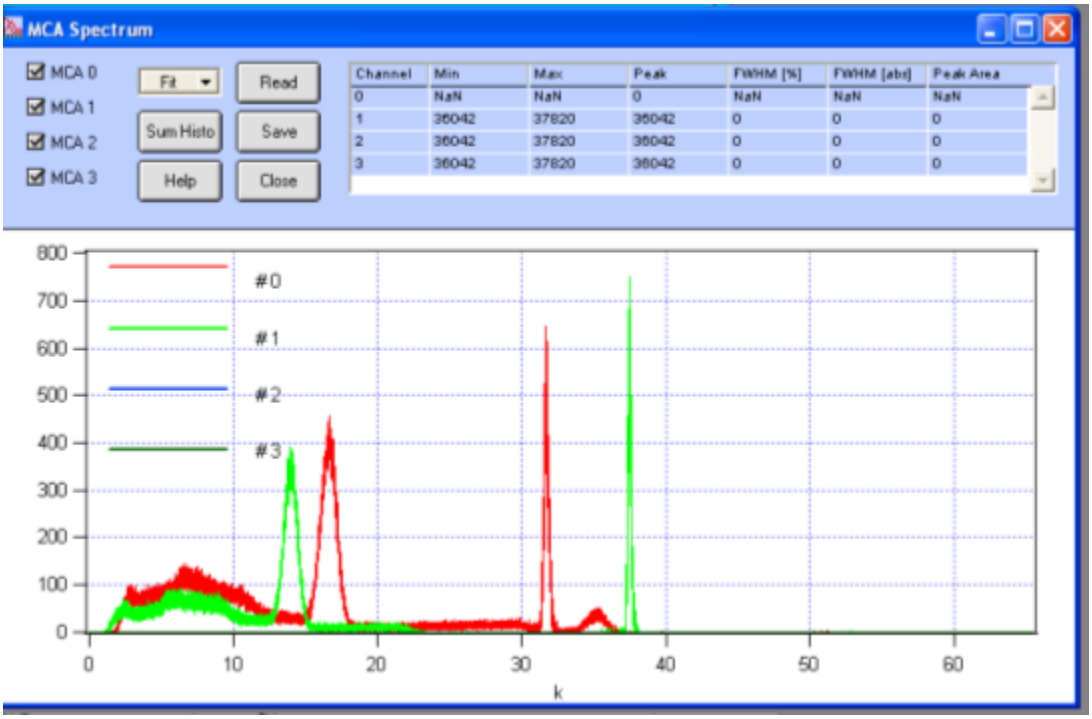

Figure 10: Interference peak found on DGF-4C during most spectrum data runs. This peak was eliminated by using a Ortec logic unit in all experimentation.

These peaks were eliminated by further synchronizing the DGF-4C modules through use of a logic unit. The Busy Out of both DGF-4C cards were connected to an ORTEC CO4020 Quad 4-input logic unit. One of the logic unit's AND logic pulses was then split and connected to both DGF-4C module's $Sync_{in}$. In instances when both DGF-4C modules recorded a pulse, the Busy Out would send a pulse to the Ortec logic unit, which would then send a logic pulse to the $Sync_{in}$. The use of the logic unit in this manner eliminated the large interference peaks.

The 3γ and 2γ annihilation rates were determined by using the intrinsic coincidence capability of the DGF-4C software program. Within the Coin. Pattern OX in the DGF-4C software, only coincident events within a single module were designated to trigger on events. The definition of coincidence within the software was set to 25.6 μs, but later adjusted to 50 ns in post process analysis. Two opposing PMTs were selected to record double coincidence events on a single module, used to determine the 2γ count. The additional four PMTs were selected to only record triple coincidence between any three of the four channels, used to determine the 3γ count. This separation is graphically represented by Figure 11.

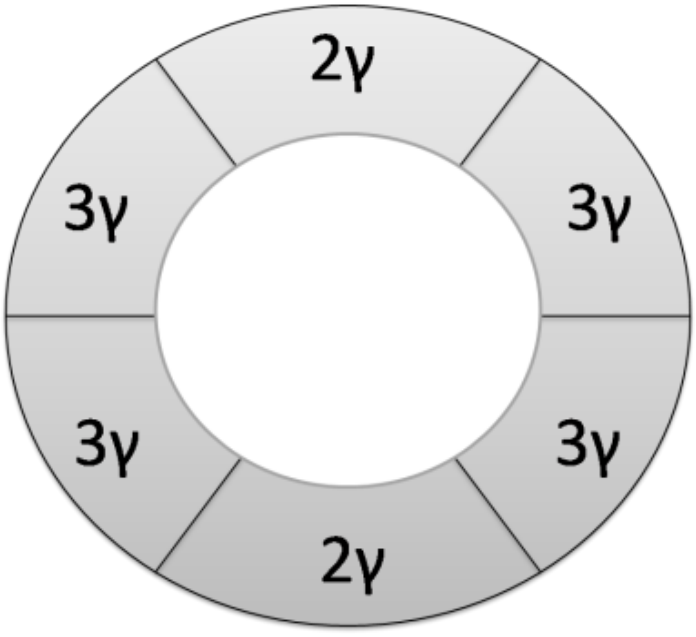

Figure 11: Graphical representation of 3γ/2γ segmented coincidence pattern.

A full spectrum of events was recorded for multiple isotopes in order to develop an energy calibration to convert the XIA software given bin channel number into a proper energy value. Radioisotopes of ^{22}Na, ^{137}Cs, and ^{57}Co were used for this energy calibration. Each source was placed onto the 3γ / 2γ holder, shown in Figure 12. This holder was designed to place the source at a near exact center for NaI ring detector experimentation. This same holder will be used for PsARS experimentation.

Of particular interest are the 511 keV photons from ^{22}Na, the 612 keV photons from ^{137}Cs, and the 122 keV photons released from ^{57}Co. Each run lasted an hour and a half, recording over 1 million counts each. Figure 13 is the spectrum recorded through an hour and a half ^{137}Cs measurement.

Figure 12: PsArs holder used to center positron source in 3γ/2γ, calibration, and efficiency experiments**.**

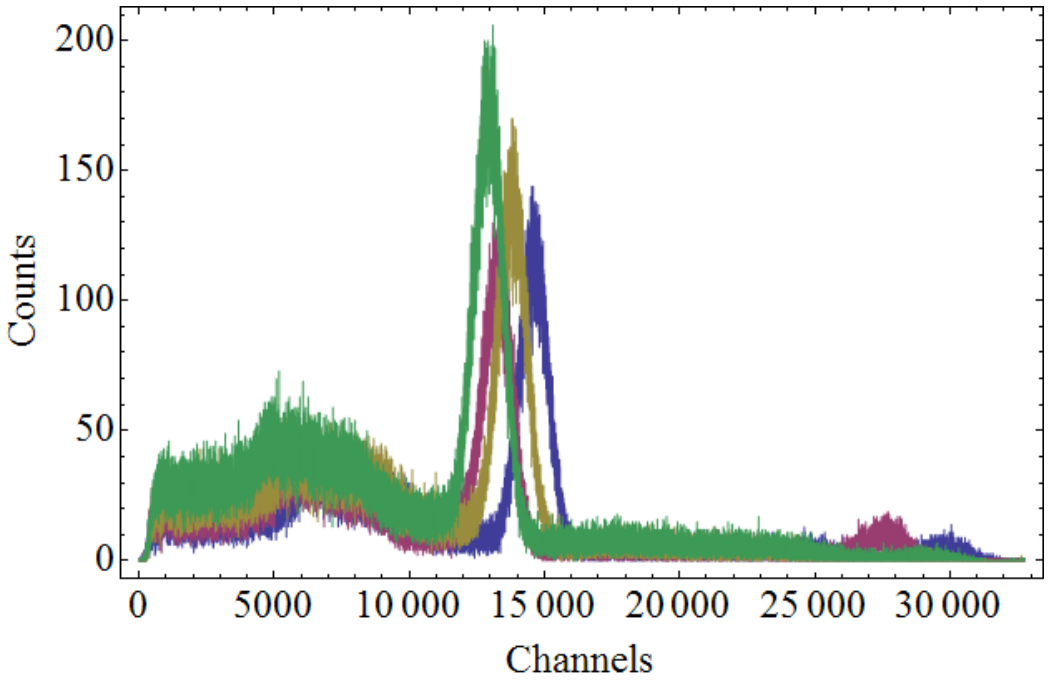

Figure 13: Energy spectrum of 662 keV photons from ^{137}Cs for Module 1 channels 1-4

For each radioisotope peak, the channel location was determined. A best fit routine was then used to determine the correlation between channel number and energy. The results of the fit and data points from the radioisotopes used are provided by Figure 14. These data points were then fit to a 2nd order model, Equation (29), in order to correlate the digital output channel number into a more familiar energy value. Table XI, located in the Appendix C, demonstrates the results for all channels. Figure 14 is the graphical representation of all six channels and their energy calibration curve along with the data points used to determine these best fit lines.

$$A + Bx + Cx^2 \tag{29}$$

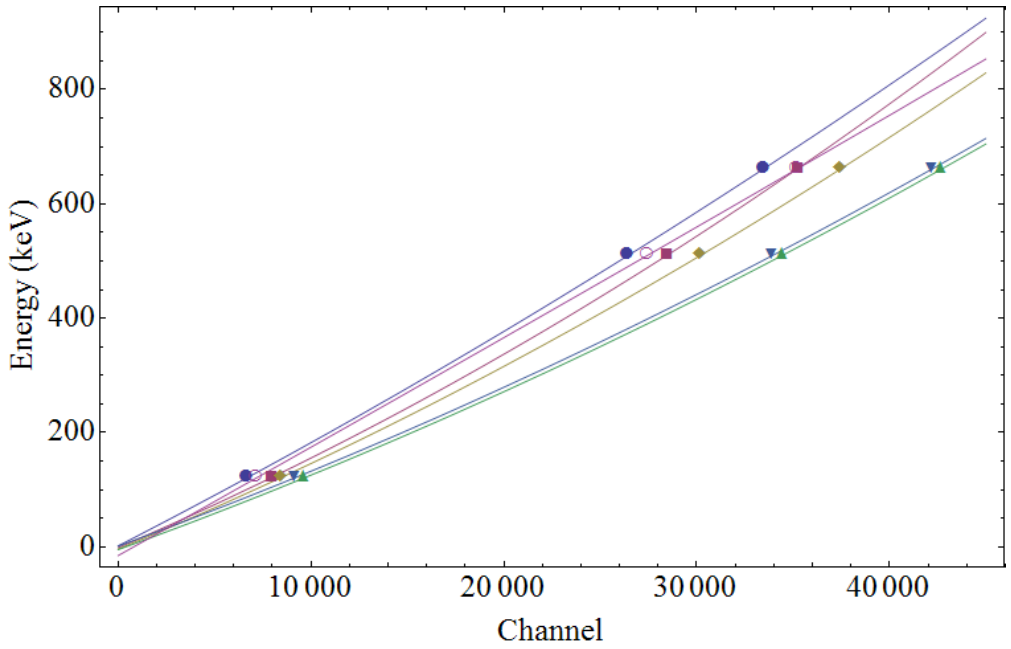

Figure 14: NaI ring detector calibration fit curves and data points

In order to determine the proper 3γ / 2γ ratio the intrinsic efficiency calibration was determined for each PMT. The decay time of most recorded pulses was on the order of 25 μs. If during that 25 μs window an additional pulse triggers within the same channel neither pulse is recorded, pulse pileup. Not recording pulse pileup data avoids spectral effects by making the detector a paralyzable detector. In order to limit pulse pileup, only low activity (10^{-2} uCi) sources were used for the efficiency calibration. In particular local ID number 00212 ^{22}Na with activity of 0.00728 uCi (1 Dec 2009) and local ID number T-085 ^{57}Co with activity of 0.02266 uCi (1 Dec 2009) were used for intrinsic efficiency data points. Each source was placed within the NaI detector using the 3γ / 2γ holder. The results of the calibration determined by ^{22}Na and ^{57}Co are depicted by Figure 15. These data points represent the intrinsic efficiency per channel.

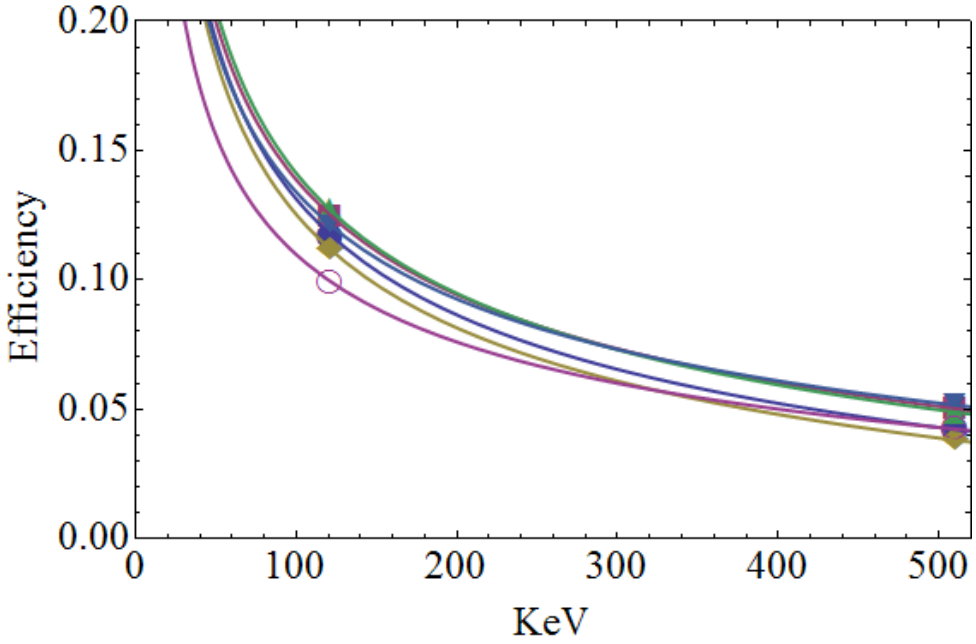

Figure 15: Intrinsic efficiency of the NaI detector

The calibration data points were then fit to an inverse natural log function, characteristic of NaI within the energy range of interest [33]. Table XII, located in the Appendix D, shows the results of the best fit to

$$\text{Eff[x]}:= \frac{m}{\text{Log}[xb]} + c \tag{30}$$

Due to the lack of eligible sources, low radioactivity, only two data points were used in the intrinsic efficiency best fit lines. However, the experimental fit appears similar to other NaI detectors of similar design [33]. All PMTs also appear to have comparable intrinsic efficiencies as expected.

The resolution of the NaI ring detector was also characterized by applying Equation (31) to a ^{85}Sr source, where H_o is the peak energy value (514 keV).

$$\text{Res} = \frac{\text{FWHM}}{H_o} \tag{31}$$

^{85}Sr undergoes an electron capture 96 percent of the time resulting in a 514 keV gamma ray emission. This 514 keV photon was chosen because it nearly mimics that of the 511 keV photon emitted from 2γ positron annihilation. The 514 keV photon also does not undergo any of the Doppler broadening shifts characteristic of positron annihilation, and is therefore more appropriate than the 511 keV photon residual from positron annihilation. The Doppler broadening shift is due to the nonzero momentum value of the positron and electron just prior to annihilation. The resolution of the each PMT was assumed to be near identical, and was determined by summing the values of all channels over a 30 minute runtime. Figure 16 is a graphical representation of the combined ^{85}Sr spectrum. The results indicated that the energy resolution at 514 keV is 10.3 percent. This resolution value will be used throughout PsARS analysis in order to determine what energy values are appropriate to discriminate 3γ and 2γ counts.

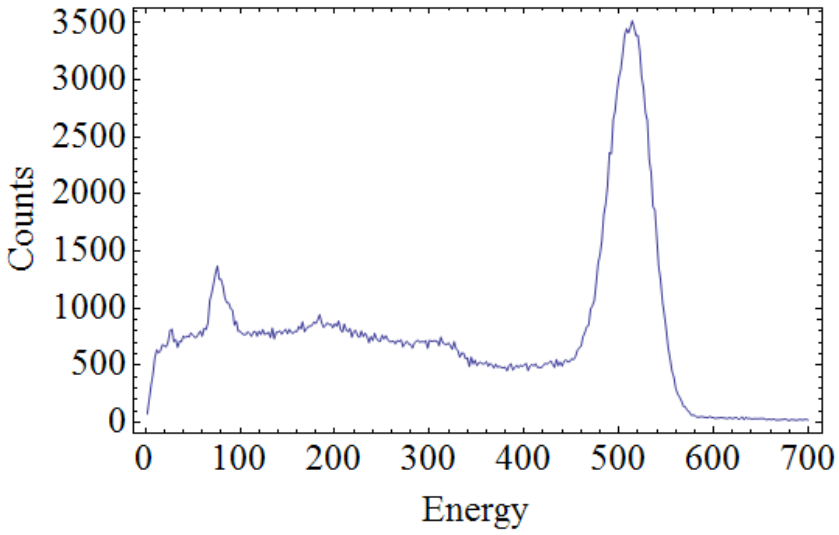

Figure 16: Graphical representation of a ^{85}Sr spectrum used to determine energy resolution

3.1.3 3γ/2γ Positron Annihilation Chance Coincidence Correction Factors

For PsARS experimentation, several correction factors were determined in order to calculate an absolute 3γ / 2γ value. For coincidence measurements, the first term to consider is the number of registered double and triple coincidence counts that are not true 2γ or 3γ annihilation of radiation events, herein referred to as chance coincidence events. The triple chance coincidence events can be broken down into three separate terms: Coincidence due to triple background counts, a Compton scattering event with the capture of the photon and resultant electron plus a simultaneous background count, or two or more simultaneous Compton scattering events. More formally the 3γ corrections due to chance coincidences can be determined from

$$3\gamma = (\sum 1\gamma_{\text{Compton+BG}}\dot{C})(\sum 2\gamma_{\text{Compton+BG}}\dot{C})\tau + (\sum 3\gamma_{\text{BG}}\dot{C}) \quad (32)$$

where $\sum 1\gamma_{\text{Compton+BG}}$ is the count rate of spectrum within 130 – 380 keV range, $\dot{C}$ is the total detector count rate, $\sum 2\gamma_{\text{Compton+BG}}$ is the 2γ coincidence count rate, $\sum 3\gamma_{\text{BG}}$ is the 3γ coincidence count rate due to background, and τ is the coincidence time. All count rates are defined as the number of counts of interest per recorded detector counts. This pseudo-count rate enables the 3γ correction factors to be independent of activity. Not basing the 3γ correction factors on activity is important for two reasons. The first is that the count rate dependence enables the 3γ / 2γ factor to be determined without an additional pulse pileup correction factor. Due to the large volume of scintillating crystal, even low radioactive sources (~.3 μCi) can produce pulse pileup. The second reason is that the activity of several of the materials to be measured are only known within a potentially influential uncertainty, roughly five percent. This uncertainty in activity could reduce the precision of the measurement. However, basing the

correction factors on count rate makes the assumption that energy distributions are similar. This is a good approximation for all sources in which ^{22}Na is used.

The accidental 2γ coincidence count rate can be determined by using a ^{85}Sr radioactive source. The 514 keV photon from ^{85}Sr decay should respond near identically to the 511 keV photon released from position annihilation. With the main exception that simultaneous emission does not occur. An hour and a half ^{85}Sr coincidence experiment utilizing the identical XIA settings as the calibration data was performed in which all PMTs were designated to record only counts for double coincidence. The result is shown by Figure 17.

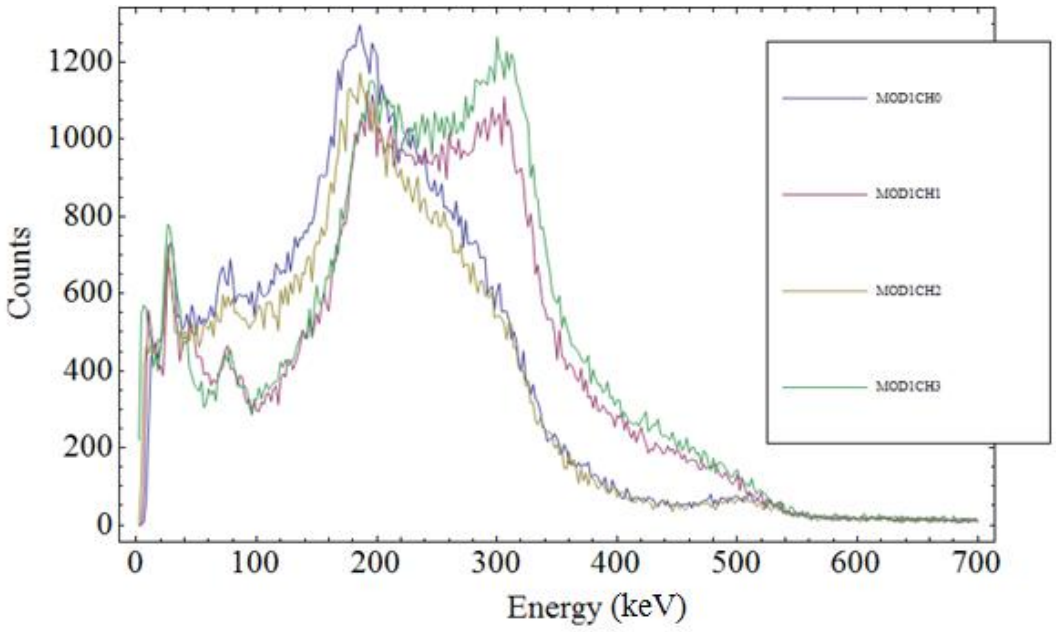

Figure 17: 2γ coincidence spectrum from ^{85}Sr source with energy in keV. With a difference in spectrum due to closer source position to CH0 and CH2

Figure 17 demonstrates several expected responses. The plot shows that many of the double coincidence data corresponds to Compton events with the resulting electron and photon both being absorbed by two separate scintillating areas and resulting into two PMTs recording a double coincident pulse. The two separate event peaks located at approximately 300 keV and 200 keV total to the expected 500 keV energy range, within the scintillating material resolution

for 511 keV annihilation photons. The response between the detectors appears biased towards CH 0 and CH 2 of Module 1, which did not record as many coincident events near 300 keV. This bias is associated with the unique geometry used for this measurement. Due to the higher activity of the ^{85}Sr source a cylindrical metal shielding container was placed surrounding the radioactive planchette. The metal container was then placed at the bottom of the NaI ring detector. This position places the source closer to the lower channels (CH0 and CH2). The cross section for scattering angle for Compton events is demonstrated by Figure 18.

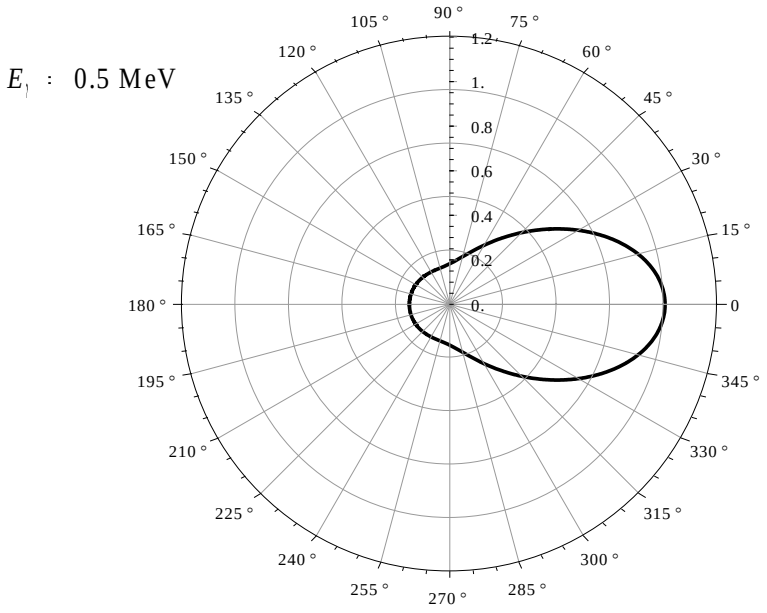

Figure 18: Klein-Nishina polar plot for the probability of resultant photon propagation.

As demonstrated in Figure 18 the most probable direction a resultant photon following a Compton event would propagate is 30^{o}. The scattered photon propagation direction is entirely dominated by small angles. For CH0 and CH2, due to proximity to the source, the most likely interactions are to occur far removed from additional channels. The combination of this

separation distance as well as propagation direction indicates that for these channels few double Compton interactions will trigger coincident events. For CH1 and CH3 Compton events are most likely to occur near a channel intersection, many times resulting in the escape of the residual photon and capture in an alternative channel.

The 2γ coincidence count rate was determined by summing the coincidence curves between 130 keV and 380 keV of CH1 and CH3 data, which correspond to most accurately resembling the configuration of PsARS experimentation. This sum was multiplied by a factor of 2 to account for the other channels. This new sum was then divided by the total count time and multiplied by the total counts per second recorded by the detector. The 2γ coincident Compton rate, defined as coincident counts per recorded decay, is

$$\sum 2\gamma_{\text{Compton+BG}} = \frac{2\sum 2\gamma_{\text{Compton+BG}}(^{85}\text{Sr})}{t\dot{C}} \tag{33}$$

where the timing window for coincidence was determined to be 50 ns, based upon detector timing resolution of coincidence events [34].

An additional hour and a half runtime ^{85}Sr spectrum was taken to record the rate of non-coincident Compton events in the 130 keV to 380 keV region of interest. Figure 19 details the results of this experimental run. Once again the ^{85}Sr source was placed in a cylindrical metal shielding container horizontally, but not vertically centered. This results in the distinct count rate difference between detectors.

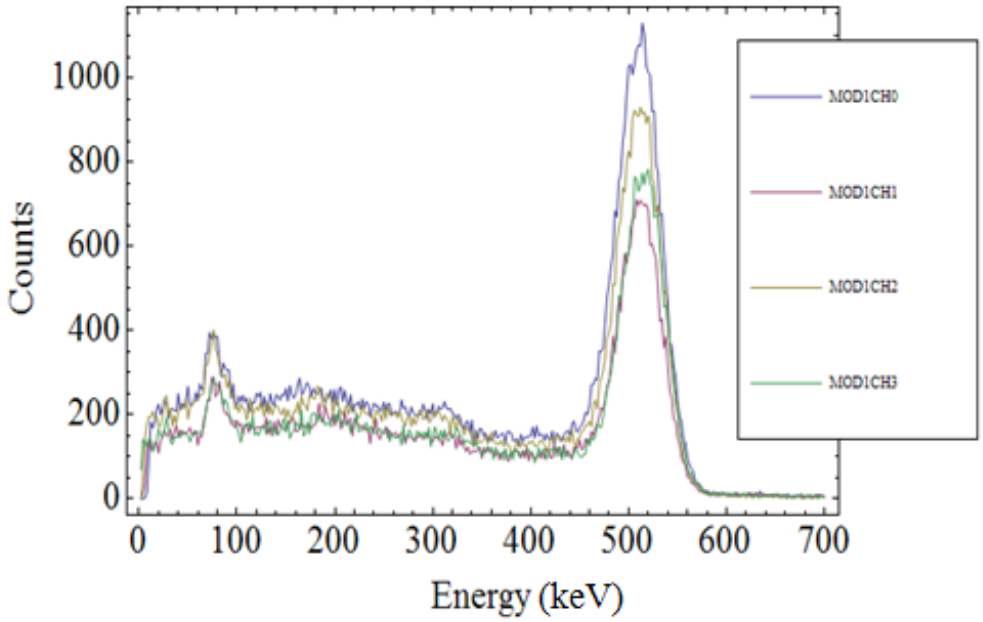

Figure 19: ^{85}Sr non-coincident spectrum

The non coincident Compton and background rate in the region of interest (130 – 380 keV) was determined by

$$\sum 1\gamma_{\text{Compton+BG}} = \frac{\sum 1\gamma_{\text{Compton+BG}}(^{85}\text{Sr})}{t\dot{C}} \tag{34}$$

This equation in combination with Equation (33) can be applied to determine an approximation to the chance coincident 3γ counts due to Compton events from simultaneous 511 keV emission. For coincident PsARS there will be approximately $4.0410^{-10}\dot{C}^2t$ chance coincident events recorded by the detector that accede from post process analysis.

Additional chance coincidence terms include 3γ counts due to a single Compton 511 keV photon emission in combination with background counts. Figure 20 shows the results of an additional hour and a half runtime of ^{85}Sr in which only triple coincident counts were recorded.

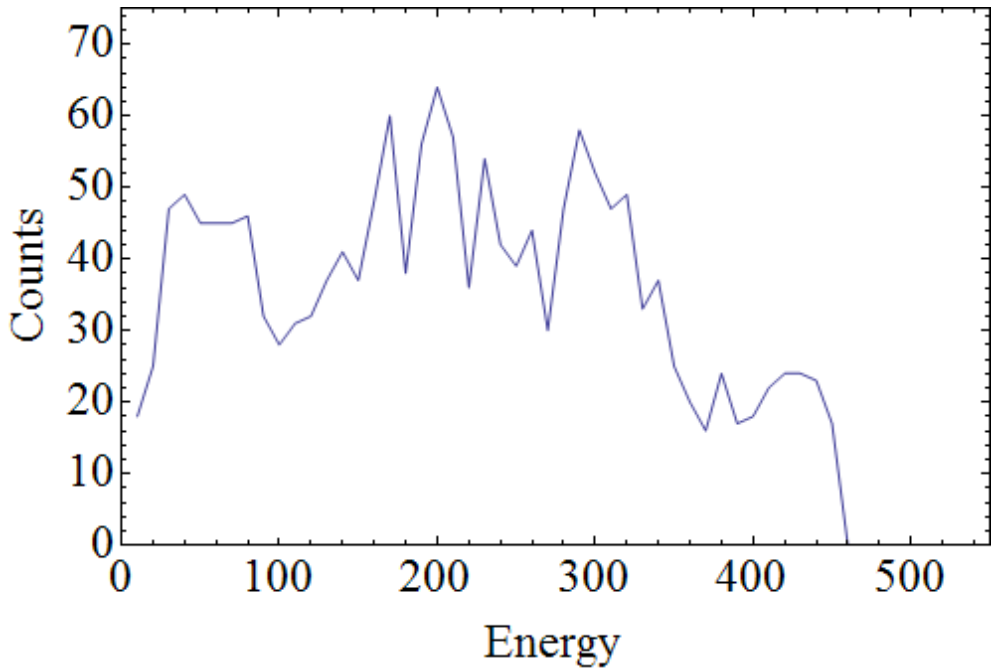

Figure 20: Coincident 3γ spectrum due to ^{85}Sr

The sum of accident background 3γ events was determined compiling and executing the algorithm located in Appendix E in Igor Pro. The algorithm is used for 3γ analysis and discriminates events based upon both coincident timing (50 ns) and energy (130 keV to 380 keV). Equation (35) is added with the combination of Equation (33) and (34) to determine the coincident 3γ counts due to Compton events from simultaneous 511 keV photon emission to include coincident triple Compton events, and double Compton events plus background.

$$\sum 3\gamma_{\mathrm{BG}} = \frac{\sum 3\gamma_{\mathrm{BG}}(^{85}\mathrm{Sr})}{t\dot{C}} \tag{35}$$

Therefore the approximation to the chance coincident rate due specifically to single 514 keV emission plus background is $5.29x10^{-8}\dot{C}t$. For count rates, $\dot{C}$, of 1000 $\frac{\text{counts}}{\text{second}}$ or greater, the total number of chance coincidence in a given experiment reduces to

$$3\gamma_{\mathrm{Chance}} \approx 4.0410^{-10}\dot{C}^2 t$$

^{85}Sr experiments were conducted in order to determine the accidental 2γ count rate. Figure 21 graphically demonstrates the summed spectrum from both channels following an hour and a half runtime, recording coincident 2γ events.

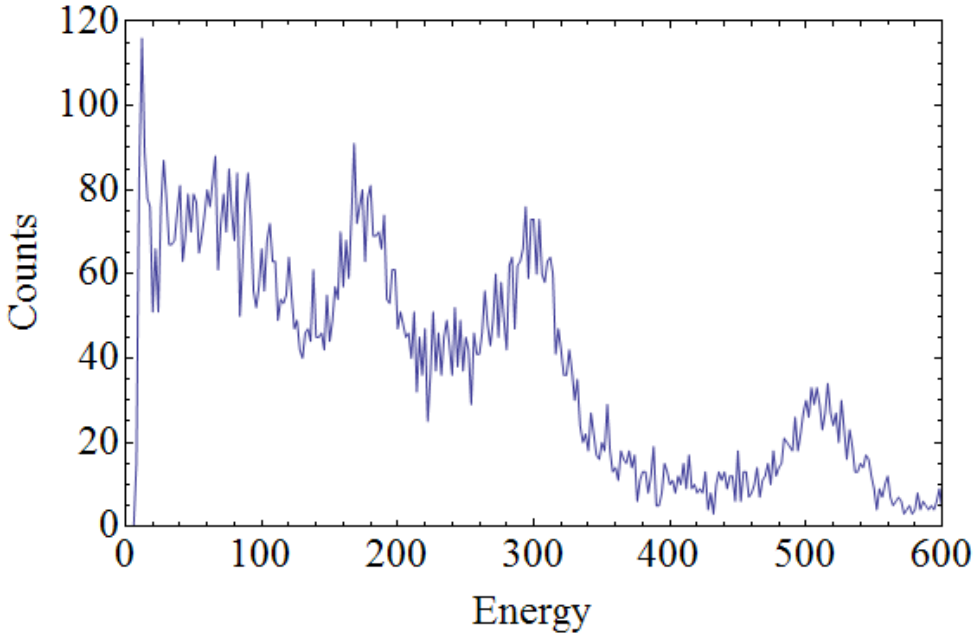

Figure 21: 2γ Coincident Spectrum from ^{85}Sr source

Similar to previous results, local peaks appear near 300 keV and 200 keV energies. A key difference between Figure 21 and Figure 17 is the local energy peak near 511 keV. Because neither of these two channels were geometrical located next to each other on the NaI crystal, only Compton events scattering at 180^{o} could record coincident events. The Klein Klein-Nishina cross section demonstrates the decrease in probability for these events. Therefore, the likelihood of a coincident event at the 200 keV and 300keV energies is lower. Consequently, the chance coincident events in the 511 keV energy range appear relatively higher.

The chance coincident 2γ events was determined by

$$2\gamma_{\text{Chance}} = \frac{\sum 2\gamma_{\text{Compton+BG}}(^{85}\text{Sr})}{t\dot{C}} \tag{36}$$

where

$$\sum 2\gamma_{\text{Compton+BG}} = \frac{2\sum 2\gamma_{\text{Compton+BG}}(^{85}\text{Sr})}{t\dot{C}} \tag{37}$$

and $\sum 2\gamma_{\text{Compton+BG}}(^{85}\text{Sr})$ was the sum of coincident spectrum from 460 to 560 keV. The factor of two is present because for positron annihilation two 511 keV photons are emitted. Based upon experimental measurements, the accidental coincident 2γ events was determined to be

$$2\gamma_{\text{Chance}} = 6.39\text{x}10^{-4}t\dot{C}$$

As an example, for a PsARS experiment with a count rate of 1000 cps for a two hour detector live time, the accidental coincident 2γ events would be approximated to be 4,600 counts. The approximated number of 3γ accidental coincident events would be 3.

3.2 Coincidence PsARS Algorithm

A coincidence PsARS algorithm was developed in order to process output XIA data. The code was written as an Igor Pro Procedure file. Igor Pro is a data analysis and programming software tool that is also used as the GUI XIA interface. This section outlines the methodology of the algorithm. The full code is attached in Appendix F.

Once compiled and executed the algorithm inputs the data collected from the six PMT channels as Igor Waves. In particular only the energy and timing data is used, both of which are outputted as digital units. Using the experimentally determined energy fit, the energy digital units are converted into keVs for each channel. The program then discriminates the 3γ counts based upon energy values. All triggered channels must have energy less than 380 keV and the sum must

not be less than 920 keV or exceed 1120 keV. The 920 keV and 1120 keV numbers were determined based upon the experimentally determined energy resolution of 10.3 % at 514 keV.

Following the 3γ count energy discrimination, the true 3γ counts are further separated by shortening the coincidence timing window to 50 ns, the DGF-4C resolving time. This time corresponds to a net difference of one digital timing unit. Because only three of the four active 3γ PMTs will trigger for each event, one channel must be excluded from the coincidence timing discrimination. The algorithm sets the PMT channel with no triggered energy count equal to the digital timing unit of channel 1. If channel 1 is the channel not triggered, channel 1 is set equal to the digital timing unit of channel 2. If the sum of the difference in digital timing units exceeds 1, corresponding to a difference in coincidence timing by 50 ns ± 12.5 ns, the count is rejected. Otherwise the count is recorded as a 3γ event. On average 25 % of recorded counts with coincidence windows of one digital unit (50 ns), will register as being coincident only in a window of two digital units (75 ns). This is because 25% of what otherwise would have been considered a 3γ count gets rejected because the channel not triggered adjusted its timing unit to that of the channel that was different from the others by one unit. This causes the sum of the timing difference between all channels to be two timing units (75 ns) and thus not registered as a 3γ count. To correct for this a 25 % factor is added to only the 50 ns terms.

The 2γ events are also discriminated in a similar fashion. The energy is discriminated by assuring that neither recorded count is below 460 keV or above 560 keV. If the difference in the digital timing units is exceeds 1, once again corresponding to a difference in coincidence timing greater than 50 ns, then the count is rejected. Otherwise the count is recorded as a 2γ count.

The algorithm creates several histograms that are useful in analyzing data, in particular energy diagrams of each channel, energy diagrams of both 3γ and 2γ counts, and timing distribution diagrams. As a final step the algorithm calculates the 3γ/2γ ratio by summing the recorded counts and applying the theoretical and experimentally determined correction terms. In

particular the background terms from both 3γ and 2γ events (count rate and data run time must be specified), several 3γ correction terms, and a 25% correction term applied to the 50 ns 3γ counts as previously discussed. All of which can play a significant factor in determining the true 3γ/2γ ratio.

3.3 3γ Correction Terms

To determine an accurate 3γ/2γ ratio based upon coincident PsARS measurements, a multitude of correction terms must be determined: The true 3γ counts that get discriminated based upon energy, the geometrical issues that arise for 3γ counts that are not present for 2γ counts, the correction factor based upon the requirement to capture three gamma rays as opposed to two, and the difference in energy efficiency for 3γ relative to 2γ events.

The first and most straight forward correction term to determine is the 3γ counts that are discriminated based upon energy. This factor is determined by integrating Equation (17) between 130 and 380 keV and subtracting that value from one. Figure 22 graphically demonstrates this region of corrected counts. As illustrated by Figure 22, bases upon the integral of this region, 26.9 percent of 3γ counts are discriminated based upon energy.

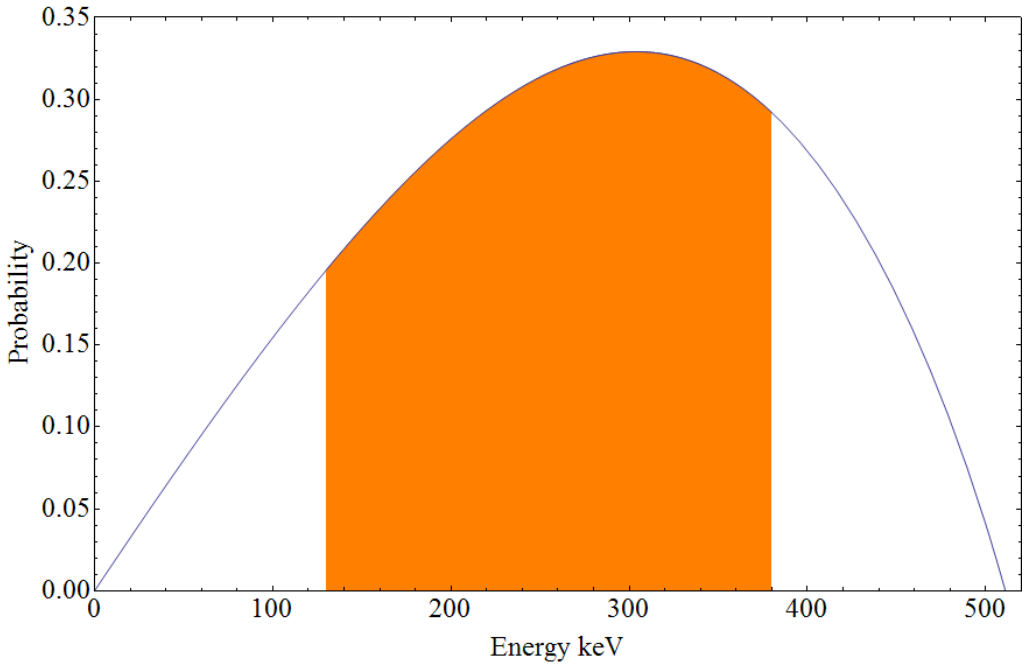

Figure 22: Coincident 3γ acceptance energy window

A geometric correction factor was also determined to correct for geometric constraints not present for 2γ counts. Because the two active 2γ detectors are 180° apart from each other and 2γ annihilation photons are emitted at approximately 180° apart in the laboratory frame, all true 2γ counts recorded by one detector can be detected by the other. This is not true for 3γ events. Because the NaI ring detector is not a 4π detector, two of the three photons released may be captured within one section of the NaI crystal that is an active 3γ section, while the other may only propagate through an inactive 3γ region. This geometrical correction can be determined by reinvestigating Equations (18) and (19).

$$m = 0: P(\theta) = \frac{1}{2}(\mathrm{Sin}(\theta)^2\psi(k) + 0.5 * (3\mathrm{Cos}(\theta)^2 - 1)\phi(k))$$

$$m = \pm 1: P(\theta) = \frac{1}{4}((1 + \mathrm{Cos}(\theta)^2)\psi(k) - 0.5 * (3\mathrm{Cos}(\theta)^2 - 1)\phi(k))$$

Where

$$\psi[\mathrm{k\_}]:=8\left(\frac{2-k}{k}+\frac{2(1-k)}{k^2}\mathrm{Log}[1-k]+\frac{k(1-k)}{(2-k)^2}-2\frac{(1-k)^2}{(2-k)^3}\mathrm{Log}[1-k]\right)$$

$$\phi[\mathrm{k\_}]:=8\left(\frac{k}{2(2-k)^2}-\frac{(1-k)}{(2-k)^3}\mathrm{Log}[1-k]-4\frac{(1-k)}{k^3}-\frac{(2-k)^2}{2k^3}-3(2-k)\frac{(1-k)}{k^4}\mathrm{Log}[1-k]\right)$$

While keeping in mind the probabilities of individual photons propagating at relative angles from each other.

$$\frac{\mathrm{dP}}{P}=\frac{3((1-\mathrm{Cos}(\alpha))^2+(1-\mathrm{Cos}(\beta))^2+(1-\mathrm{Cos}(\gamma))^2)}{2\pi(\pi^2-9)}\frac{\mathrm{Sin}(\alpha)\mathrm{Sin}(\beta)\mathrm{Sin}(\gamma)}{(\mathrm{Sin}(\alpha)+\mathrm{Sin}(\beta)+\mathrm{Sin}(\gamma))^3}\mathrm{d}\Omega\mathrm{d}\alpha\mathrm{d}\beta$$

The main inactive 3γ regions of interest are the active 2γ regions, active 3γ regions that have already triggered an event, and empty space in which no NaI crystal is present. A determination of the geometrical correction factor can be approximated by making the assumption that for all 3γ events emitted nearly perpendicular to the horizontal NaI detector plane, that on average photon events $\frac{1}{3}\pi$ to $\frac{2}{3}\pi$ radians from the axis along a single detected incident photon will not be detected. This inactive region is caused by the presence of the 2γ detectors as demonstrated by Figure 11. An additional approximation is that all emissions will occur with respect to only two planes: the horizontal plane, parallel to the detector, and the vertical plane, perpendicular to the detector. The sum of both correction factors should be a reliable approximation to the true geometrical correction factor.

The active 2γ region represents an average approximate angle between $\frac{1}{3}\pi$ and $\frac{2}{3}\pi$ and $\frac{4}{3}\pi$ and $\frac{5}{3}\pi$ for all 3γ events that occur in a plane perpendicular to the NaI detector. This angle

must be corrected for both γ and β, the angles between the first photon and the second, and the first photon and the third.

The approximate angle to correct for the active 3γ regions that have already triggered an event can be determined along a plane perpendicular to the NaI detector. Angels between 0 and $\pm \frac{1}{6}\pi$ for all α, β, and γ angles were corrected for. This angle represents the minimum angle required for all three 3γ photons to propagate through separate active 3γ regions.

An additional angle correction is required for the region of space not occupied by any NaI scintillation crystal. The angle corresponding to this empty space in which no NaI crystal is present was determined to be

$$\theta_{\text{Open}} = \text{Tan}^{-1}(\frac{D}{L}) \tag{38}$$

where D is the open diameter of the hallow portion of the NaI cylinder is (9.5 cm), and L is the length of the NaI cylinder (18 cm). This results in an angle, θ , of 0.486 radians. Therefore the correction factor of 3γ photons emitted with an angle between 0 and 0.486 radians, either perpendicular or tangential to the detector, would not propagate through an active region and therefore must be corrected for. The coincident correction factor can be calculated by integrating the probability that a 3γ photon be incident to an inactive 3γ region. The 3γ coincident correction factor, as determined by numerical integration, is

$$3\gamma_\theta = \frac{1}{2}(\int_{-\theta_{\text{Open}}}^{-\theta_{\text{Open}}} P(\theta)_{m=\pm1\,,m=0}\, d\theta + \int_{\frac{1}{3}\pi}^{\frac{2}{3}\pi} P(\theta)_{m=\pm1\,,m=0}\, d\theta + \int_{\frac{4}{3}\pi}^{\frac{5}{3}\pi} P(\theta)_{m=\pm1\,,m=0}\, d\theta) \tag{39}$$

$$3\gamma_\theta = 0.524$$

Over 50 percent of all 3γ events will not be detected due to 3γ/2γ detector geometry.

The final correction term to be applied for coincident PsARS experimentation, is the correction factor produced from the difference in detection efficiency for 3γ/2γ events. For 2γ

events, the probability of detection is the sum of both 2γ channel's intrinsic efficiency for 511 keV photons squared. The squared portion is required because two photons must be detected in coincidence for an event to trigger. For 3γ events, the probability of detection is the sum of all four 3γ channel's intrinsic efficiency cubed. The cubed portion is required because three photons must be detected in coincidence for an event to register. The 3γ/2γ correction factor based upon detection efficiencies can be calculated by

$$\frac{3\gamma}{2\gamma}\epsilon = \frac{(\epsilon[511\text{keV}]_{\text{Mod2Ch1}} + \epsilon[511\text{keV}]_{\text{Mod2Ch2}})^2}{(\epsilon[3\gamma]_{\text{Mod1Ch0}} + \epsilon[3\gamma]_{\text{Mod1Ch1}} + \epsilon[3\gamma]_{\text{Mod1Ch2}} + \epsilon[3\gamma]_{\text{Mod1Ch3}})^3} \quad (40)$$

In order to determine the 3γ channel efficiencies, a weighted probability function specified by Figure 22 was used in conjunction with the best fit lines illustrated by Figure 15. The product of these two was integrated over the specified energy range of 130-380 keV. This calculation provides the intrinsic energy efficiency for 3γ events based upon the distribution of said events. The total 3γ weighted intrinsic efficiency was determined to be 0.2366 ± 0.04. Where the uncertainty was determined as a sum of each individual channel's uncertainty.

This level of uncertainty creates a large problem when attempting to determine the proper correction factor for 3γ/2γ events based upon intrinsic efficiency. Exercising the full range of values within the uncertainty of only the 3γ events, results in a 3γ/2γ efficiency correction factor between 0.43 and 1.22. In other words, the results of this correction factor demonstrates that 2γ counts should be anywhere between doubled to reduced by a fifth in order to reflect the proper 3γ/2γ ratio of annihilation radiation. Due to this high level of uncertainty, no correction factor based upon efficiency should be applied. However, this ignored efficiency correction is common among PsARS detectors, and should not influence the results beyond a calibration factor if necessary.

The total 3γ/2γ correction factors can be determined by

$$3\gamma_{\text{Total}} = (\frac{3\gamma}{2\gamma}\epsilon * 3\gamma_{\text{Counts}}) + 3\gamma_{\text{Energy}} * (1 + 3\gamma_{\theta}) * 3\gamma_{\text{Counts}} + 3\gamma_{\theta} * (1 + 3\gamma_{\text{Energy}}) \quad (41)$$

with

$$3\gamma_{\text{Energy}} = 0.269$$

$$\frac{3\gamma}{2\gamma}\epsilon = 1$$

$$3\gamma_{\theta} = 0.524$$

The sum of the 3γ/2γ correction factor applied to the recorded 3γ counts is therefore determined to be

$$3\gamma_{\text{Total}} = 2.08$$

Applying correction factors in this manner, assumes that each correction factor is independent of each other. This cannot be absolutely true, but should be a sufficient approximation because the counts that will be most affected by the geometrical correction factor will be those 340 keV counts emitted at 120^{o} of each other, which are not discriminated against based on energy.

3.4 PsARS Analysis of Copper

The coincident PsARS method was used to test a single crystal copper sample in order to validate the assumptions and protocol to be used for coincident PsARS experimentation. Care was taken to ensure that little to no source correction terms would be necessary due to extraneous material such as oxygen or grease.

The sample was prepared by depositing 60 µL of a radioactive NaCl solution using a 22 gauge syringe onto one face of a single crystal 10 mm x 10 mm x 1 mm copper sample. The copper sample was cleaned using methanol prior to radioactive deposition. The NaCl solution carried a ^{22}Na source of 9.585 uCi (15 Sep 2009) activity in 2 mL of water. During radioactive deposition, the copper sample was placed on a 1”x 3” copper piece positioned on top of a hot

plate. Following radioactive placement, the hot plate was used to evaporate the NaCl onto the copper sample at approximately 50 ^{o}C. The additional larger 1"x 3" copper piece was used to insure little to no oxidation during the heating phase. The NaCl evaporated within 15 minutes, requiring four runs to fully deposit the intended amount of solution. Upon cooling, an identical 10 mm x 10 mm x 1 mm copper sample was placed onto of the already radioactive sample on a thin piece of masking tape, using cardboard pieces to avoid contamination, and cut to preferred dimensions. Figure 23 is a photograph of the completed copper source. The intended deposited radioactivity was 0.3 μCi.

Figure 23: Radioactive single crystal copper sample

In order to determine activity of the copper sample a Canberra low energy germanium detector with background shielding was used. The activity was determined by measuring the count rate within the full energy peak of 511 keV photons with a known radioactive ^{22}Na sample and comparing to the full energy peak produced from the copper sample, as demonstrated by Equation (42). A plastic holder was placed into the background shielding cylinder with a divider located 4" above the germanium detector, as shown in Figure 24.

$$\mathbf{Activity_{unknown}} = \frac{\mathbf{Activty_{known}}}{\mathbf{Counts_{known}}} \mathbf{Counts_{unknown}} \quad (42)$$

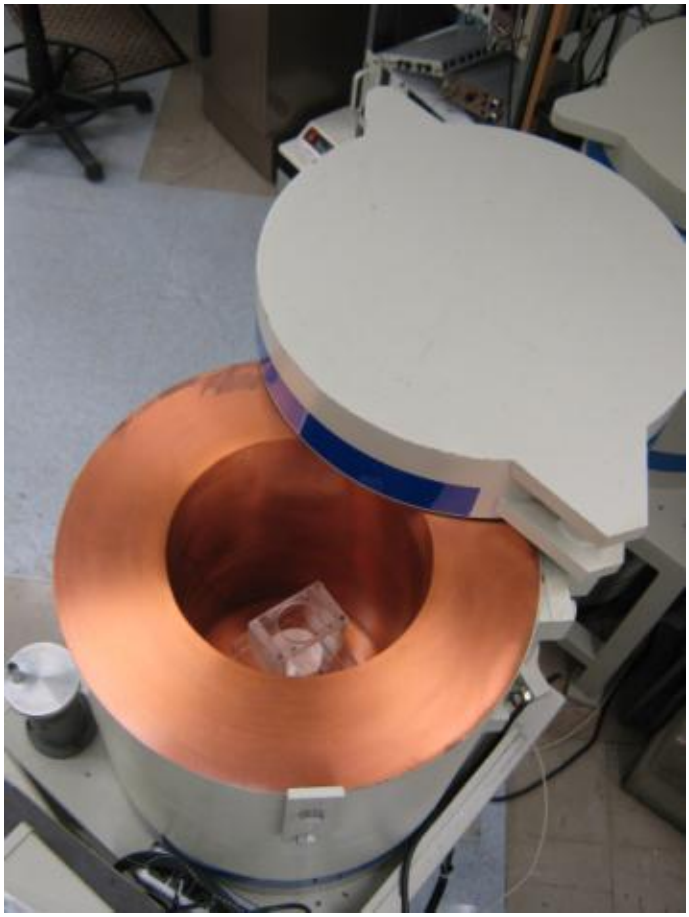

Figure 24: Canberra low energy germanium detector used to determine activity of unknown radioactive samples

A 53.96 μCi (1 Jan 2005) ^{22}Na planchette source was placed on top of the plastic divider to experimentally determined the radioactivity of the copper sample. Using this method, the activity of the copper sample was determined to be 0.29 μCi (22 Dec 2009).

Once the copper sample was verified to contain the intended amount of radioactivity, coincident PsARS was performed. The 3γ/2γ holder shown in Figure 12 was used to place copper sample near exact center of the NaI ring detector. A total of 100,000 buffer spills were selected.

The experiment run time was 1 hour 30 minutes, with a detector live time of 1250 seconds and an average input count rate of 2025 cps. The .dat file produced from experimentation was imported into the developed 3γ/2γRatioProcedure1.2 attached in Appendix E. The total number of coincident 3γ counts was 235, the corresponding number of coincident 2γ counts was 182,982 . The total spectrum of 2γ spectrum post energy (460-560 keV) and time (50 ns) discrimination is graphically demonstrated by Figure 25. Figure 25 illustrates that the energy calibration between the two channels was successfully administered, as demonstrated by the near Gaussian behavior. This figure also demonstrates how the 511 keV annihilation photons dominate the 2γ counts as expected, relative to the 3γ counts highlighted in Figure 26.

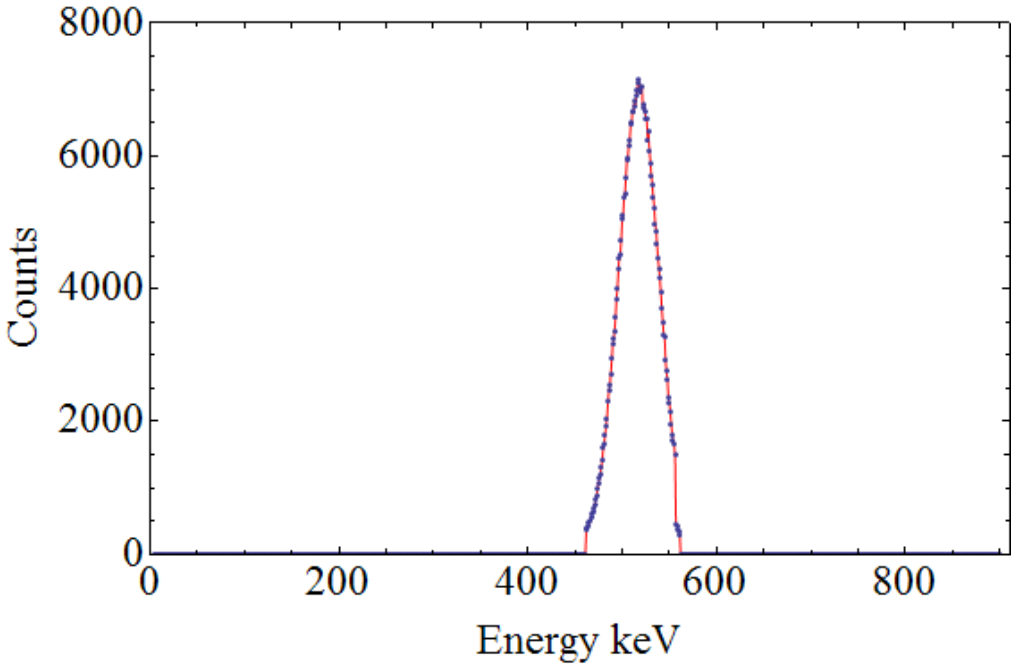

Figure 25: 2γ spectrum coincident in 50 ns and discriminated by energy

The corresponding correction to the experimentally determined 3γ counts due to chance coincidence was 2 counts, the correction 2γ chance coincidence was 1,597 counts. Subtracting

the chance coincidence terms and applying the 2.08 correction factor results in a 3γ/2γ annihilation of radiation ratio of $\frac{1}{370}$ or 0.99 ± 0.08 of the expected $\frac{1}{372}$ ratio.

Analyzing the total number of counts in relation to the runtime, known efficiency of all detectors, and correction factors can be used for additional verification. As illustrated by Equation (43), in which t is the runtime, ε is the efficiency of each PMT, and the 0.9 factor represents the β^+ decay probability, the expected 2γ counts is calculated to be 196,000 ± 30,000 counts.

$$2\gamma\text{Counts} = 0.9t(\epsilon_{\text{mod2ch1}} + \epsilon_{\text{mod2ch2}})^2\text{Activity} \tag{43}$$

Well within the uncertainty of measurement, the correlation between expected and experimentally determined 2γ counts further verifies the coincident PsARS method. Additionally the total number of expected 3γ counts can be determined by

$$3\gamma\text{Counts} = 0.9t(\epsilon_{\text{mod1ch0}} + \epsilon_{\text{mod1ch1}} + \epsilon_{\text{mod1ch2}} + \epsilon_{\text{mod1ch3}})^3\text{Activity} * \frac{1}{3\gamma_{\text{TotalCorrection}}372} \tag{44}$$

that results in a expected 3γ count of 214 ±100, where the large uncertainty once again reflects the uncertainty in efficiency taken to the third power. To attempt further verification, the final 3γ coincident (50 ns) spectrum with energy discrimination is demonstrated by Figure 26.

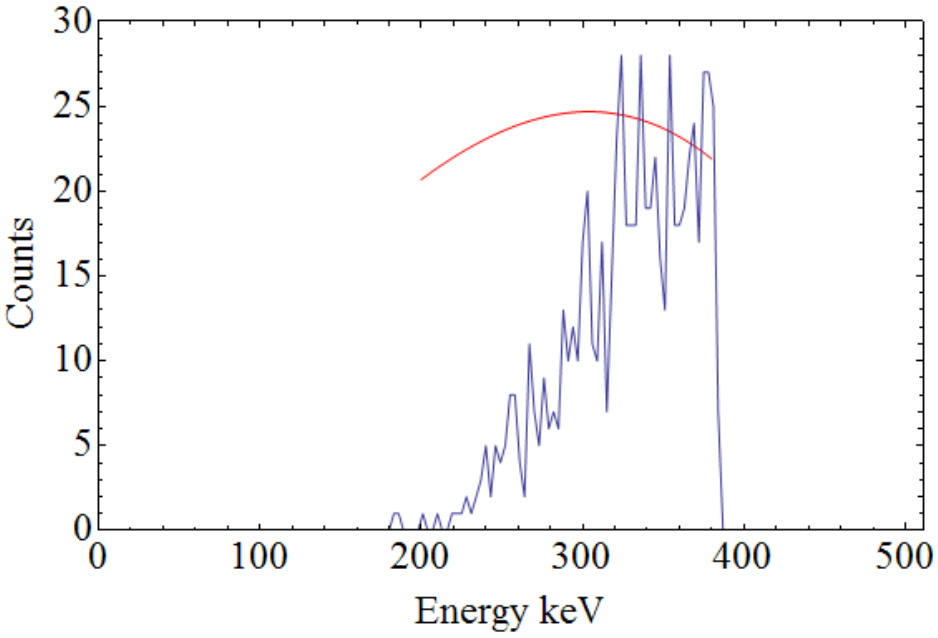

Figure 26: 3γ coincidence spectrum following analysis using developed 3γ/2γRatioProcedure1.2 compared to theoretical results

Figure 26 demonstrates the 3γ spectrum from post experimental discrimination compared to the theoretical 3γ spectrum. The 180-250 keV energy range appears lower than the theoretical results indicate. The main justification for this is that these lower energy terms are most probably emitted within a small angular deviation from an additional 3γ photon. Nearly all photons deviating only slightly from an addition 3γ annihilation of radiation will impact the same scintillating section, and therefore not register as a separate event. These lost events are taken into account through the geometric correction factor.

The general form of the experimental upper bounds near 340 keV appears to coincide with theoretical predictions. However, the far 380 keV energy range appears too pronounced. At first glance it appears as if near the Compton edge a large number of coincident events occur. Further investigation, in particular in relation to Figure 17, indicate that if these 3γ coincident events were in fact Compton events, than the 200 keV region would also appear more pronounced. Because

the 200 keV region is not well pronounced these additional counts are most likely not due to Compton events. The most likely explanation of the misshaped end (380 keV) portion of Figure 26 is that the number of higher energy photons were not as influenced by the geometric correction terms. In particular the geometric correction term would greatly influence the roughly 300 keV terms. In a plane perpendicular to the NaI ring detector, these photons are emitted at nearly 120^{o} of each other, assuring that at least one of these photons will always impact a 2γ PMT and therefore not be recorded as 3γ events. In order to prove this theory, the full detector would need to trigger from 3γ events.

Utilizing all PMTs as 3γ detectors, while simultaneously using two to detect 2γ events was accomplished by splitting the pulse exiting two of the original 3γ Ortec pre-amplifiers and connecting to both DGF-4C modules. Each channel was recalibrated to correct for the change in pulse splitting. The coincident patter was adjusted for Module 2 to include 3γ counts for all channels, as well as the 2γ counts for the two channels that previously did so. Following adjustments, a ^{22}Na 3γ spectrum was obtained. The 3γ spectrum contained interference peaks characteristic of those highlighted in Figure 10, but over a broader energy range. These interference peaks were also present in the 2γ spectrum. Although adjusting coincident count measurements to include additional detectors should double the count rate, this method was not demonstrated due to the inability to eliminate noise peaks in the coincidence spectrum.

3.5 Non-Coincident PsARS

A converse PsARS method was developed by strictly monitoring the ratios between 340 to 400 keV photon counts relative to the 511 keV full spectrum peak, and normalizing to a known 3γ/2γ ratio annihilation of radiation standard. The 340 keV photon and higher is chosen because counts strictly conjured due to Compton events will be suppressed because the Compton edge is located at this near exact energy value, determined by

$$E_{\text{Compton}} = \frac{2E^2}{2E + m_e c^2} \tag{45}$$

The predominating interaction at these photon energies is Compton scattering and a relatively large peak will be found near this Compton edge.

This non-coincident PsARS method requires two correction factors to determine 3γ/2γ ratios of annihilation of radiation. Both of these correction factors are only applied to the relative difference of 3γ spectrum compared to a calibration sample. A count correction factor, a $\frac{2}{3}$ correction, was based on the total number of recorded counts 3γ compared to 2γ. An energy correction factor was also determined through the integration of Equation (17) from 340-400 keV, as demonstrated by Figure 22 with a different energy range. This energy correction factor results in 5.56. The combined correction factor for non-coincidence measurements was determined to be 3.7. Relative efficiency or geometrical correction factors are not required for these measurements because of the use of a known PsARS standard. This standard is used as a calibration, intrinsically resolving correction factors that may arise due to differences in 3γ,2γ measurements. As determined through previous PsARS measurements the copper sample 3γ/2γ ratio of annihilation of radiation was determined to be equal to $\frac{1}{372}$, and would be used as the calibration standard.

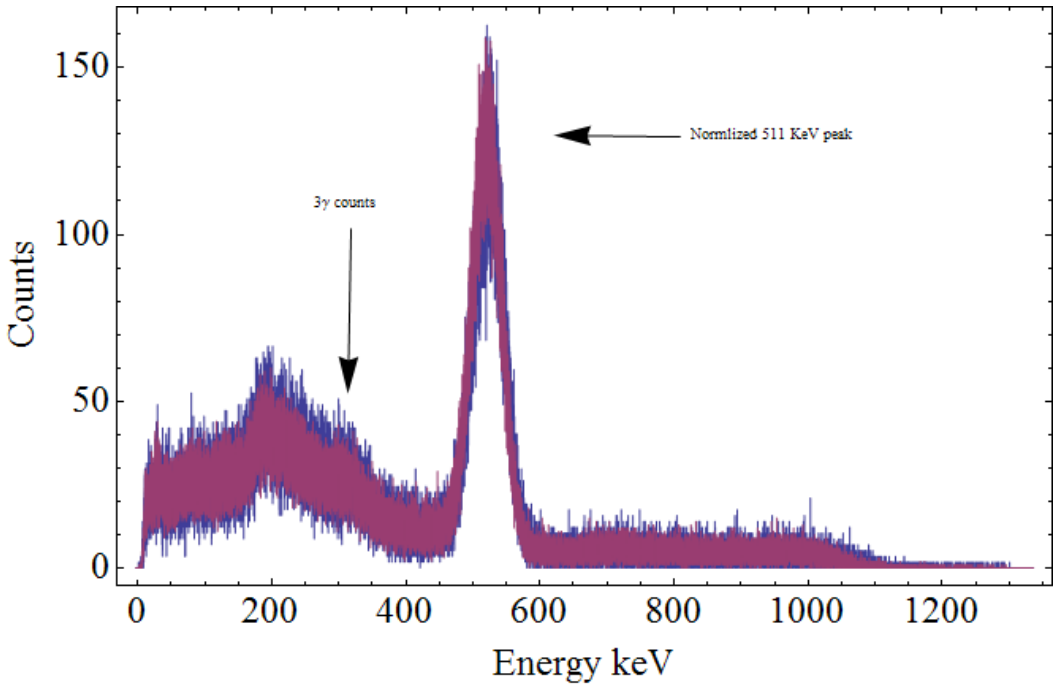

Figure 27: Plot of non-coincidence method and additional 3γ counts demonstrated relative to copper standard

Figure 27 highlights the small difference between the calibration sample spectrum, $\frac{1}{372}$, and a sample with an unknown 3γ/2γ ratio. Although small, this difference in spectrum counts has been demonstrated previously by others to be a reliable PsARS method [37].

3.6 Dodecaborate Solutions

3.6.1 Overview

An AFIT fast-fast PALS spectrometer incorporating two BaF_2 scintillation detectors was previously characterized [5] to have a 197 ps full width of half maximum (FWHM). This PALS spectrometer was employed to measure a model explosives system incorporating various concentrations of potassium nitrate and potassium dodecahydrododecaborate (dodecaborate). Radioactive carrier-free ^{22}NaCl was added to the solutions to serve as the positron emitter and birth indicator. Following analysis using the PALSfit software program, positron lifetimes as

well as species intensity were determined. The intensities and lifetimes of positronic species were left as guesses, determined through PALSfit least squared fit routines. Figure 28 demonstrates the results of the dodecaborate PALS analysis [38]. Of key importance is the suppression of p-Ps at concentrations above 10^{-2} M.

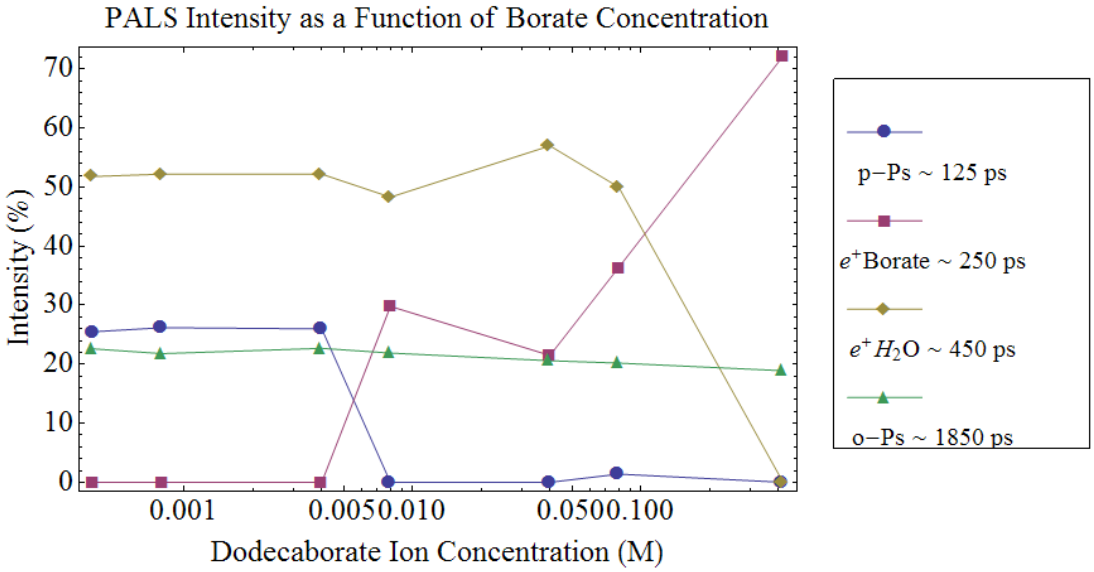

Figure 28: Dodecaborate PALS analysis

In most materials, to include potassium nitrate solutions, only the ortho-positronium species are suppressed [18] or positronium formation altogether is suppressed [39]. The fundamental difference for ortho-positronium being the lifetime, and therefore the likelihood of a conversion, spin flip, or other process to occur before annihilation. The ortho-positronium, the longer lived species (140 nanoseconds in vacuum), survives long enough to undergo a physical change, generally annihilating long before the expected lifetime in a material (a few nanoseconds). In most solutions, the para-positronium term with a lifetime of 125 ps does not live long enough to undergo a significant change before annihilation. According to the data presented by Figure 28 this does not appear to be the cause for dodecaborate solutions above a 10^{-2} concentration. Further evidence to support the claim that para-positronium is suppressed in dodecaborate

solutions appears when investigating the average positron lifetime, to include all terms. Figure 29 demonstrates how the average positron lifetime changes with increasing dodecaborate concentration.

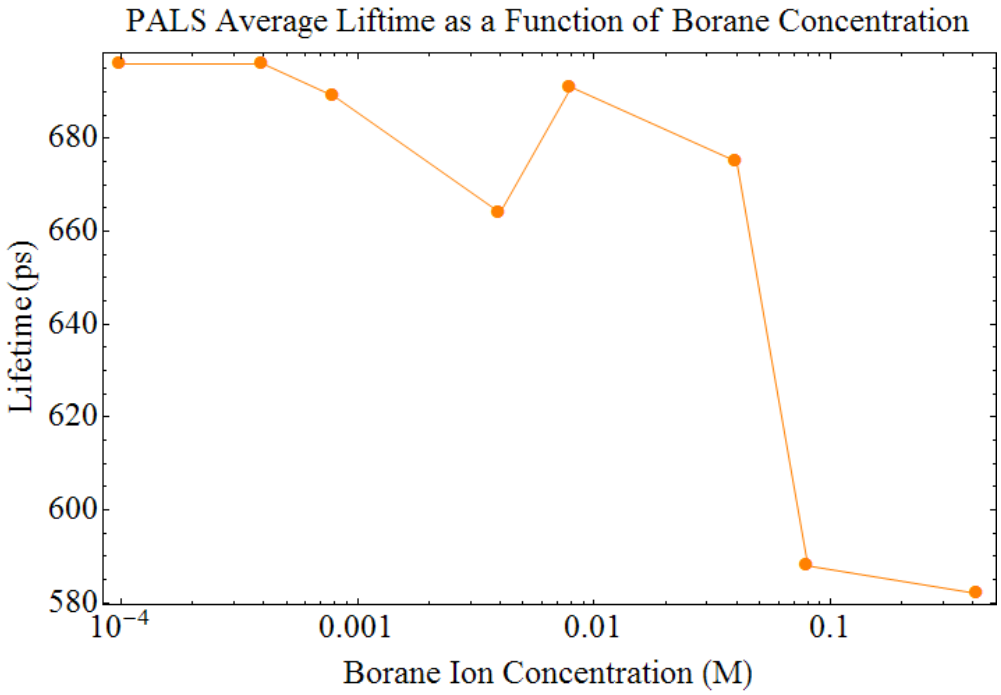

Figure 29: Average positron lifetime

As the concentration of dodecaborate increases the amount of positronic species associated with water, 450 ps lifetime, should decrease relative to the positronic species of dodecaborate, 250 ps lifetime. This increase in dodecaborate concentration should result in a continual decline in the average positron lifetime. As demonstrated by Figure 29 this is preciously the case for all increases in concentration excluding 0.008 M, which is preciously the data point at which the para-positronium (shortest lifetime) species appears to be suppressed.

The suppression of para-positronium may be due to a positron precursor interaction or something else entirely. Further data is required in order to investigate this phenomenon. Both PsARS methods were used to determine the end spin state of annihilation radiation. Para-

positronium annihilation events result in 2γ emission while ortho-positronium result in 3γ emissions. By investigating how this ratio changes with varying dodecaborate concentration, a change in the 3γ / 2γ ratio would correspond to a change in the spin state of positron species. For para-positronium suppression one would expect an increase in the 3γ / 2γ ratio, corresponding to additional triplet state annihilation events.

3.6.2 Dodecaborate Solution Preparation

A total of 6 dodecaborate solutions were prepared using previously mixed concentrates, a single solution of water was also assembled. An oxygen free environment was ensured through use of a nitrogen purged glove box. ^{22}Na was then combined using a 22 gauge syringe to insert 0.6 mL of NaCl solution with activity of 9.585 uCi (15 Sep 2009) in 2 mL of water. The volume of radioactive solution was estimated by counting drops within the encapsulated dodecaborate solutions. The intended amount of deposited radioactivity was 0.30 µCi.

Following an identical procedure as outlined in Section 3.4, the activity of all dodecaborate solutions was determined. The activities and concentrations of all solutions are shown in Table III.

Table III: Dodecaborate solutions concentration and activity

Sample ID	Dodecaborate Concentration (M)	Activity (µCi)
Sample B	0.04	0.30
Sample C	0.008	0.36
Sample D	0.004	0.34
Sample E	0.0008	0.31
Sample F	0.0004	0.43
Sample G	0	0.34
Sample H	0.00144	0.35

As Table III indicates, all solutions had at least 0.30 μCi of radioactivity. The highest activity solution being Sample F with 0.43 ± 0.03 μCi.

3.6.3 Dodecaborate PsARS measurements

Dodecaborate concentrations and activities shown in Table III were measured using coincident PsARS. In order to determine measurement sensitivity, Sample G, water, was measured six separate times with results shown in Table IV. The detector runtime was approximately an hour with a detector livetime of approximately 1500 seconds. Correction factors to include background were taken into account in order to determine the 3γ / 2γ ratio.

Table IV: Water sample 3γ/2γ ratio

Sample	3γ / 2γ (1/372)
Sample G	1.25
Sample G	1.14
Sample G	1.19
Sample G	1.20
Sample G	1.16
Sample G	1.29

As Table IV demonstrates the coincident PsARS measurement is incredible sensitive to placement within the detector. Alignment was conducted by placing sample on the 3γ / 2γ holder and then aligned towards end of the NaI detector by matching marked line on holder with straight edge. The results from this test conclude that the 3γ / 2γ ratio of annihilation of radiation for Sample G (water) is 1.2 ± 0.1 ($\frac{1}{372}$). This result differs slightly from the approximation based upon lifetime data for water of 1.4 [40]. The potential difference in dodecaborate solutions should be slight, and most likely will not appear within this uncertainty. However, larger differences could be observed.

Table V is the results following PsARS analysis for dodecaborate solutions, that are graphically represented by Figure 30. Figure 30 and Table V clearly demonstrate that there is little difference between Sample C and Sample D, dodecaborate concentrations of interest. Where the uncertainty was determined to be the standard deviation as observed through multiple measurements of Sample G. The only data point outside of the uncertainty labeled for water is Sample B, 0.04 M.

Table V: Dodecaborate solutions coincident PsARS measurements

Sample	3γ / 2γ (1/372)
Sample B	1.37
Sample C	1.22
Sample D	1.14
Sample E	1.32
Sample F	1.19
Sample G	1.21
Sample F	1.14

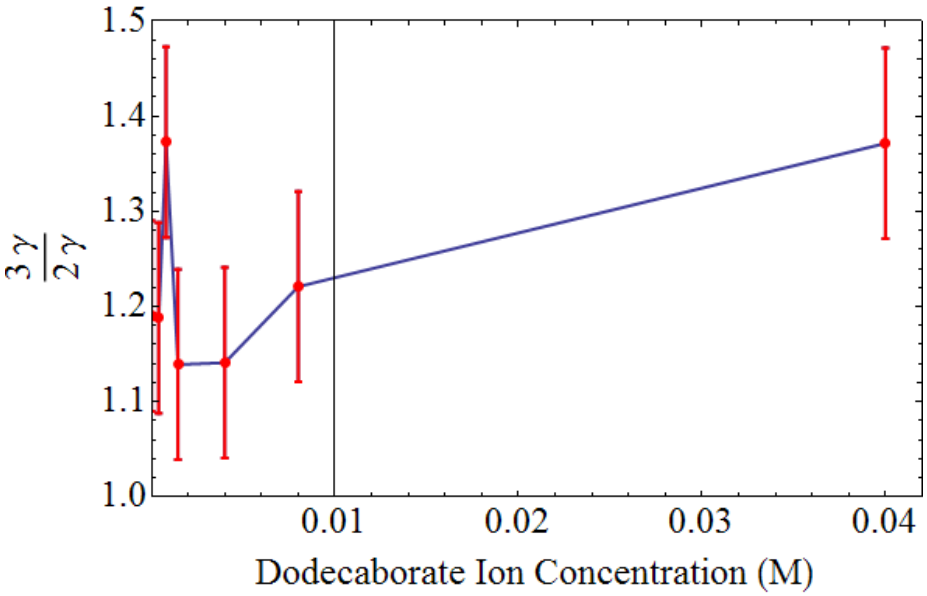

Figure 30: PsARS data for dodecaborate solutions using coincidence method

Additionally the non-coincident PsARS method was used to determine 3γ / 2γ ratios of the dodecaborate solutions. For the non-coincident PsARS method, sample B was measured three times following the sample handling process as the coincident PsARS method resulting in 3γ / 2γ ratios of 1.25,1.26 and 1.30 1 ($\frac{1}{372}$). Results indicate that the non-coincident PsARS method has less uncertainty than the coincidence method, but that the measurement may still be too insensitive to determine a distinct difference between samples. As Table VI and Figure 31 demonstrate, once again Sample B appears to be the only sample with a difference in 3γ / 2γ ratio larger than the quoted uncertainty. Where the uncertainty was determined to be the standard deviation as observed through multiple measurements of Sample B.

Table VI: Dodecaborate solutions non-coincident PsARS measurements

Sample	3γ / 2γ (1/372)
Sample B	1.27
Sample C	1.21
Sample D	1.20
Sample E	1.23
Sample F	1.22
Sample G	1.25
Sample F	1.20

Results from both PsARS methods reproduce the expected 3γ / 2γ ratio within some uncertainty for water sample, Sample G [40]. However, no results indicate any affirmative results either confirming or refuting para-positronium quenching at the observed concentrations. However, the PsARS data from both coincidence and non-coincidence methods indicate that as the dodecaborate concentration increases to 0.04 M that the 3γ / 2γ ratio increases. This increase further indicates the existence of positronic dodecaborate species and affirms that dodecaborate does not quench positronium formation.

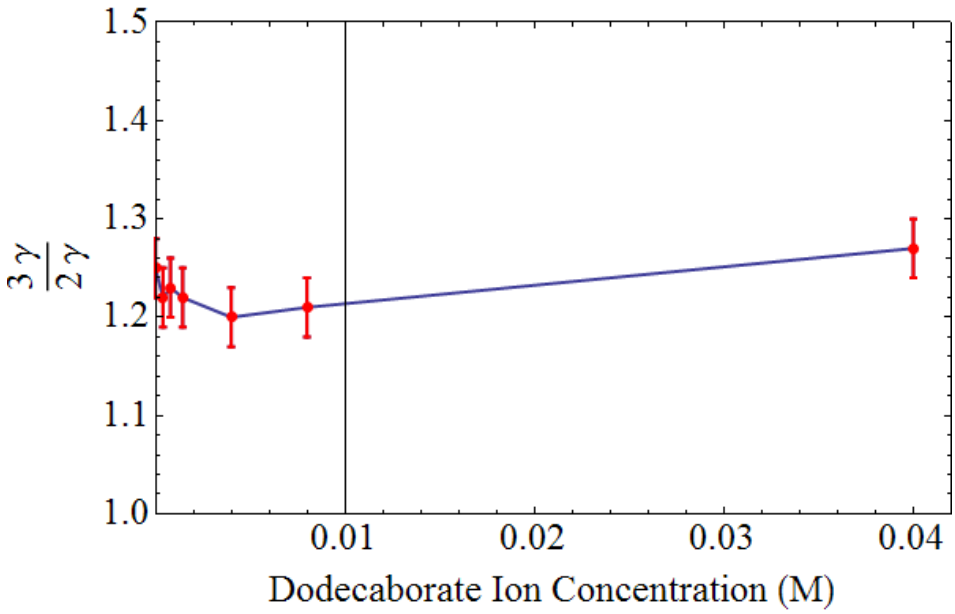

Figure 31: PsARS data for dodecaborate solutions using non-coincidence method

3.6.4 Dodecaborate Conclusion

Dodecaborate samples with varying concentration were analyzed using two PsARS methods. Both methods indicated that the only solution to contain a 3γ / 2γ ratio different from other solutions by a value greater than the uncertainty in the measurement is Sample B, 0.04 M. These results provide further evidence that the ortho-positronium species and therefore positronium species are not quenched at higher dodecaborate concentrations. These results also provide further evidence affirming the existence of positronic dodecaborate species that were theoretically predicted [9]. However, PsARS data did not provide the insight necessary to determine if para-positronium quenching is present in samples. Either the dodecaborate solutions constructed for these measurements underwent significant physical change from previous measurements [39], or the PsARS methods used did not have the precision necessary to confirm para-positronium quenching at 10^{-2} M. In order to verify which solution appears most accurate, further PALS analysis with the dodecaborate solutions is required. Both coincident and non-

coincident PsARS methods appear to be determining the correct absolute 3γ / 2γ annihilation of radiation ratios, within their known uncertainties of approximately 10 and 5 percent.

4 Silver Nanoparticle Array Construction on Gold Capillary Tube

4.1 Overview

Theoretical calculations have predicted that in crossed magnetic and electric fields positronium lifetimes can be extended due to the formation of stable outer wells [41]. In the presence of a strong electric field, the positron electron pair can polarize. An outer state may still be created, but the positronium system will not be protected within a deep ground state (well) from external energy events. The future aspirations of this research are to validate the existence of positron-electron outer well states due to the application of an external electric field by monitoring the lifetime of positron annihilation. To experimentally validate this theoretical prediction, external electric fields will be applied to a positron source. The initial step in development of such a source is to create an environment that is favorable for positronium formation, as well as create the surface features necessary for the desired electromagnetic field effects.

All elements and compounds can have small deformities or oxides, especially at the surface, allowing for positronium formation. However, only certain elements and compounds are known to bind with a positron to form positronic species. Due to the columbic repulsion of the positively charged nucleus, the positron formation for these elements and compounds occurs with a valance electron. One of the known elements that allows for positronium formations is silver [42]. The binding energy associated for para and ortho positronium states for silver is 0.158 eV with lifetimes of 429 ps and 22.42 ns respectfully.

The planned experiment requires a distribution of 10-50 nm sized silver nanoparticle arrays to be construction on the surface of gold coated capillary tubes with inner diameters of 0.7 mm. Figure 32 demonstrates the theoretical results from analyzing the field surrounding 200 nm sized gold particles connected to a gold surface [43]. The field effects near the tip produced a field enhancement factor of over 20,000 times the applied external voltage. The surrounding of this nanoparticles also produced a field enhancement on the order of 100. These large field enhancements will be necessary to polarize any positronium or positronic species. The local fields will have to begin to strongly affect the electric fields that bind the particles together. The columbic attraction between the positron and local electrons does not have to be overcome, but will need to be weakened in order to lower annihilation rates.

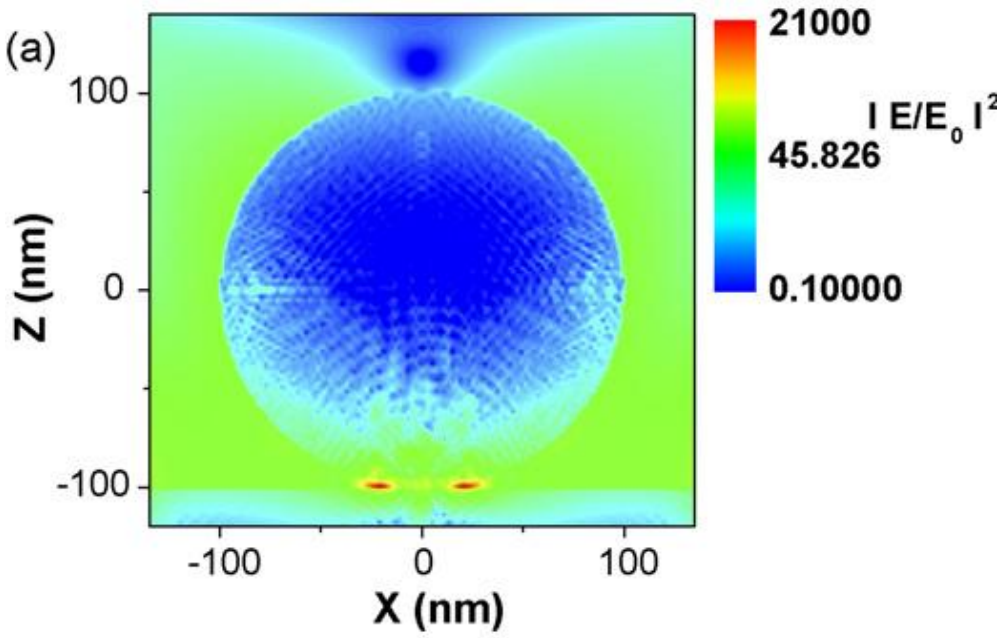

Figure 32: Localization of EM field [43]

This research focuses on the development of a radial positron source, as well as producing the capability to deposit silver nanoparticles on such a source. Once the capability is

demonstrated further research will investigate which possible array distributions are favorable to generate high local electric fields in the presence of an external field. This local electric field would be designed to polarize positronic species, whose effects can be monitored by investigation through digital PALS and PsARS measurements.

4.2 Gold Coating Capillary Tube

A thin capillary tube was chosen as the best candidate to provide a radially symmetric positron source. The capillary tubing had to be thick enough to provide support as an independent structure, but also thin enough to allow many of the positrons to reach the surface, where the intended field effects will be present. In order to determine the appropriate thickness a GEANT4 simulation was conducted to provide insight into appropriate tube thickness.

GEANT4 is a Monte Carlo particle tracker toolkit program designed for a wide variety of physics experiments [45]. GEANT4 has been validated in a multitude of experiments [46], in particular GEANT4 is used extensively for Positron Emmission Tomography (PET) applications [47]. A GEANT4 simulation of 100,000 positrons incident on silicon at the peak energy value of 240 keV was performed. 240 keV corresponds to the most probable positron kinetic energy value resulting from β+ emission, as demonstrated by Figure 1. The results of the analysis showed 50 percent of the positrons thermalized within 104 um of the silicon material. This distance should be considered the near maximum limit of capillary tube thickness for any similar polymer material.

Two custom designed segments of capillary tubing manufactured by Polymicro with silica layers of 65 ± 15 microns and 75 ± 20 microns with outer coating of polyimide of 25 μm were acquired for experimentation. Because the thickness of these optical fibers are near maximum thresholds, an additional electric field may be fundamental in providing the drift necessary for a majority of positrons to reach the capillary surface. For silver nanoparticle deposition a metal

layer is necessary to provide the affinity required for chemical attachment. This layer can also be used to provide the conductivity required for electrical contact in order to provide the external voltage difference between the outer capillary tubing and the vacuum walls (ground). Each capillary tube fiber is also designed with a 2.9 um silver inner layer. If an electrical contact can also be made with the inner silver layer, a small voltage drop between the outer and inner diameters may increase the likelihood of positronium formation on the surface of the capillary tube.

A thin (~ 200 nm) Au layer was deposited on the outer surface through a Torr Electron Beam Evaporation System (E-Beam) as shown in Figure 33. Developing a uniform and smooth layer of deposition is of chief concern. Each deposition involved hanging each capillary tube vertically on a stand, within the vacuum chamber of the E-beam. The capillary tube was connected to the stand by placing 22 gauge electrical wire firmly within the hollow portion of the tube. In order to provide a uniform coating the stand rotated during gold deposition. The E-beam machine measures deposited thickness, by monitoring the deposition rate onto a thin layer perpendicular to material vent. The system then estimates the deposition layer by assuming a one dimensional growth at a distance of 10". Due to the necessity of a rotator, additional deposition runtime would be required. For a true layer of approximately 100 nm, an E-beam system deposition of 250 nm was chosen. Prior to gold deposition, the capillary tube was cleaned with methanol to cleanse the surface of grease and dust particles.

Figure 33: Torr Electron Beam Evaporation System (E-Beam)

The complete gold coating process required approximately an hour to include vacuum roughing time as well as deposition, this is largely dependent upon the deposition rate, which varies between runs. Multiple capillary tubes can be coated at the same time. The uncertainty in the thickness is ± 10% . Following gold deposition the capillary tube was carefully placed within a plastic bag, and isolated to ensure minimal contact.

4.3 XRF Images of Gold Coated Capillary Tubing

An X-Ray Florescence (XRF) machine was used in order to ensure that a uniform coat of gold was deposited onto the capillary tubing. An XRF machine bombards samples with X-Rays

exciting generally K and L shell electrons. Ultimately these excited electrons release characteristic X-Rays that are measured by the XRF machine to identify elements within a sample. A 50 data point scan of 50 keV X-rays along the gold coated capillary tube resulted in the confirmation of both silver and gold. In particular the L shell of the gold and the K shell of the silver were identified using a 50 kV X-Ray tube voltage. The results are demonstrated by Figure 34.

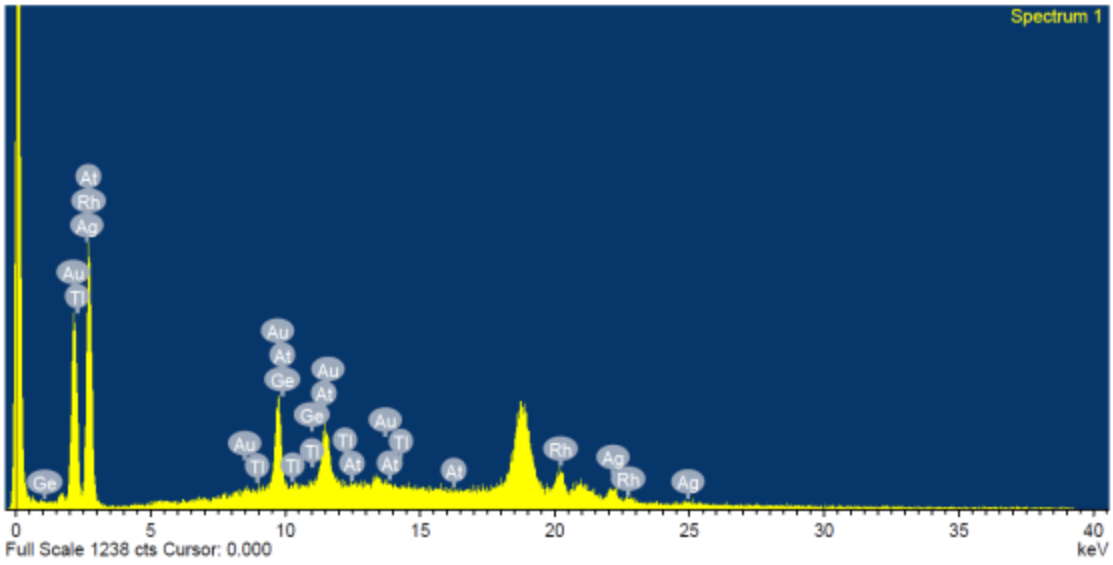

Elem.	Line	Mass [%]	3sigma	Atomic [%]	Intensity [cps/mA]
32 Ge	K	0.66	0.60	1.28	4.58
45 Rh	K	25.38	3.19	34.73	30.35
47 Ag	K	18.89	3.24	24.65	16.92
79 Au	L	54.53	3.69	38.98	96.15
81 Tl	L	0.23	2.28	0.16	0.44
85 At	L	0.31	2.18	0.21	0.65

Figure 34: XRF scan results for a gold coated capillary tube

The XRF machine also identified a large amount of Rhodium that is attributed to a background term that was continually identified throughout all material analysis using the XRF. The relative abundance of gold and silver cannot be used in their current form to determine the absolute mass of each in the sample. This is because the sample material is layered and therefore

the X-Ray flux at different layers is not constant due to absorbing and reemission by upper layers. Therefore the determined mass percent cannot be considered an absolute abundance, but does give insight into quantities present. Because the first layer of material is gold, the abundance of gold is an overestimate. The true thickness of silver is approximately 2900 nm and the true thickness of gold is most likely slightly greater than 100 nm as expected. A full scan of the gold coated capillary tube was performed in order to image the uniformity of gold throughout a 3 mm region. Figure 35 demonstrates the results of this scan.

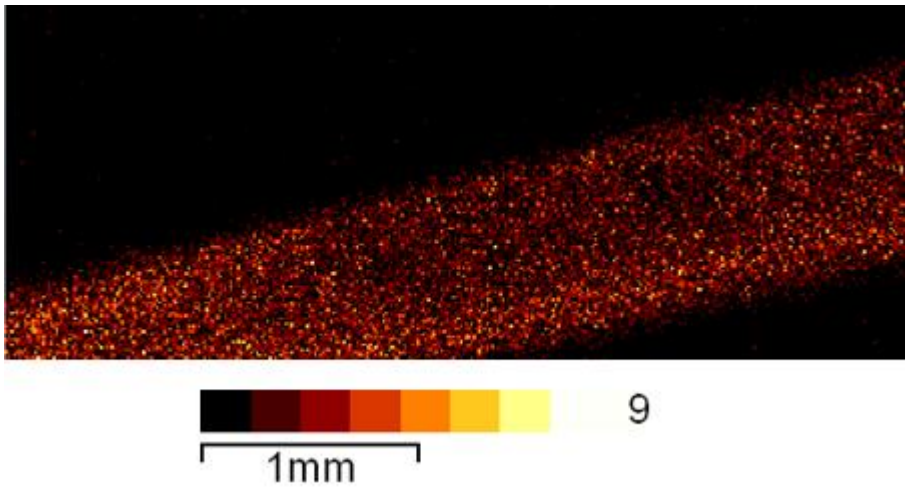

Figure 35: XRF scan for gold along coated capillary tube

Figure 35 affirms that along this 3 mm region the gold capillary tube has a relatively uniform coating and does not appear to have any abnormal edge effects that may have been present due to using a rotator during gold coating.

4.4 SEM Images of Gold Coated Capillary Tubing

Additional microscopic imaging tools, in particular a scanning electron microscope (SEM), were used to further determine coating uniformity as well as identify coating abnormalities and find an approximation to their distributions. An SEM uses high energy electrons to scan the

surface of the material. By analyzing the scattering pattern of a flux of electrons an SEM machine can determine image nanometer sized particles. Figure 36 demonstrates a 25x image of the capillary tube.

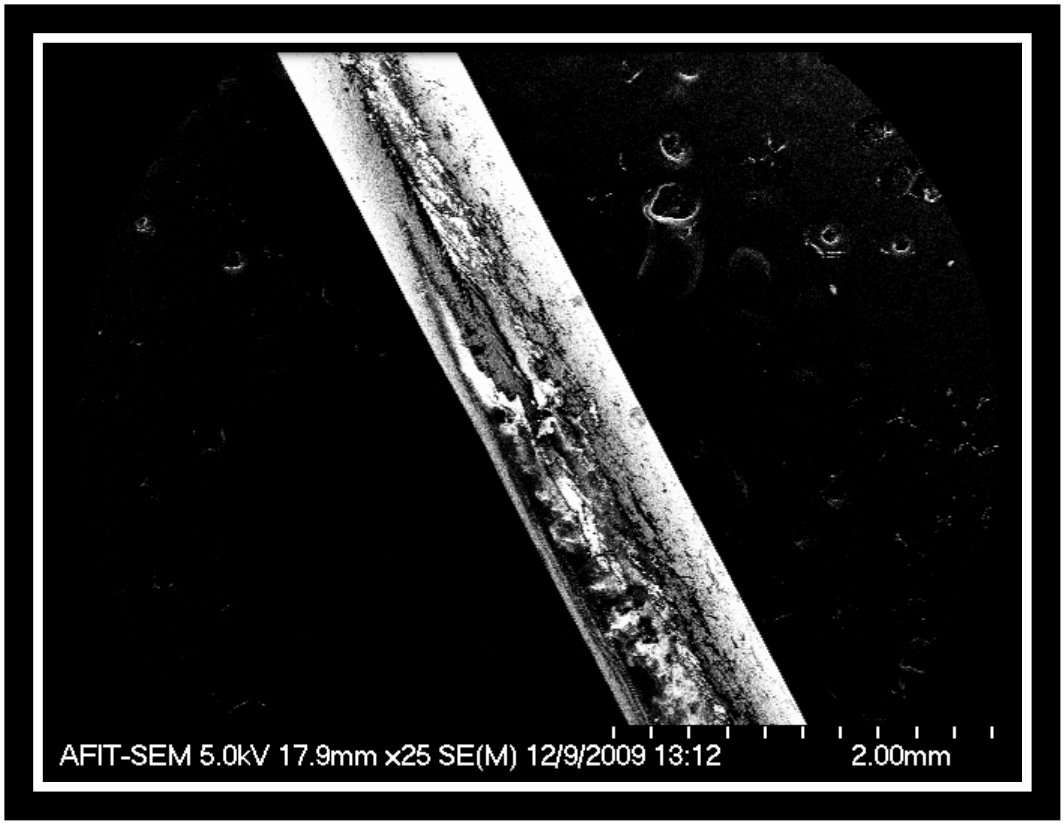

Figure 36: 25x image of a gold coated capillary tube showing large amount of damage done to surface

As shown on Figure 36, the capillary tube has a significant amount of damage present on the surface. It is apparent that the handling procedures are not sufficient enough to isolate the surface from strenuous contact. Further gold coated capillary tubes must be handled differently in order to reduce surface deterioration.

The dark surfaces found in the SEM image correspond to a lack of scattering of electrons, or generally speaking a lack of conducting metal. These dark spots are interpreted as not

sustaining a gold coating, and visually imaging either the acrylate buffer or polyamide bulk of the capillary tube. Figure 37 further demonstrates this interpretation.

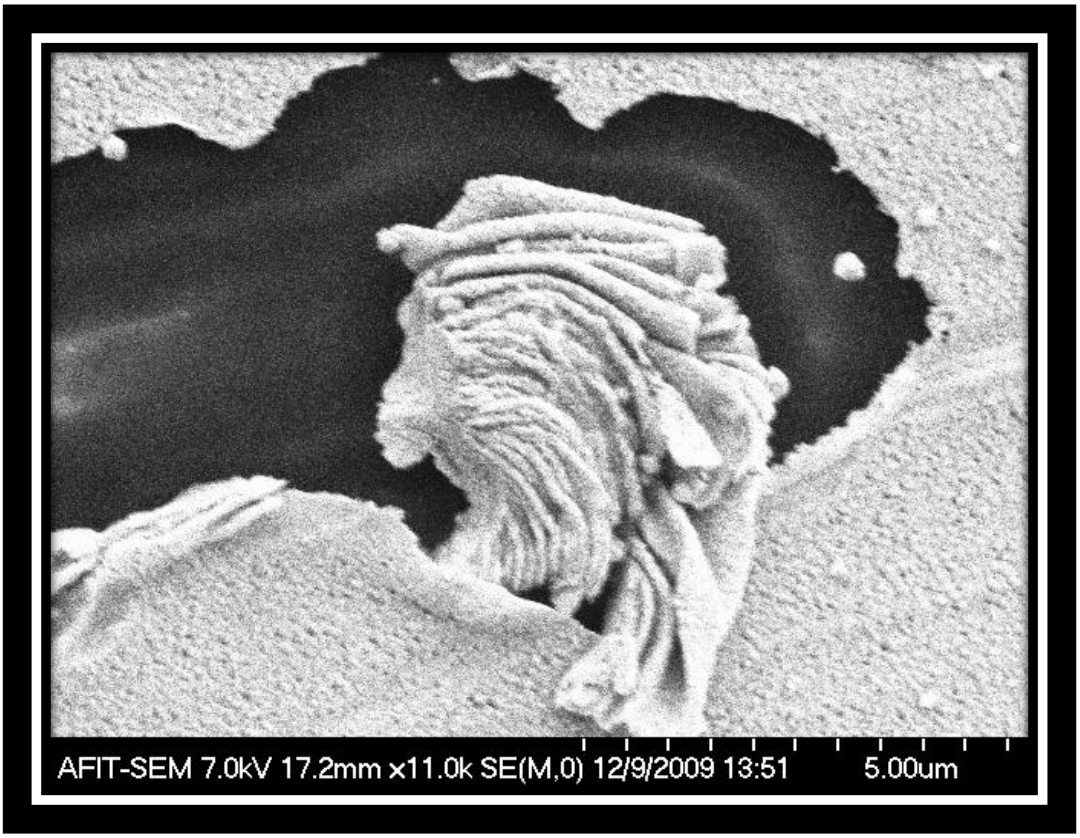

Figure 37: 11,000x image of gold coated capillary tube showing gold scrap and demonstrating dark coloring due to semiconducting material

Figure 37 is a 25,000x 100 μm^2 region in which the upper most layer looks scrapped, still remaining attached to the surface, but bundled up. This scrapped region appears darker (black). However, the adjacent regions are clearly shown with much detail, demonstrating a conductive surface. This conductive surface is the gold coating.

Figure 38 is an additional scan that demonstrates a typical region of interest detailing two obscure objects. These two objects appear to be some form of dust or pre-coating damage.

Both bumps have what appears to be a shadow adjacent to them. This shadow represents an uncoated area, and provides further evidence that the capillary tube handling procedure must be altered in order to minimize these features. The gold coated capillary tube appears to have a concentration of one nano-sized bump every 10 μm^2. This is only true for the retained gold coated regions. The regions where the gold coating was entirely scrapped off could not effectively be imaged using the SEM. The typical dimensions of these bumps, in particular the height, cannot be determined through SEM analysis. Additional imaging techniques in particular using an Atomic Force Microscope (AFM) are required to obtain this information.

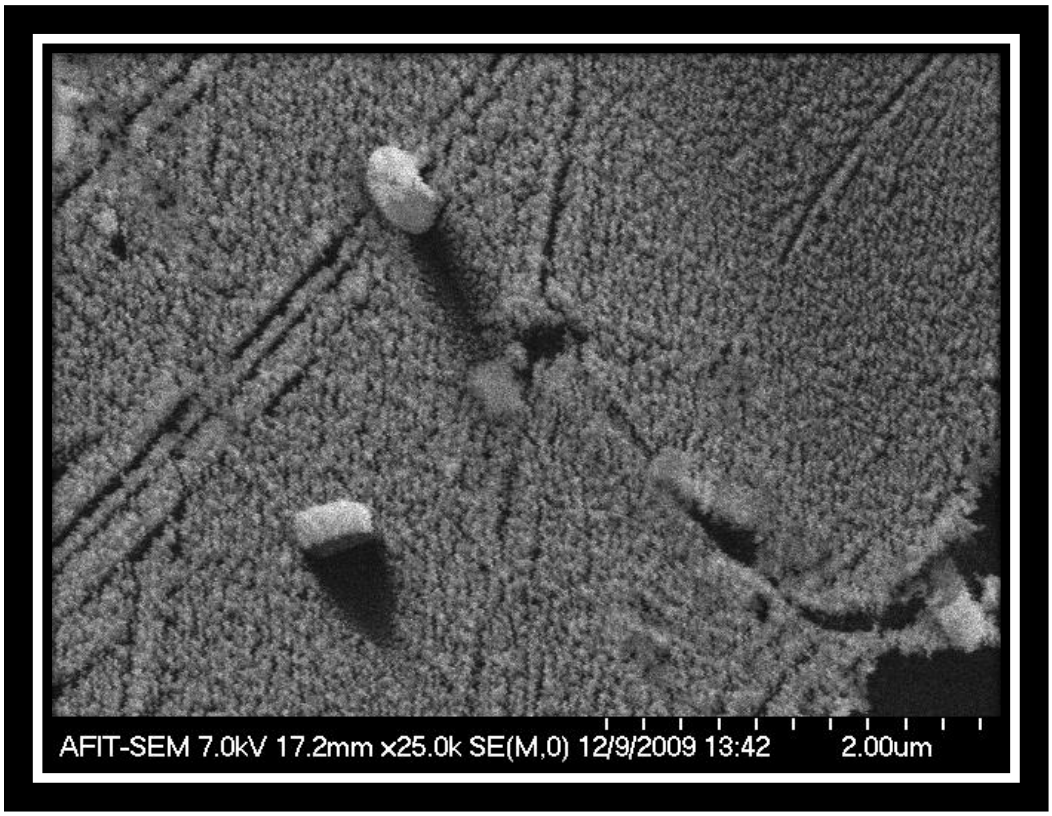

Figure 38: 25,000x image of gold coated capillary tube showing dust particles

Figure 39 is an additional SEM scan obtained at the end of the capillary tube that demonstrates the edge roughness caused through the cutting of the capillary tube as well as using electrical wire along the inside of the tube during gold deposition. At 130x the inside of the capillary tube, although damaged, still appears to sustain a silver lining. This lining is apparent due to the brightness of the inside material. Although rough, these edge effects should not pose any risk to the desired future field effects. Using electrical wire to suspend the capillary tube is an acceptable method for deposition as well as possible handling procedures.

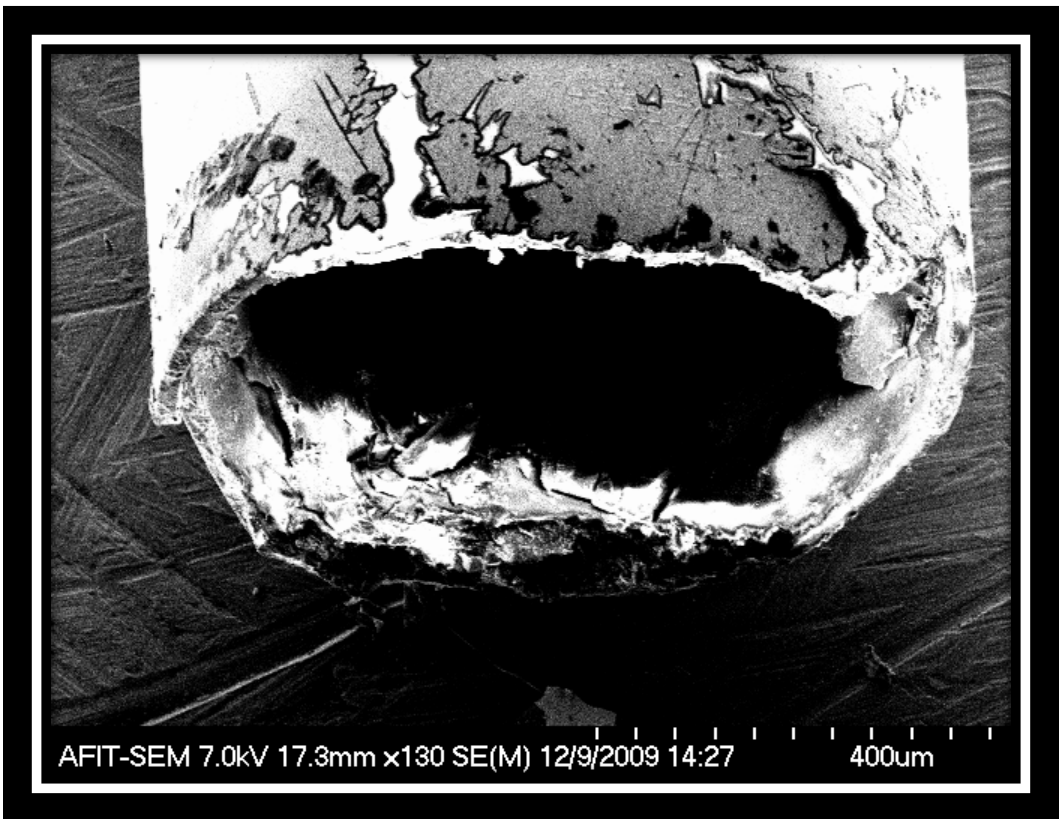

Figure 39: 130x image of gold coated capillary tube showing large amounts of damage, but still retaining inner silver coating

4.5 AFM Images of Gold Coated Capillary Tubing

Atomic Force Microscope (AFM) was used in order to better determine the smoothness of the gold coating on the capillary tube. An AFM uses a cantilever with a sharp tip at one end. By precisely scanning the surface, always maintaining a constant force between the surface and the cantilever, an AFM can provide quantitative information on roughness.

A diamond cantilever tip was used for imaging the gold capillary tube. The diameter of the tip was roughly 100 nm wide. Many surface scans were performed. Several interesting features were observed and further investigated. Figure 40 is a 3 - Dimensional AFM image of a 5x5 μm^2 region of interest.

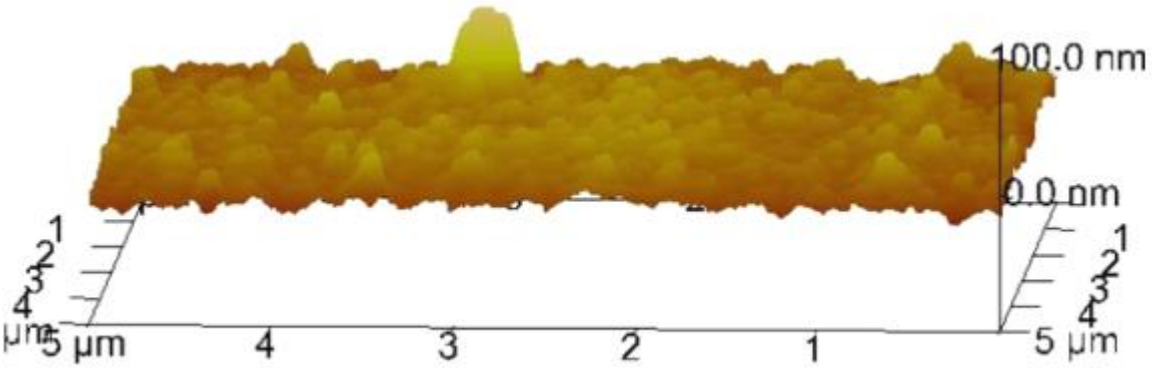

Figure 40: AFM image of 25 μm^2 area of gold coated capillary tube

A distinct 40 nm sized bump located near the back end of Figure 40 is observed. This bump is characteristic of that imaged previously in several SEM images, in particular Figure 38.

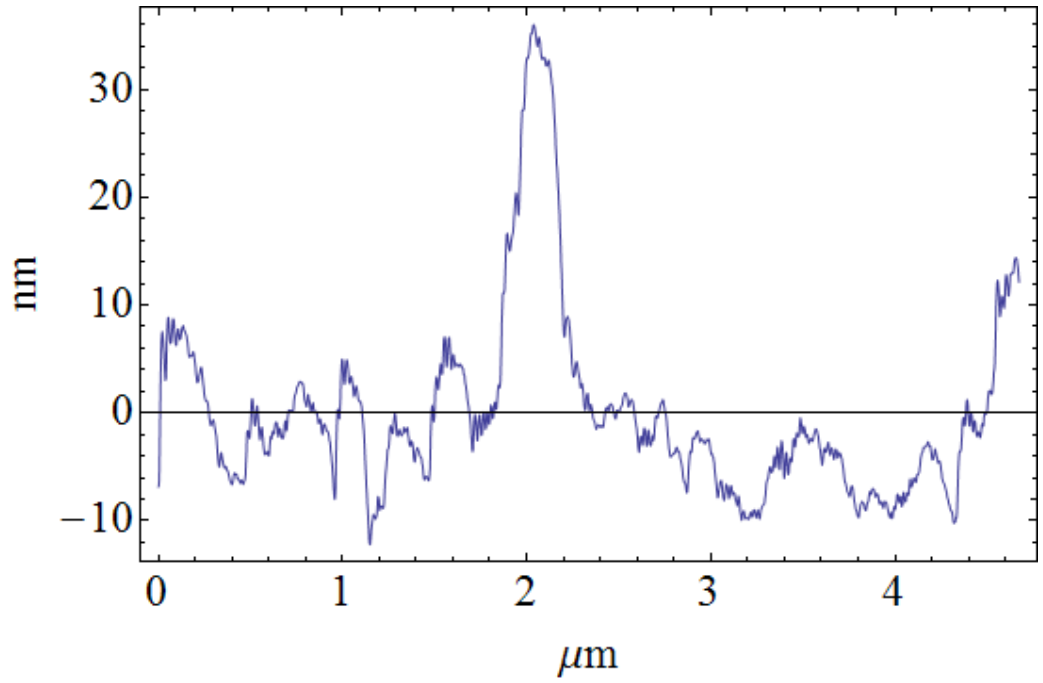

Figure 41: Plot highlighting size of large bump imaged using AFM, large bump feature providing quantitative height of highlighted bump found in Figure 40

Figure 41 is a 2-D scan along a region found within Figure 40. Figure 41 shows the presence of a significant 40 nm tall with a 500 nm base feature. This type of feature is once again found commonly among scans. These types of features may be detrimental to future experimentation, mainly because they are not intended to be present and may not be able to be controlled. Future gold coated capillary tubes will be coated with silver nanoparticles. The intent of these nanoparticles are to create peaks on the surface similar to the bump feature imaged by Figure 40, but with much smaller diameter (10-50 nm). These particles are also intended to be regulated both in size and distribution. Reducing these seemingly uncontrolled, unidentified bumps is essential in order to maximize the effectiveness of any silver nanoparticle array in creating potential local high electric fields.

Additional analysis of the regions not exposed to these bumps appears very promising. Figure 42 shows how over a 2000 nm region that the change in surface roughness does not

exceed 20 nm over this region The AFM images gathered indicate that handling procedures are required to change in order to provide the full surface effects desired. These images also highlight that using the E-beam evaporative method for surface coating appears acceptable in creating the smoothness necessary to deposit silver nanoparticles and make a difference in surface extrusion. Silver nanoparticles of 10-50 nm size should extrude this highlighted surface, and potentially create the desired field effects.

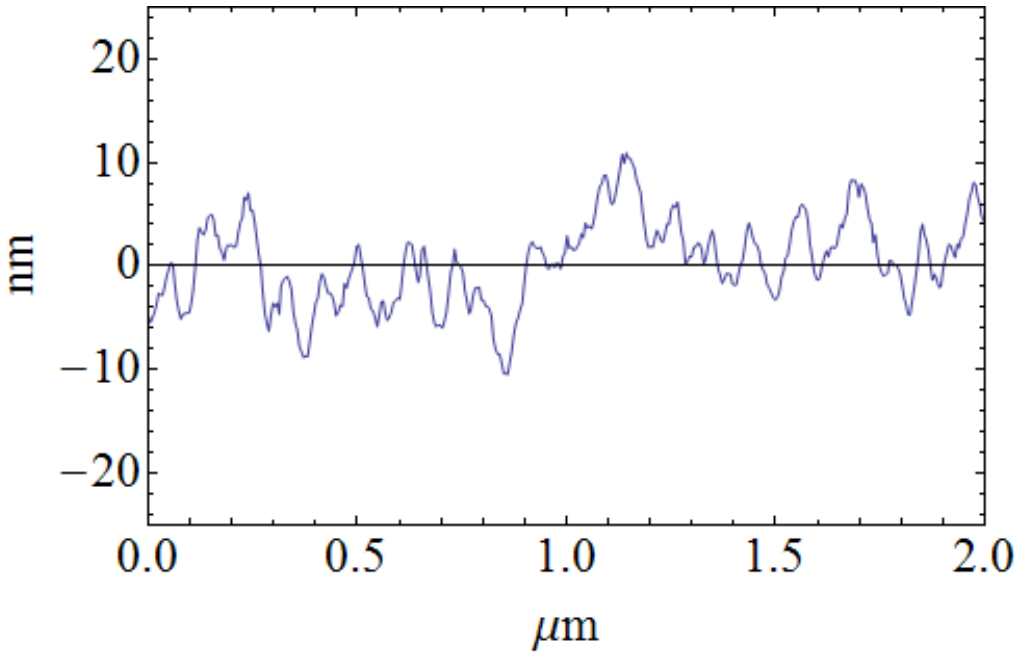

Figure 42: Plot of AFM image highlighting a 2000 nm "smooth" surface

4.6 Silver Nanoparticle Colloid

Silver nanoparticle concentrations can be constructed by mixing silver nitrate with variety of reducing agents. Previous research has indicated that the following chemical reaction can produce silver nanoparticles.

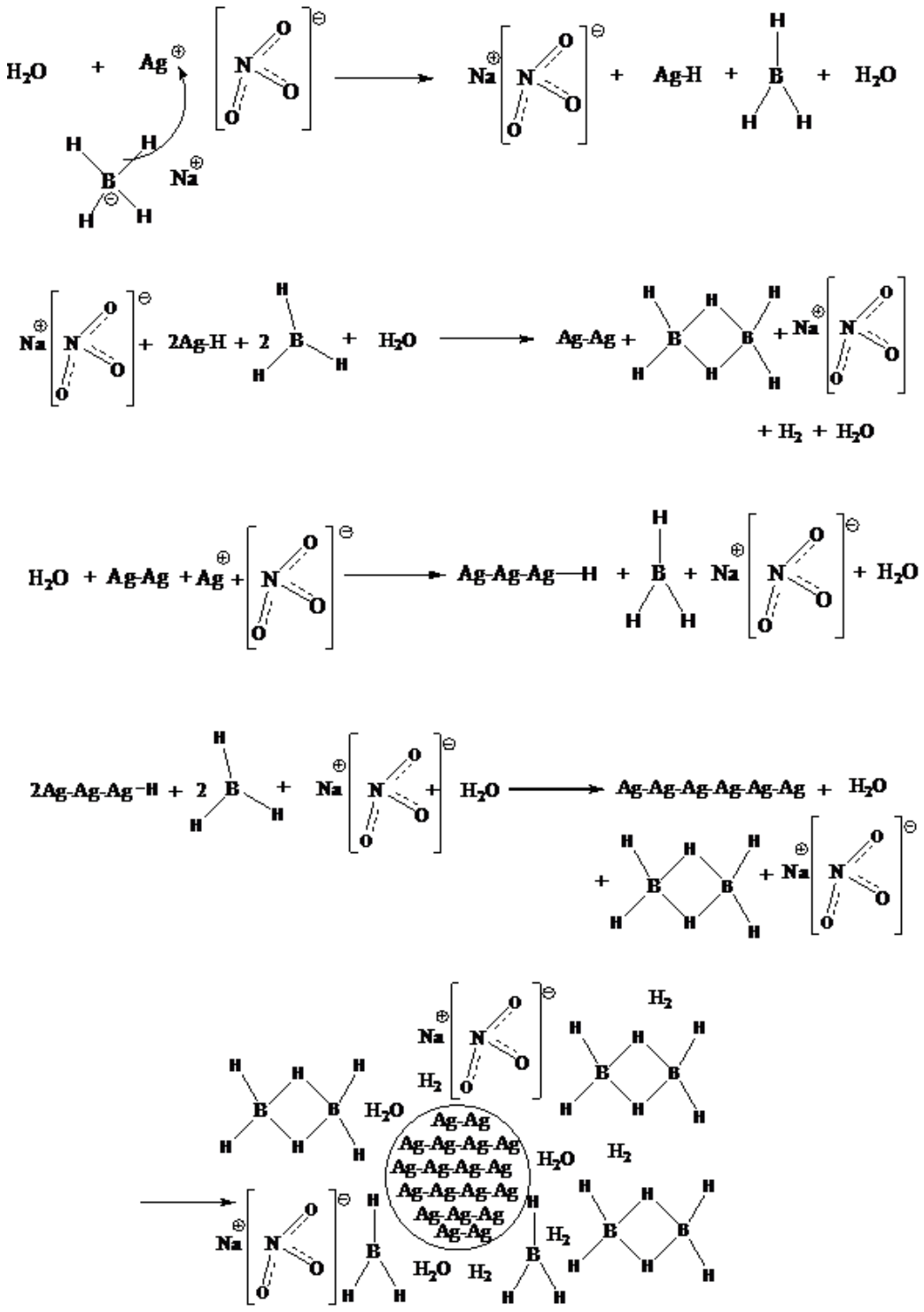

Figure 43: Chemical reaction highlighting silver nanoparticle formation [48]

Silver nitrate mixed with sodium borohydride can produce aggregates of silver nanoparticles [49]. The sodium borohydride first donates a hydride to a Ag ion in order to generate silver hydride. Two silver hydride molecules and two borane molecules dimerize to generate neutral metallic silver (Ag_2), diborane and H_2 gas. The metallic silver can then complex with the Ag ion to form metallic silver. This metal is then reduced again by $NaBH_4$ and the cycle is repeated until a nanoparticle is stabilized by boranes and diboranes. If the temperature is not kept cool, a hydrolysis (side reaction) will occur in which $NaBH_4$ is converted to $NaB(OH)_4$. This is illustrated by Equation (46). In order to slow the rate of this reaction, synthesis should be carried out at ice cold temperatures.

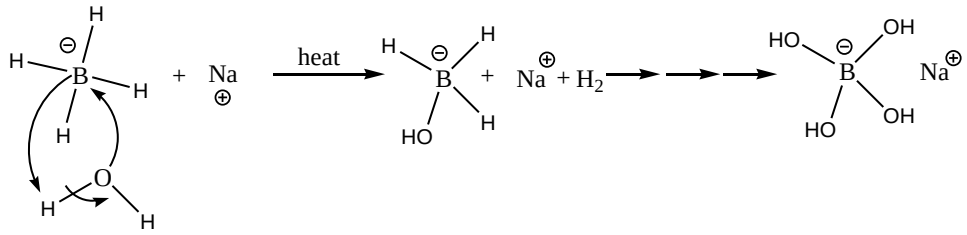

(46)

Following a 20 minute mixing time, this synthetic method produces a yellow tinted colloid. Ultraviolet-visual (UV-vis) spectroscopy can be performed on a sample in order to verify particle size. Previous research has demonstrated that UV-vis spectrum centered upon 400 nm corresponds well to a distribution of silver nanoparticles on the order of 12 ± 3.4 nm in size. Figure 44 demonstrates the results of the UV-vis measurement and Transmission Electron Microscope (TEM) measurements [49] of a 2:1 mixture of sodium borohydride and silver nitrate.

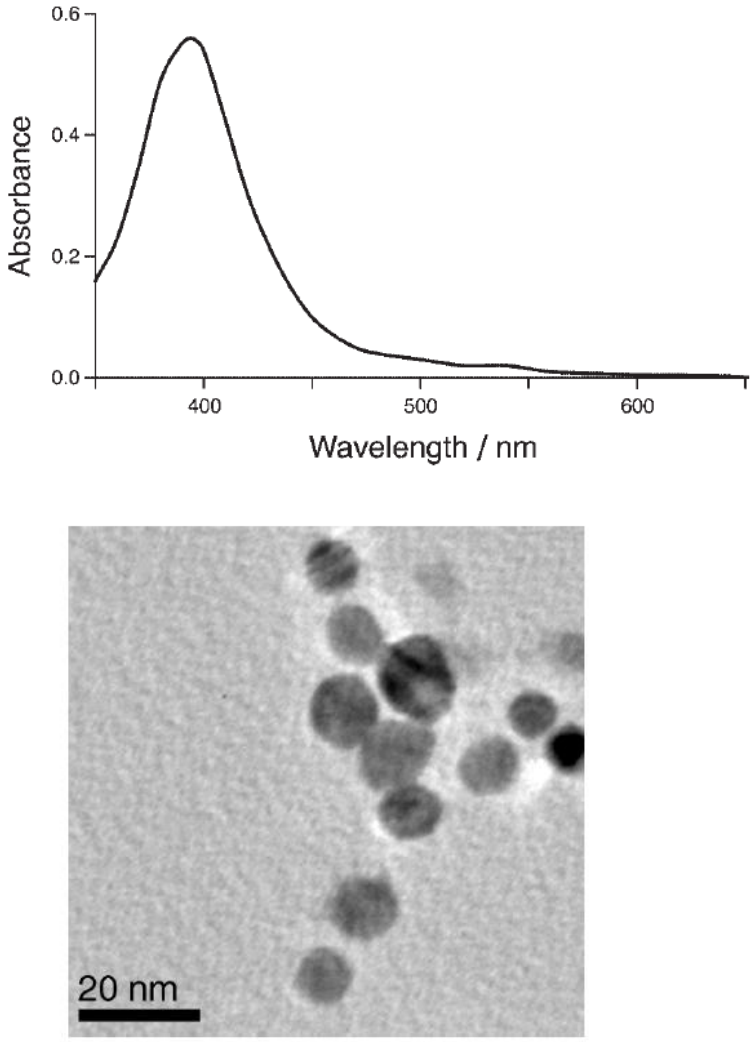

Figure 44: UV-vis Spectrum of silver nanoparticles using Sodium borohydride and highlighting correlatied size distribution obtained through a TEM image [49]

Additional silver nanoparticle synthesis using sodium citrate can be used in order to produce larger silver nanoparticle aggregates on the order of 50 nm in size. The UV-vis spectrum from these aggregates shifts due to the larger particle size. Figure 45 demonstrates this result [50]. For silver nanoparticle synthesis, the UV-vis spectrum can be used for these known mixtures as a gauge to aggregate size.

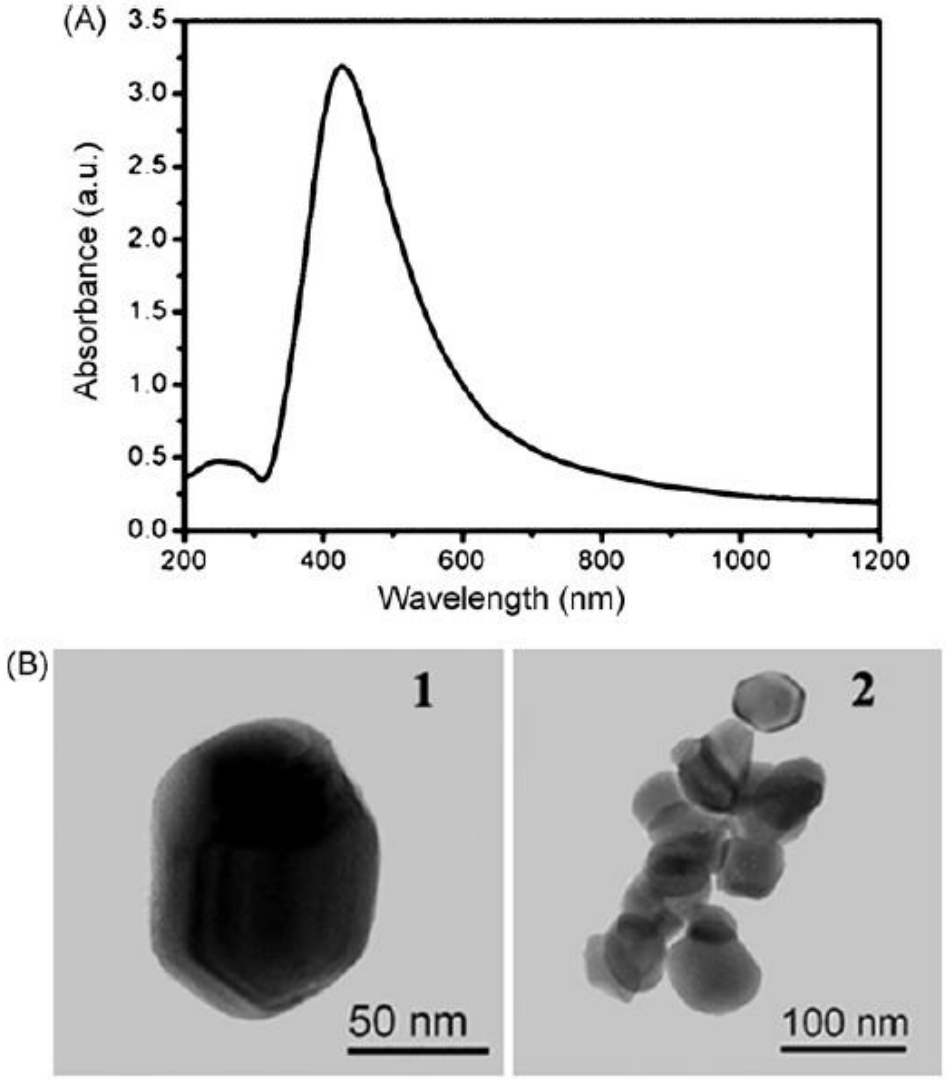

Figure 45: UV-vis Spectrum of silver nanoparticles using sodium citrate and highlighting correlated size distribution obtained through a TEM image [50]

Using either of these two methods, a UV-vis spectrum can provide insight as to the size distribution of silver nanoparticles based upon the location of the peak absorption wavelength. In order to maximize enhanced local electric fields, as long as surface features do not exceed particle size, a dense array of the smaller sized silver nanoparticles would be ideal.

Silver nanoparticles were constructed mixing 1.7 mg of $NaBH_4$ with 4.53m g of $AgNO_3$ in 70 mL of distilled water [51]. Calculations indicate that this colloid should have a density of

15.42 ppm of silver nanoparticles. A barometer was used to mix $AgNO_3$ and $NaBH_4$ at a rate of one drop per second. The resultant concentrate was then stirred in a magnetic stir plate for 20 minutes. As expected, following mix time, the silver nanoparticle colloid had a yellowish tint. The resultant colloid was then analyzed through a UV-vis spectrometer to provide insight into the size distribution of silver nanoparticles as demonstrated by Figure 46. These particles were also imaged with a TEM to verify particle size distribution as demonstrated by Figure 47 [48]. Although a distribution of sizes exist, the average size is approximately 10 nm. As Figure 46 and Figure 47 demonstrate the colloid mixture is near identical to that of the intended standard illustrated in Figure 44.

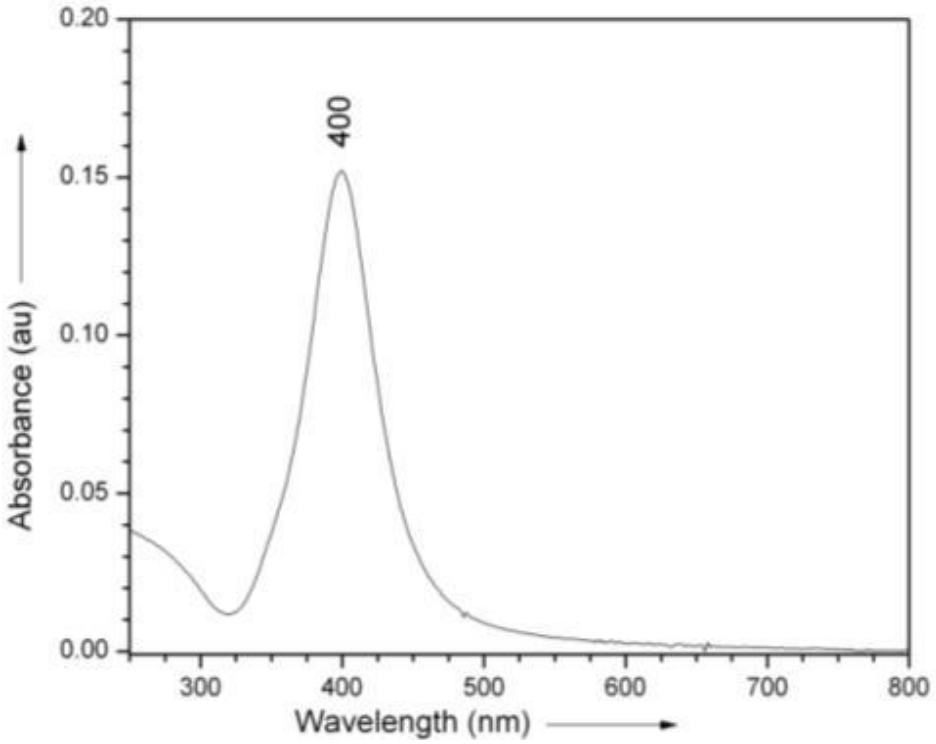

Figure 46: UV-vis of silver nanoparticle colloid to be deposited on surface of gold coated capillary tube

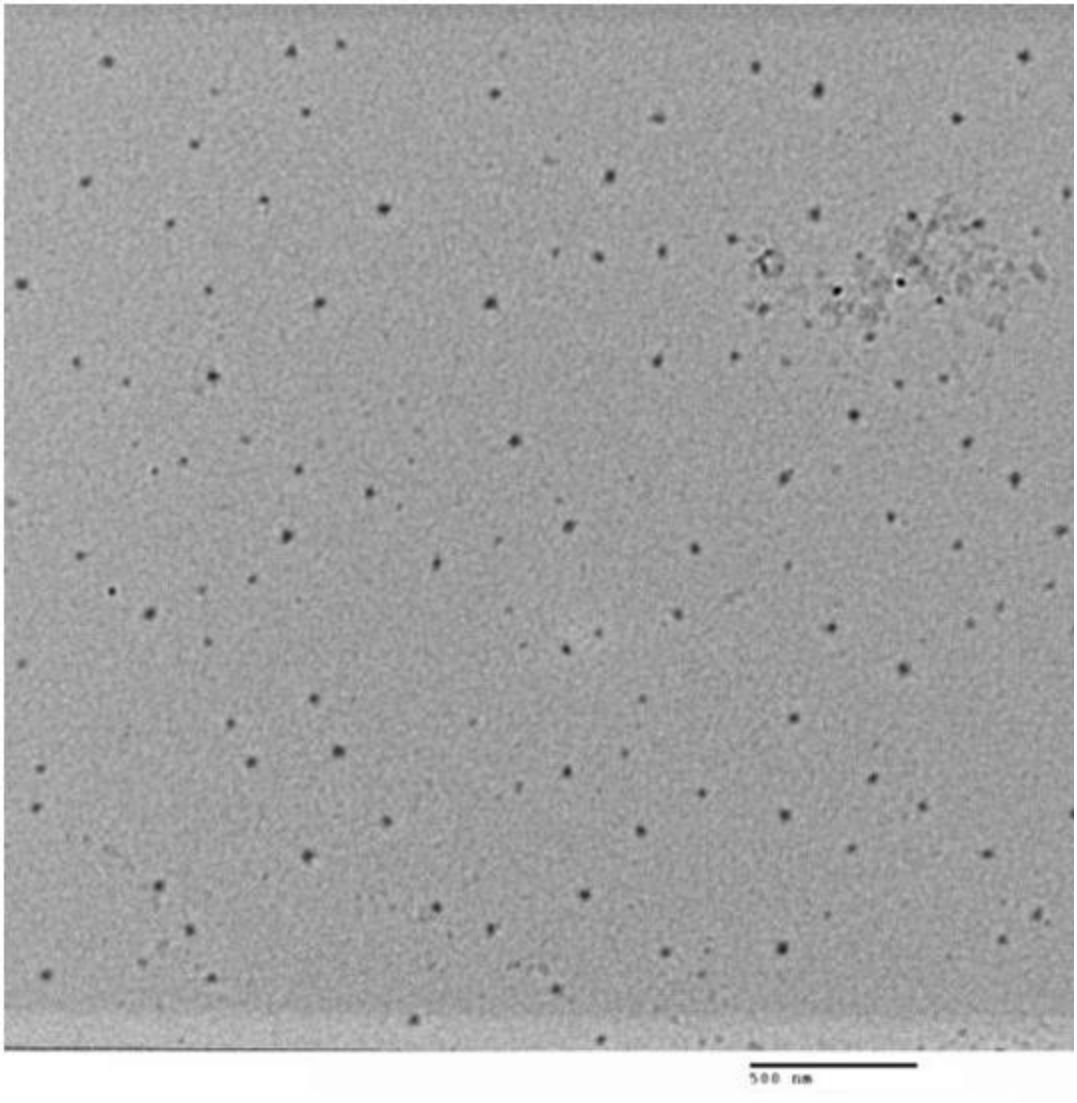

Figure 47: TEM image of silver nanoparticles to be deposited on gold coated capillary tube [48]

Additionally, a Varian fast sequential atomic absorption spectrometer (model AA240) equipped with an air-acetylene burner and a silver hollow cathode lamp was used to determine the silver nanoparticle content within the colloid sample by investigating the atomic absorption of a flux of 328.1 nm photons. Five samples of known silver concentration were used to develop the calibration standard. Each sample was measured three times, with the final absorbance value set to the average measured value. The results from measured samples including calibration

curve are demonstrated by Figure 48. This best fit curve was then extrapolated to determine the concentration of silver within the colloid. The extrapolated curve indicates a density of 15.31 ± 0.05 ppm of silver nanoparticles. This agrees well with the theoretically calculated value of 15.42 ppm.

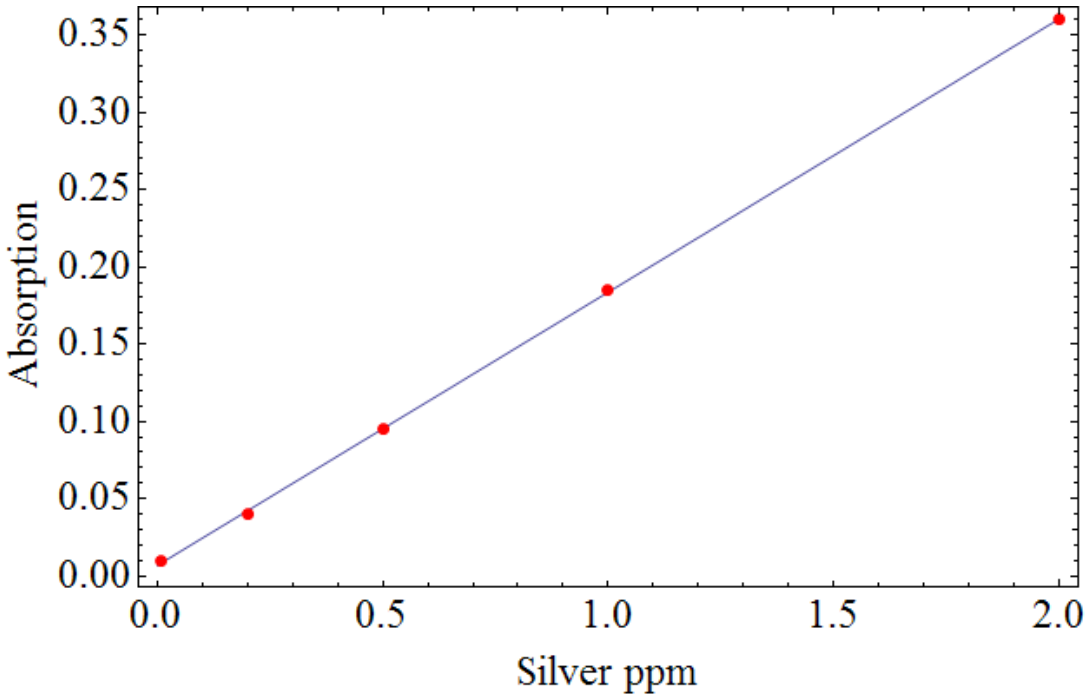

Figure 48: Silver atomic absorption curve fit to know standards (ppm)

4.7 Silver Nanoparticle and Linker Construction

In order to form a reliable attachment between the silver nanoparticles and the gold capillary tubing, a combination of chemicals that have varying affinities towards gold and silver were applied to set up periodic linker combinations along the surface. These linkers will have one end (end of molecular chain) attached to capillary tube (Au) and the other end free to attach to silver nanoparticles. The interaction of positron species with these linkers must also be minimized. In order to minimize these interactions a combination of p-Phenylenediamine (PPD) and

n-Heptylamine, short molecular structures, were chosen. PPD is a homobifunctional linker that can be used to attach to the gold surface of the capillary tube. Once attached to the gold surface, PPD linkers are also known to have a high affinity towards silver nanoparticles [52], these linkers are referred to as active. Once attached to the gold surface, n-Heptylamine will not commonly attach to silver nanoparticles. These linkers are referred to as inactive. This process is further illustrated by Figure 49. The PPD molecule contains a H_2N strand at both ends, generally undergoing a chemical reaction and bonding to either silver or gold particles when present. The n-Heptylamine contains only one H_2N strand, theoretically allowing one end to undergo a chemical reaction and bind to the gold surface. The other end is not reactive to silver nanoparticles.

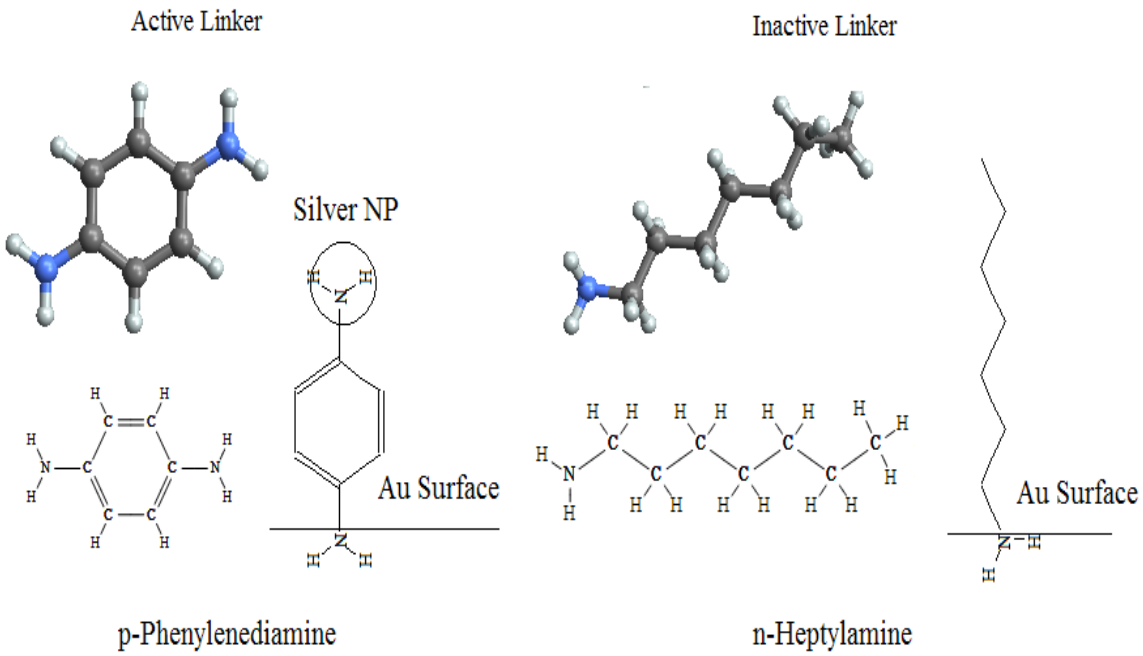

Figure 49: Illustration of active (p-Phenylenediamine) and inactive (n-Heptylamine) linker molecules.

By testing varying concentration ratios of active to inactive solutions, silver nanoparticle arrays were constructed with the intent of determining processes that produce varying array distributions both in nanoparticle size and in separation. The spatial separation will be determined using a SEM. AFM images were used to determine surface peaks.

Additional capillary tubes were coated with a 150 nm layer of gold using the Torr E-beam evaporation machine. Following deposition, handling procedures were altered. Each capillary tube was horizontally suspending within an isolated container using 20 gauge electrical wire. Segments 2 cm in length were cut in order to mix with linker and silver nanoparticle solutions.

Using 99% p-Phenylenediamine (PPD) a stock 0.1 M concentrate solution of PPD was mixed using water as the solvent. In 50 mL of water, concentration ratios of 1:10, 1:50, 1:100, 1:500, and 1:1000 of PPD:n-Heptylamine were mixed in solution. Table VII outlines the concentration ratios, volume of PPD and n-Heptylamine, and the total mixing times for the capillary tube in both linker and silver nanoparticle (NP) solutions used for gold coated capillary samples.

Table VII: Linker molecule PPD and n-Heptylamine relative concentrations and mixing times

Molar Ratio	PPD 0.1 M Stock (µL)	n-Heptylamine 6.72 M Stock (µL)	Mixing Times Linker (hours)	Mixing Times Silver NPs (hours)
1:10	500	74.4	24	12
1:50	100	74.4	24	3
1:100	50	74.4	24	12
1:500	10	74.4	24	3
1:1000	5	74.4	24	12
NA	10	0	24	3
NA	100	0	24	3

Two additional solutions of PPD were mixed with water without any n-Heptylamine added. Each solution was placed in a beaker with the 2 cm gold capillary tube placed gently inside. An additional solution consisting of 50 mL of water was also used to serve as a control sample. As shown in Figure 50 a Fisher Scientific rotator was used and set to a low speed during entire mixing time.

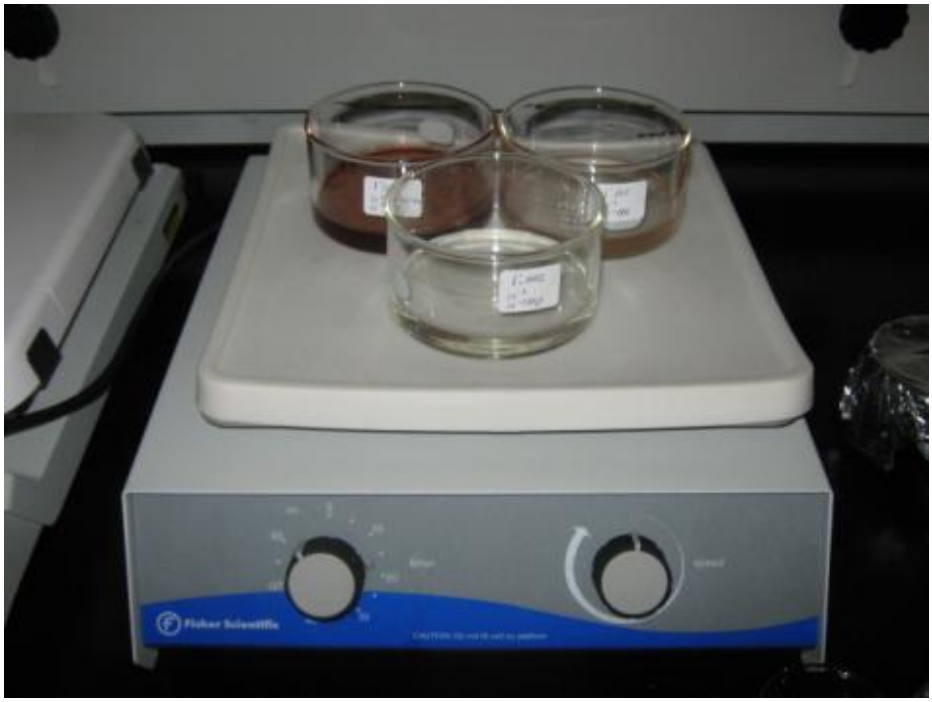

Figure 50: Rotator used to mix gold coated capillary tube and linkers and eventually silver nanoparticles. Of importance is color of high concentration of PPD solution (top left)

The capillary tube sample within the linker solution containing the 1:10 Molar ratio of PPD:n-Heptylamine had underwent a distinct color change, and appeared to be entirely void of any gold. This solution concentration appears to high for the duration of linker mixing time of 24 hours. This tube sample was not imaged using either the SEM or AFM.

Following mixing times of the capillary tube with linker solutions, the capillary tubes were gently removed and placed in 10 mL of silver nanoparticle solution made six days prior following

the $AgNO_3$ and $NaBH_4$ mixing formula. At the conclusion of the silver nanoparticle mixing stage, each 2 cm capillary tube sample was individually held suspended within the storage container using 20 gauge electrical wire.

4.7.1 SEM Imaging of Silver Nanoparticles

Numerous SEM images were taken of all silver nanoparticle deposited samples on capillary tubing with linker mixing concentrations and times outlined by Table VII. Two additional control samples were imaged. One of the controls was not mixed with any silver nanoparticles and is referred to as Control I. The other control was mixed for 24 hours with water, no linker molecules, and then added with silver nanoparticle solutions, referred to as Control II.

Figure 51 details a 25x image of one of the sample capillary tubes. There is minimal amount of surface damage relative to previous control samples, in particular Figure 36. This drastic reduction of damage is attributed to the adjustment in handling procedures, in particular the horizontal suspension by 20 gauge electrical wire. There does however appear to be some non-uniformities (damage) to the gold surface. This is clearly demonstrated by Figure 52, which is a 3000x and 10,000x image of Control I.

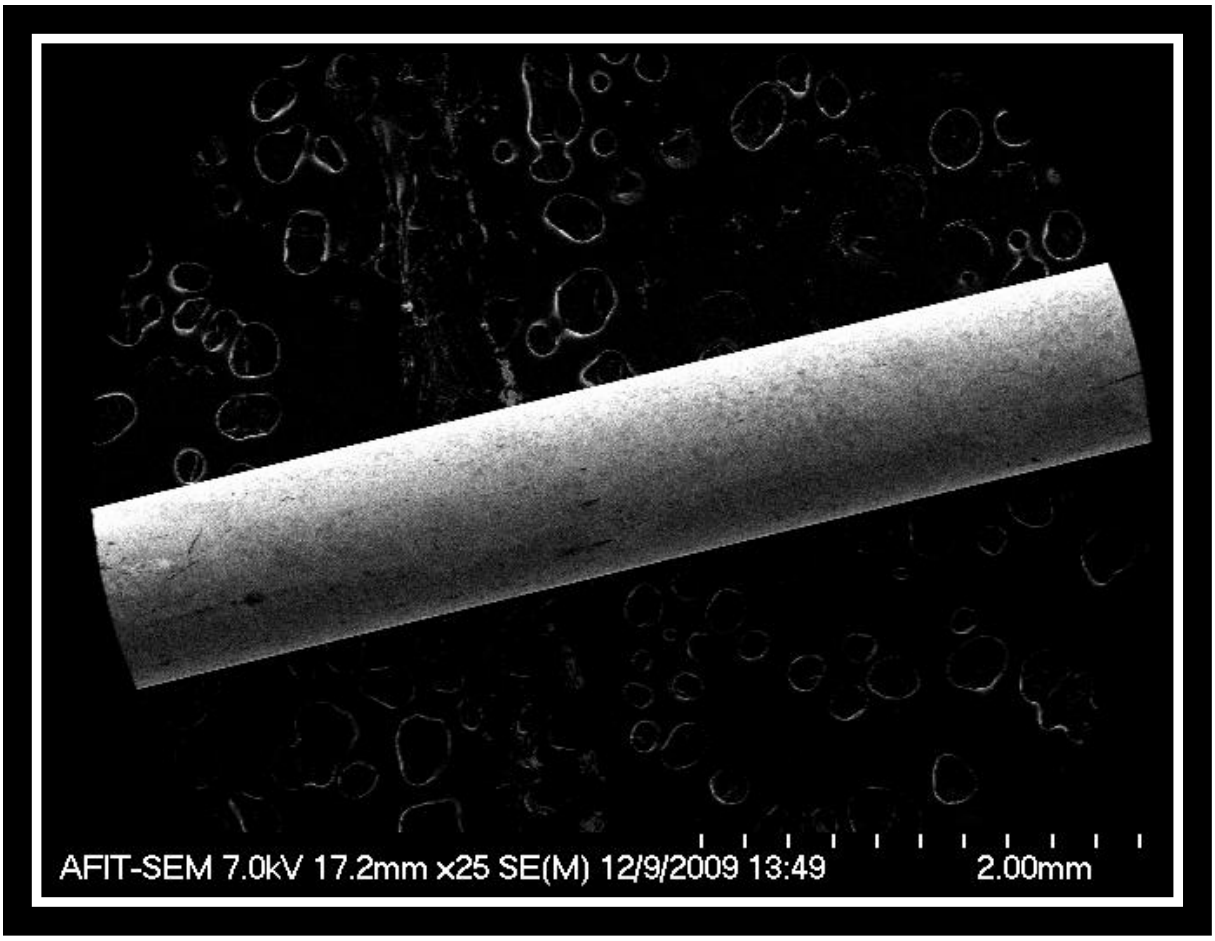

Figure 51: 25x image of gold coated capillary tube illustrating improvements in handling procedures relative to previously imaged SEM samples

Figure 52 a 3,000x and 10,000x image of the Control I surface, shows slight scratch marks as well as a dark spot in the top left corner of the top image. The lower 10,000x image appears to be have relatively smooth area. This is demonstrated further by Figure 53, a 30,000x image of the same surface. This smoothness is once again attributed to a thorough methanol cleansing prior to gold evaporation as well as improved handling procedures. As expected no large distinguishable extrusions appear on Control I. Differences in surface characteristics of other samples will be analyzed with respect to these control images, which are assumed to have only gold and defects on the surface.

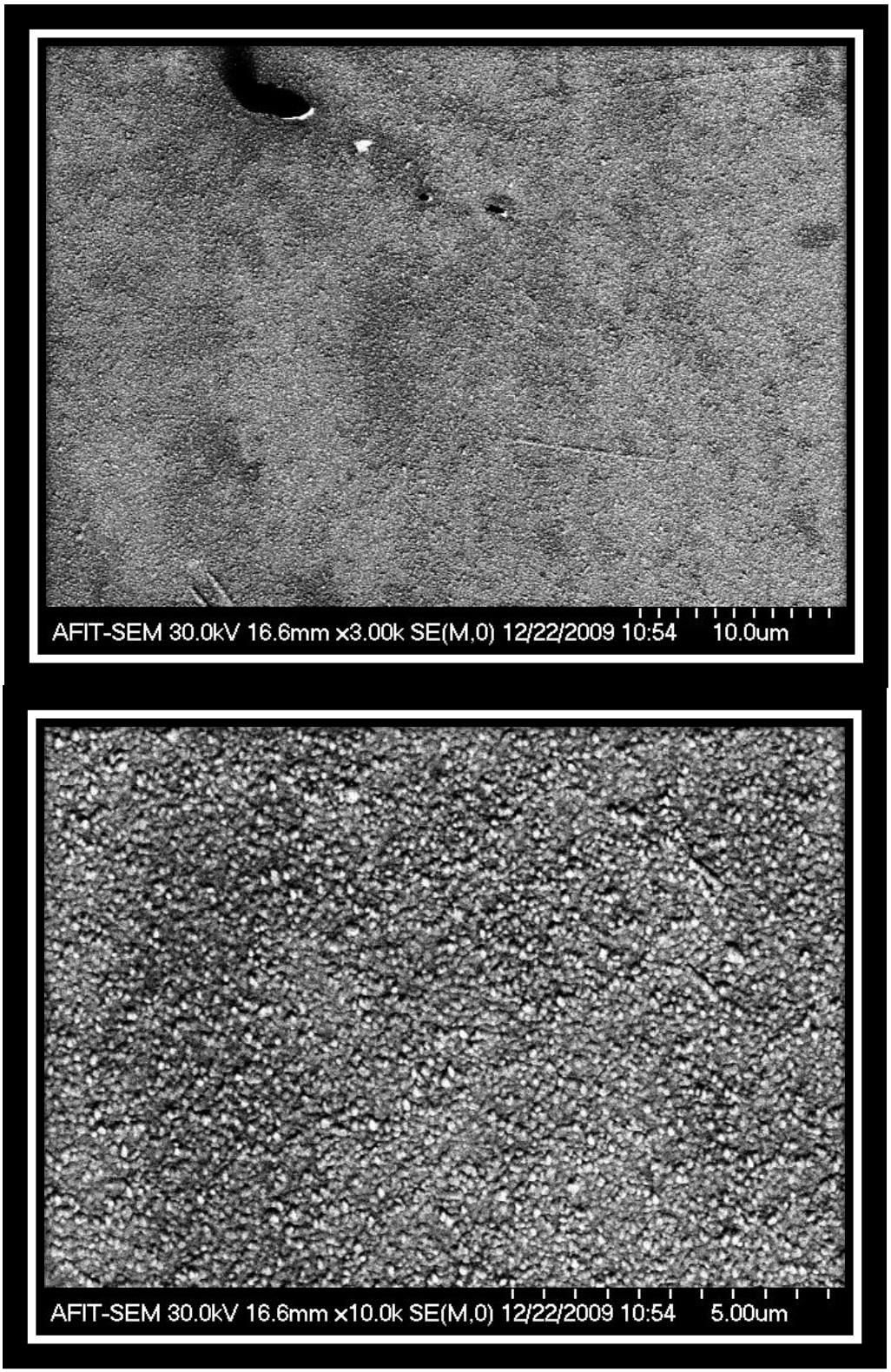

Figure 52: SEM images of gold coated capillary tube, Control I no treatment

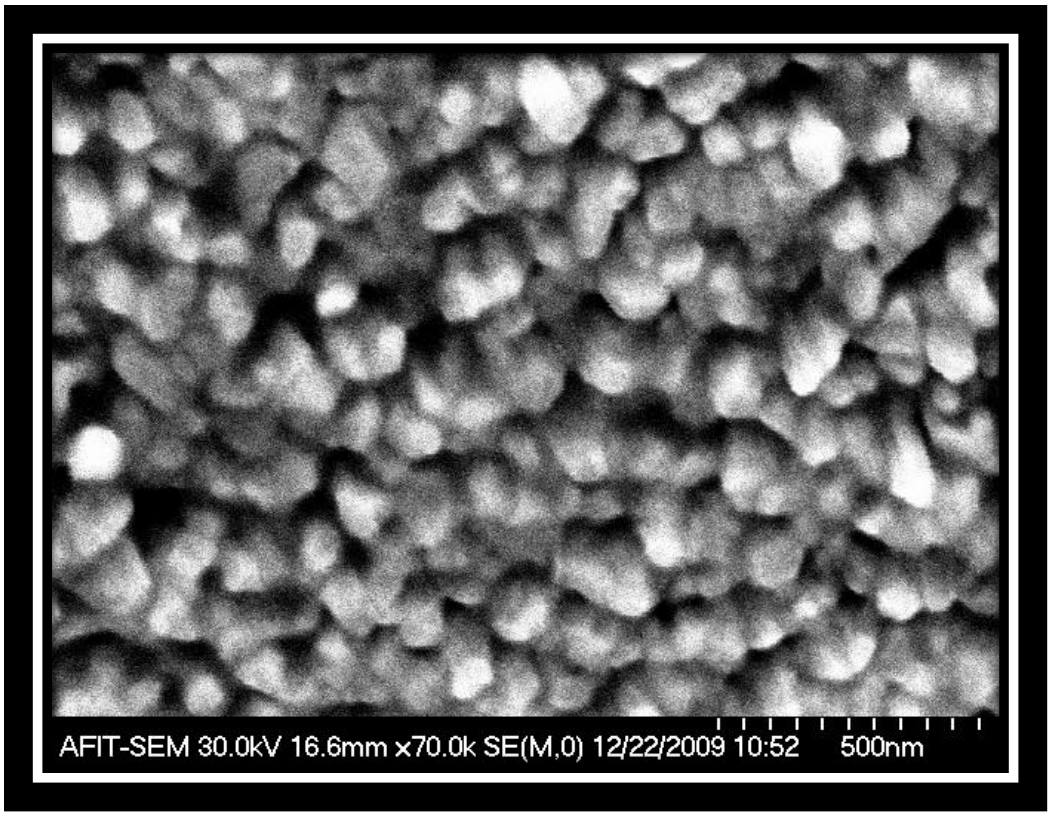

Figure 53: 30,000x image of gold coated capillary tube highlighting generally smoothness of surface

Figure 54 is a 2000x image and a 35000x of Control II. Control II was treated with silver nanoparticles, but did not have the linkers that are assumed to be necessary for a large amount of silver nanoparticle bonding to the gold capillary surface. All extruding objects located in Figure 54 appear with dark regions adjoined, characteristic of a defect and not actual nanoparticle formation. The image of Figure 54 further highlights the lack of extruded objects without evidence of surface tamper. One large surface feature (top left) has an apparent dark shadow characteristic of surface damage.

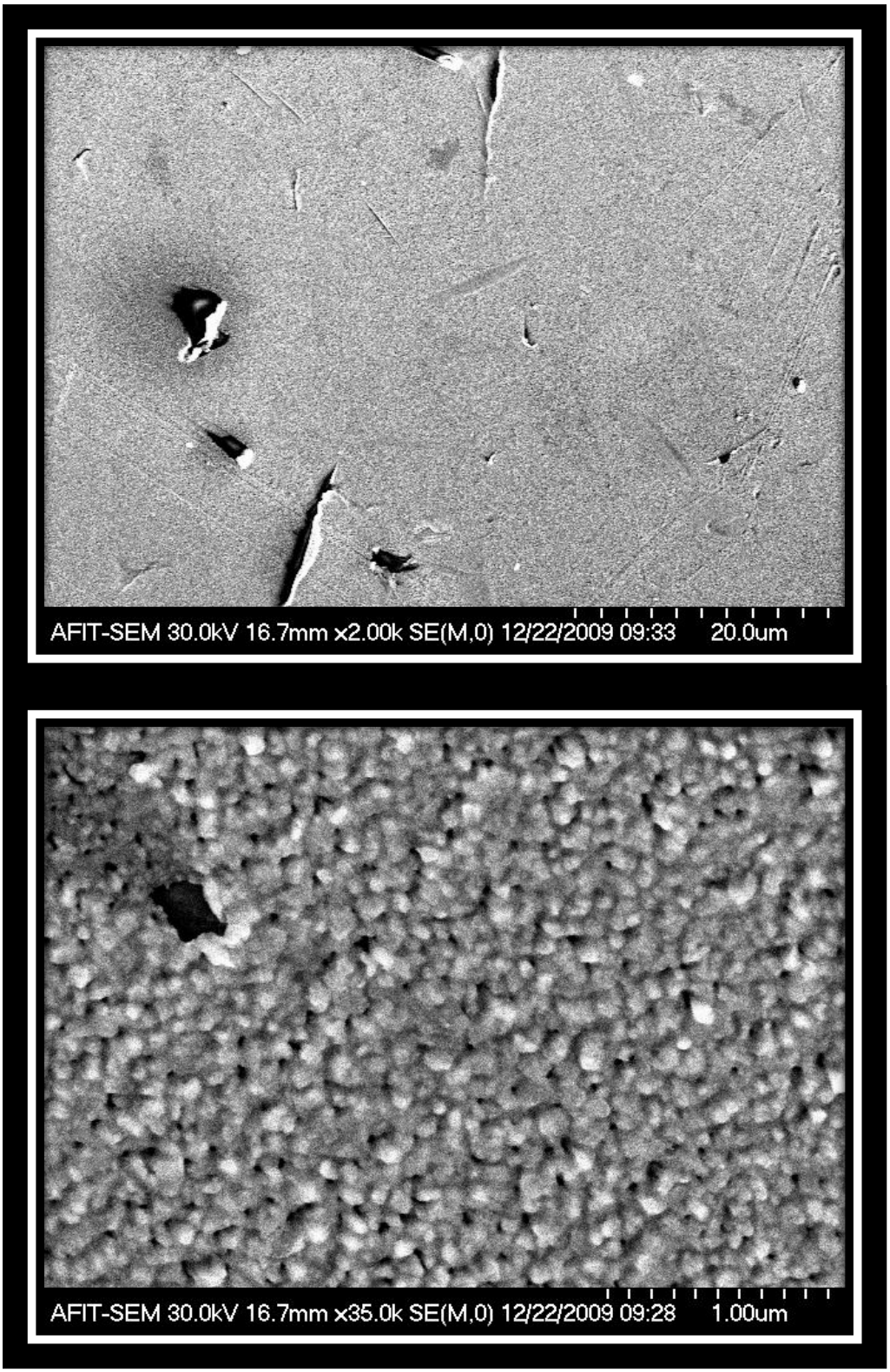

Figure 54: SEM images of gold coated capillary, Control II water treatment

Figure 55 is a 6000x and 30,000x image of the 1:1000 PPD : n-Heptylamine sample capillary tube treated with silver nanoparticles. The top image details slight scratches found on the surface. This image also highlights the lack of 10-100 nm sized nanoparticle objects. The bottom image highlights one of the few of these objects found in the 1:1000 ratio sample. This object however, is accompanied once again by a black shadow. This shadow signifies that this is most likely not a silver nanoparticle, but a conglomerate of a gold scratch or dust covered in gold during deposition.

Figure 56 are 2000x and 8000x images of samples mixed with concentration ratios of 1:500 and treated with silver nanoparticles. Of key importance in this image is the sole approximately 250 nm sized particle isolated from any "shadows". This object is identified as most likely being a silver nanoparticle, due to size, geometry, and the change in brightness relative to the surface. A contrast in brightness for a SEM image can be present for different materials. However, this 250 nm sized particle is not characteristic of the silver nanoparticle sizes expected to be deposited. The distribution of these particles is also sparse and therefore not ideal.

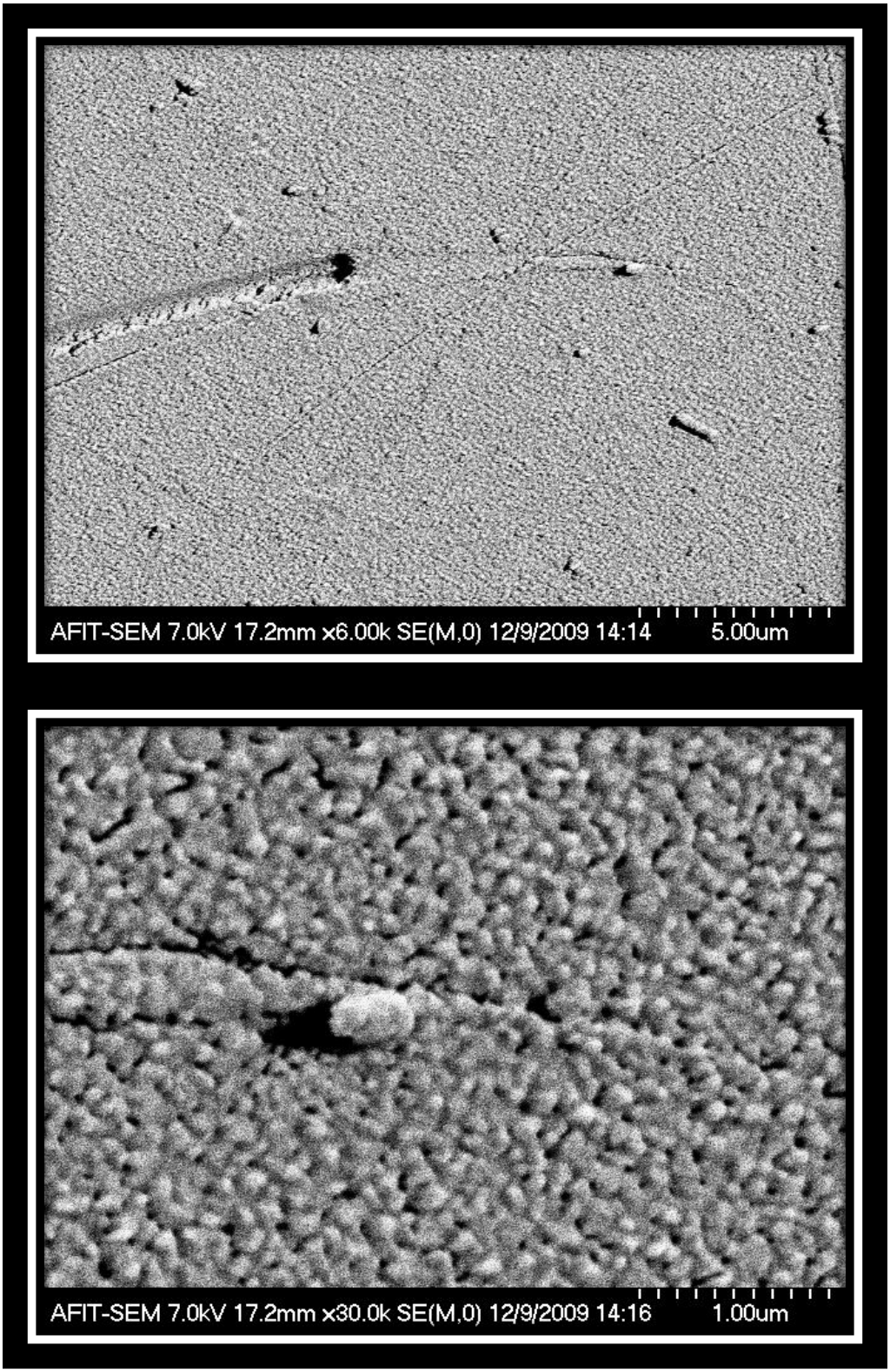

Figure 55: SEM image of silver nanoparticle treated tube with 1:1000 linker ratio

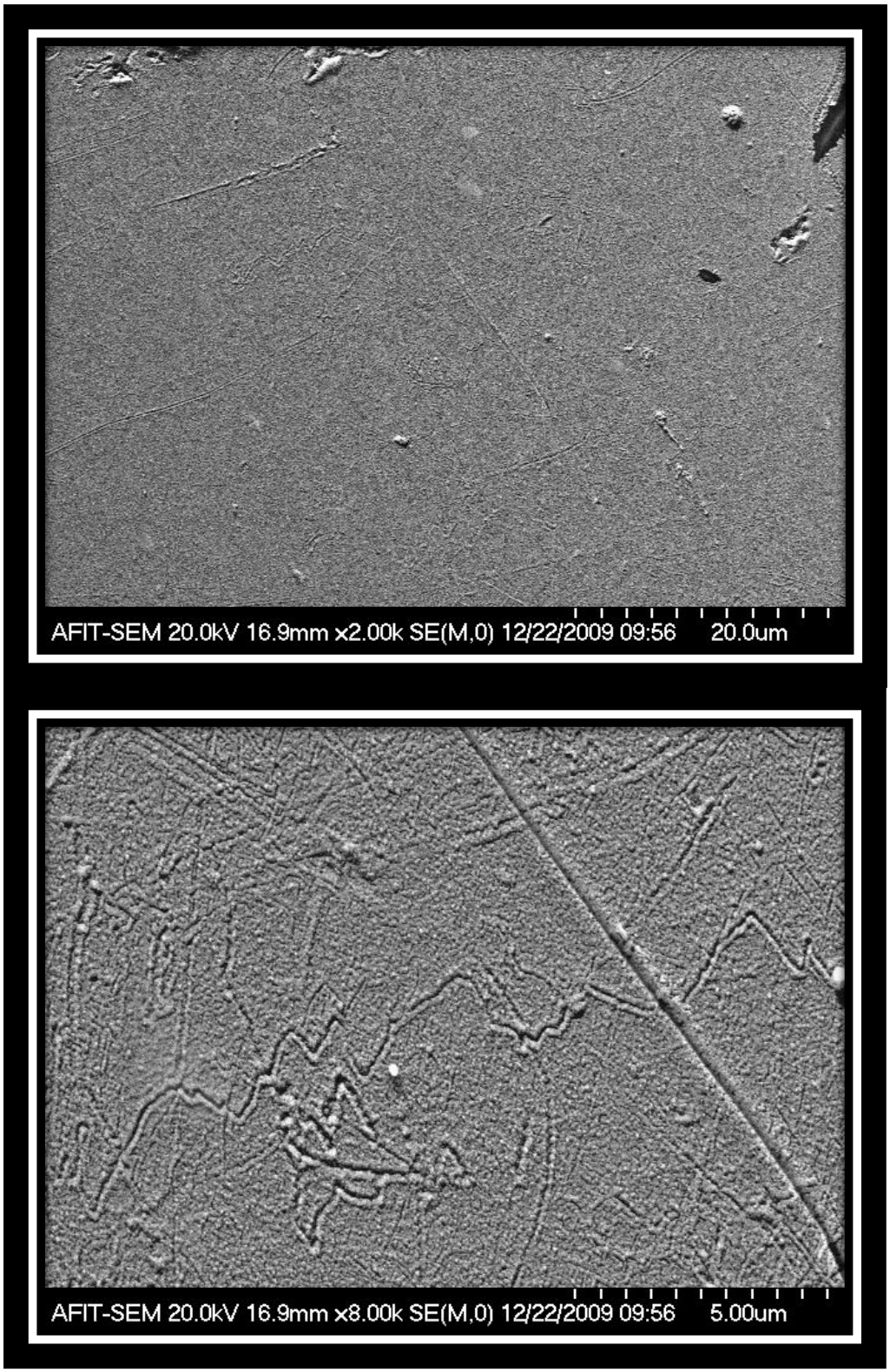

Figure 56: SEM image of silver nanoparticle treated tube with 1:500 linker ratio

Figure 57 provides a 70000x image of the 1:500 ratio sample. This image is magnified within the range necessary to see the expected 10-20 nm sized silver nanoparticles. Figure 57 does not show any difference in surface features relative to Control I or II, and therefore does not appear to have many attached silver nanoparticles. However, the resolution of this image is poor. There is a potential that quantities of silver nanoparticles are on the surface, but not to the expected levels that are desirable.

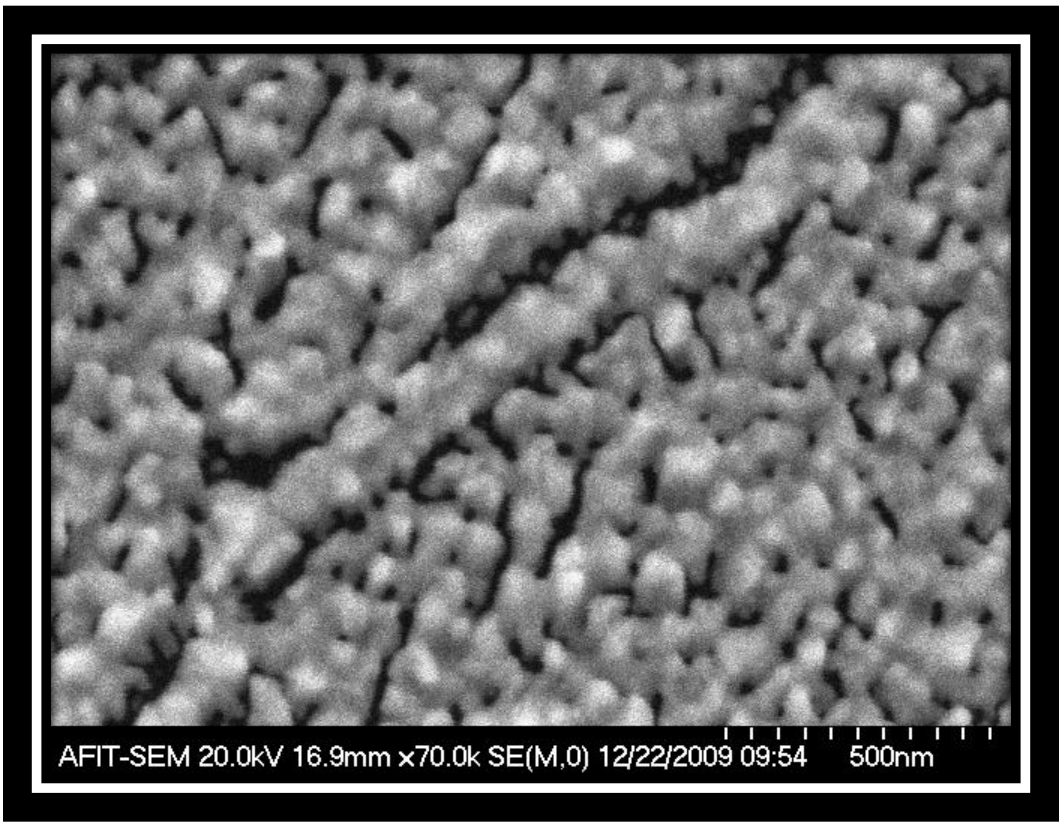

Figure 57: 70,000x SEM image of surface of silver nanoparticle treated capillary tube with 1:500 linker ratio

Figure 58 is a 3000x and 30000x image of 1:50 linker ratio capillary tube samples. In the top image of Figure 58, distinct large spherical particles can be identified. These particles are

once again much larger than expected (1000 nm), and are not currently desired. At a higher magnification of the same sample, the lower image of Figure 58 does not seem to indicate that there are any apparent silver nanoparticles on the surface. Similar to the 1:10 ratio the 1:50 ratio seemed to slightly alter the amount of gold on the surface. This was apparent due to a slight color shift in which the 1:50 ratio sample went from the bright yellowish tint of gold following evaporation, to a more copper color characteristic of the acrylate buffer. Although the 1:50 ratio sample color shift was not nearly as drastic as the 1:10 ratio sample, as demonstrated by the color of solution found in Figure 50 (top left).

Figure 59 is a 3000x and 30000x image of 100 uL PPD containing no n-Heptylamine. This sample did not appear to have the same slight color change that was found in the 1:50 ratio sample, although the same amount of PPD was added. The top image of Figure 59 does not show the same large nanoparticles that were found in Figure 56 and Figure 58. These large nanoparticles may be the consequence of the presence of n-Heptylamine. At a larger magnification, lower image in Figure 59, there does not appear to be any silver nanoparticles. Once again the resolution is poor, but the image provides no verification that silver nanoparticles are present.

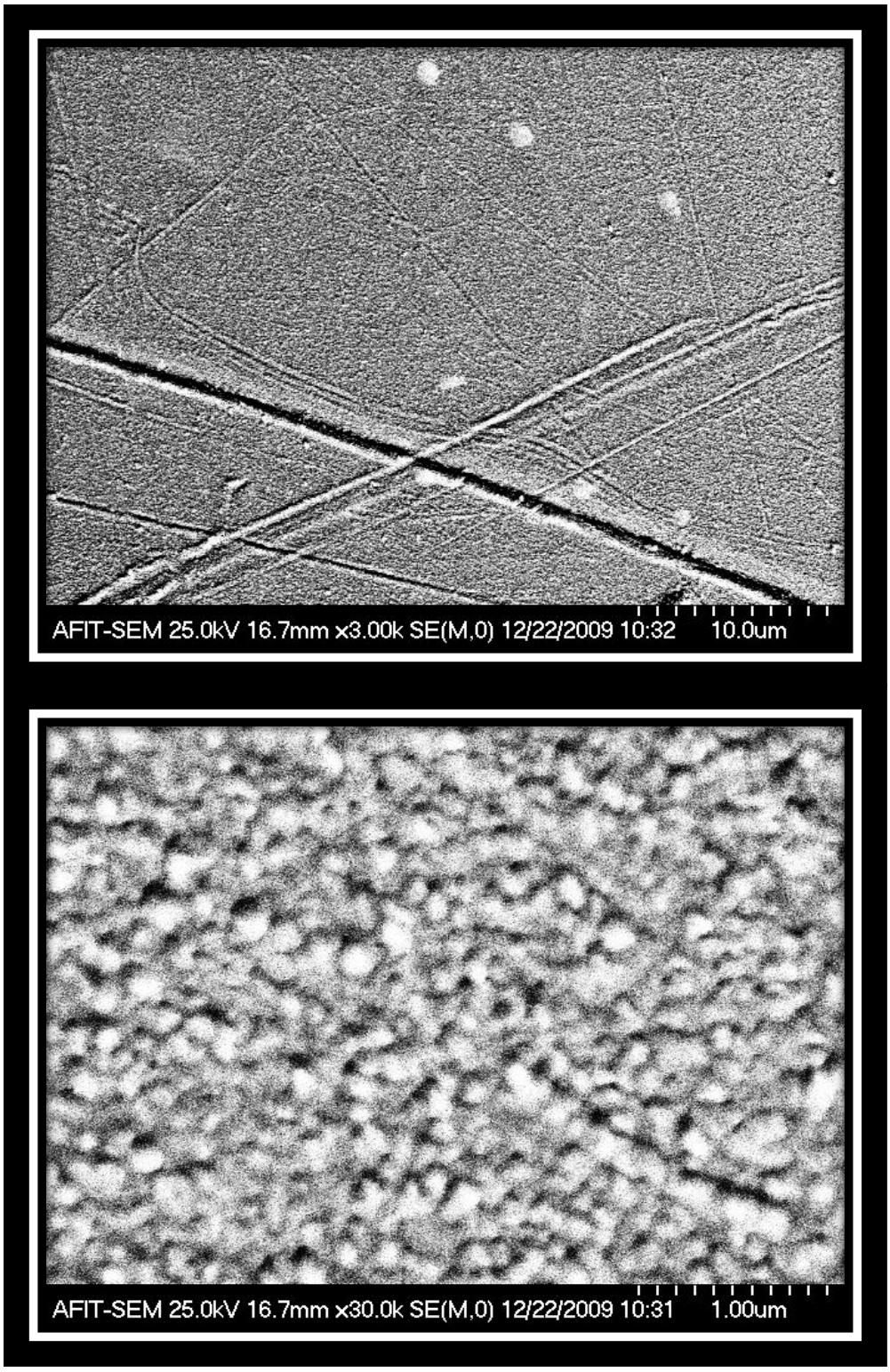

Figure 58: SEM image of silver nanoparticle treated capillary tube with 1:50 linker ratio

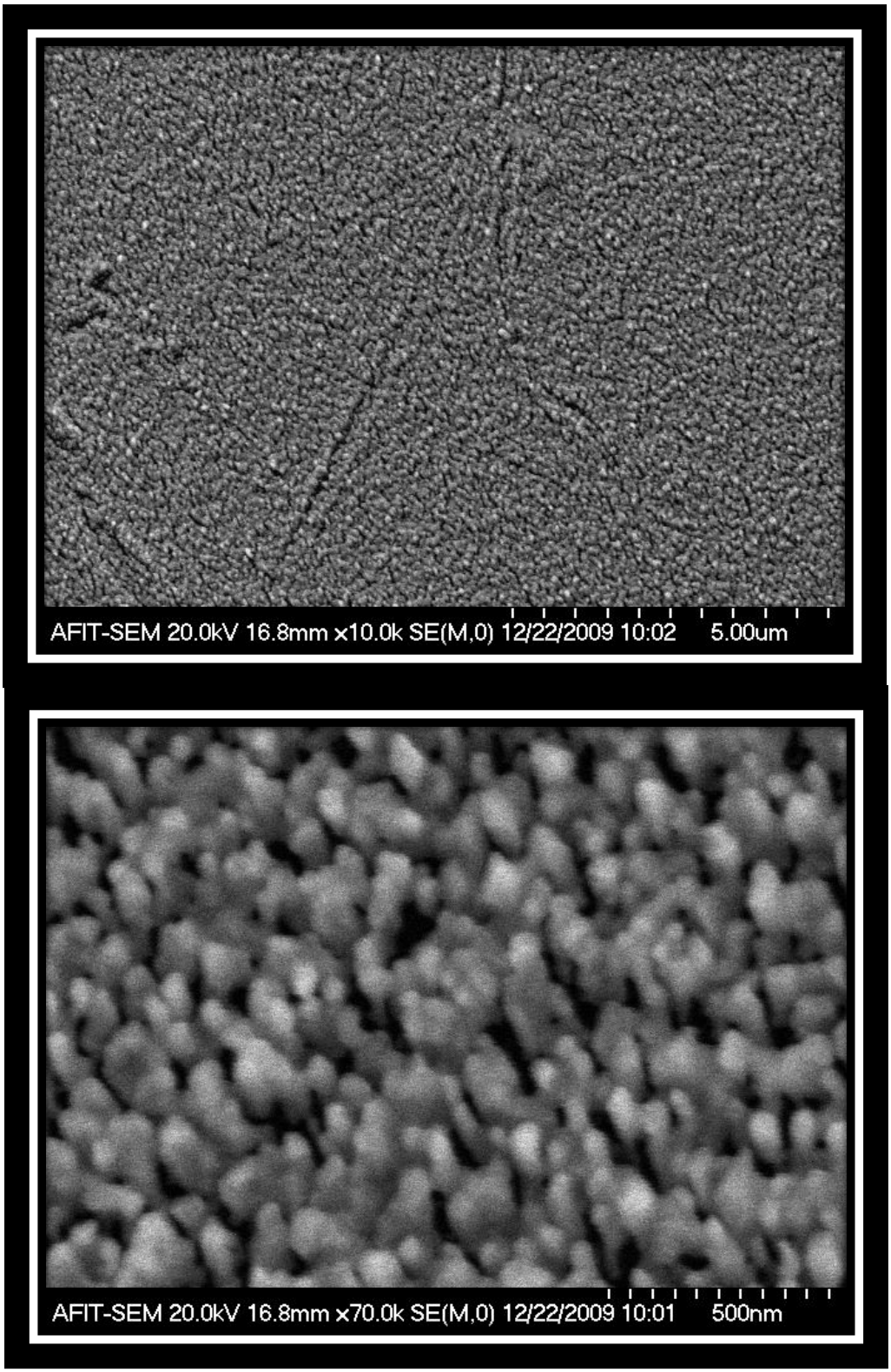

Figure 59: SEM image of silver nanoparticle treated capillary tube 100 µL PPD

Figure 60 is a 1100x and 30000x image of 1:100 ratio silver nanoparticle deposited on the gold coated capillary tube samples. Unlike previous samples, this image clearly verifies that silver nanoparticles are being formed on the surface of these linker treated capillary tubes. A large number of (100 nm) sized particle are present on the surface. These particles appear to range in size from 50-500 nm. They are not accompanied by any of the shadow like features characteristic of many of the other samples. The lower image of Figure 60 better indicates that these nanoparticles are not the byproduct of a scratch. The wide dispersion of these particles throughout the tube surface, in combination with the lack of similar particles found on other samples, provides indication that these are most probably the silver nanoparticles that were deposited from the colloid solution. These silver nanoparticles formed large conglomerates throughout the surface of the capillary tube. These conglomerates are not intended, but do provide the evidence required to verify that this method of deposition can form silver nanoparticles on the surface of gold coated capillary tubes.

The lower image of Figure 60 also depicts a variety of white dots scattered throughout the surface. These dots may correspond to the silver nanoparticles of interest (10-20 nm), but could not be imaged clear enough to confirm their existence. The silver nanoparticles that could be identified in this image range in size from 100-170 nm.

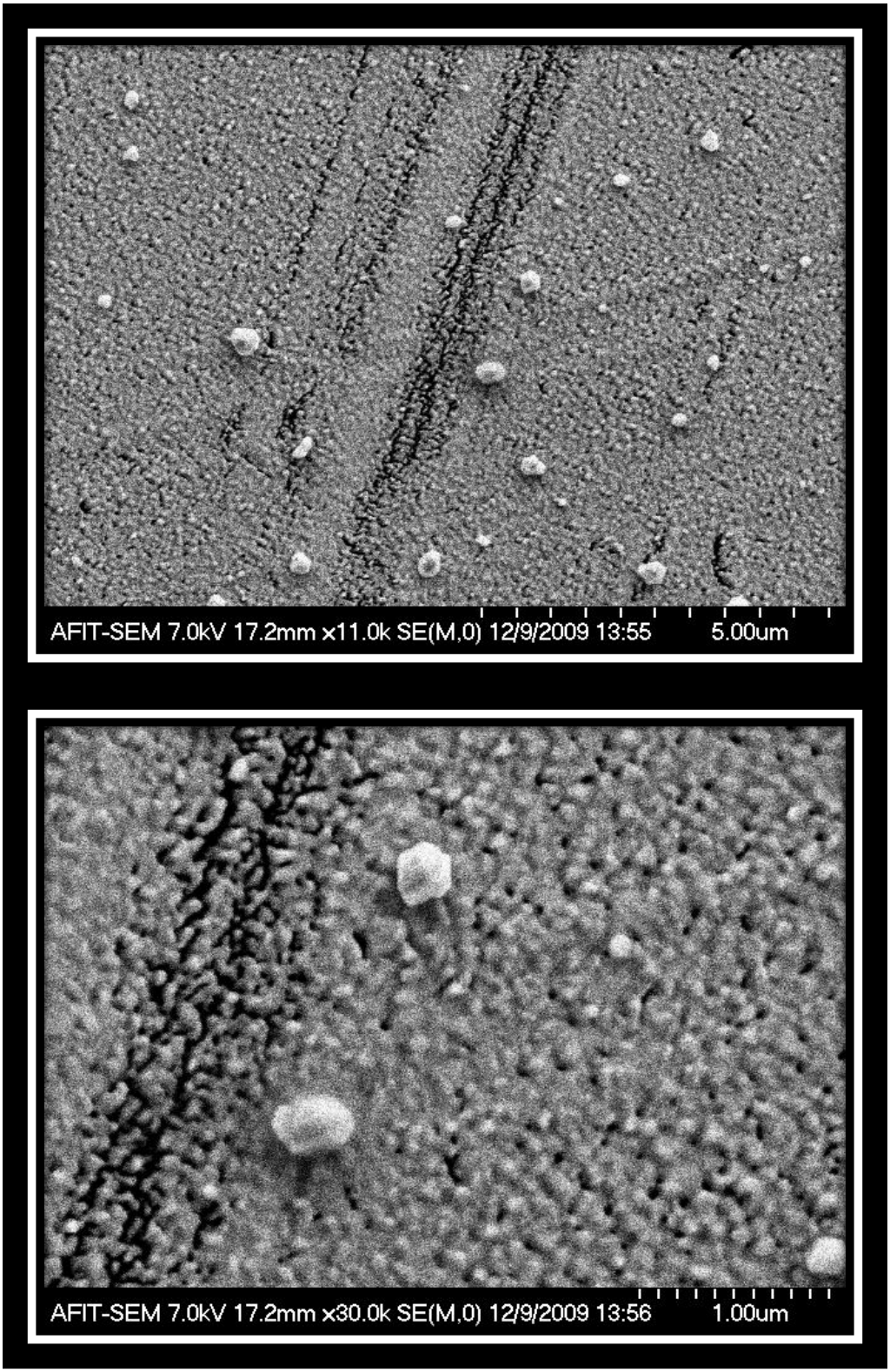

Figure 60: SEM image of silver nanoparticles formation on capillary tube

Figure 61 is 2000x and 8000x image of a gold coated capillary tube mixed in a linker solution of 10 uL of PPD with no n-Heptylamine, and later treated with silver nanoparticles. Both images indicate at these magnifications very few protruding surface features exist. In particular there is a lack of nanoparticle conglomerates that were identified by Figure 60 for the 1:100 ratio sample. The absence of these conglomerates provides further evidence that the presence of n-Heptylamine gives rise to the formation of these clusters.

Figure 62 is a 50000x image of the same sample. This image demonstrates a wide variety of white dots scattered throughout the surface. These dots appear to be the deposited silver nanoparticles. These dots are 10-50 nm in size, are distributed throughout the surface, and are spherical in nature. The distribution of nanoparticle sizes agrees well with what UV-vis and previous data suggest.

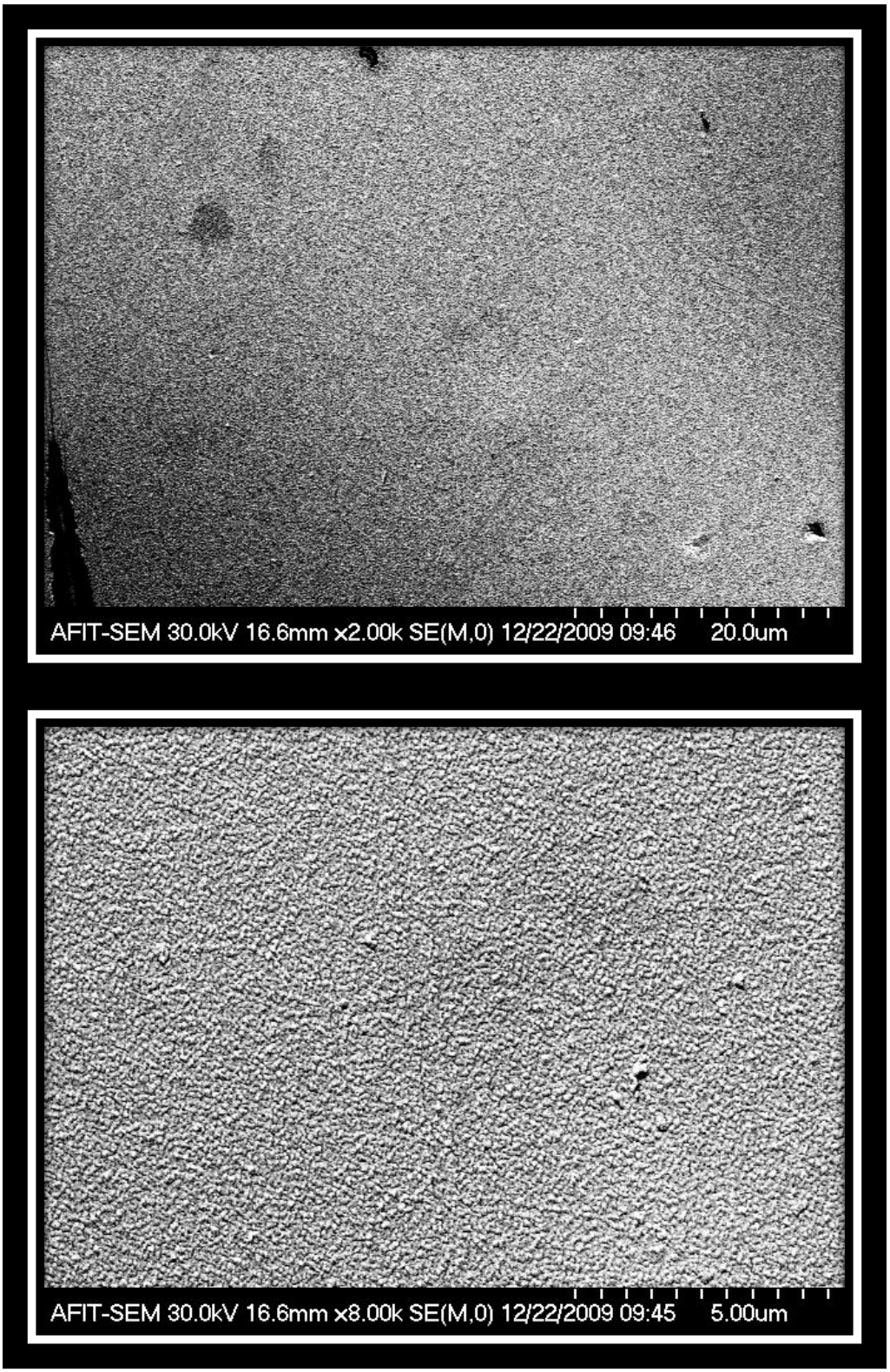

Figure 61: SEM image of silver nanoparticle treated capillary tube 10 µL PPD

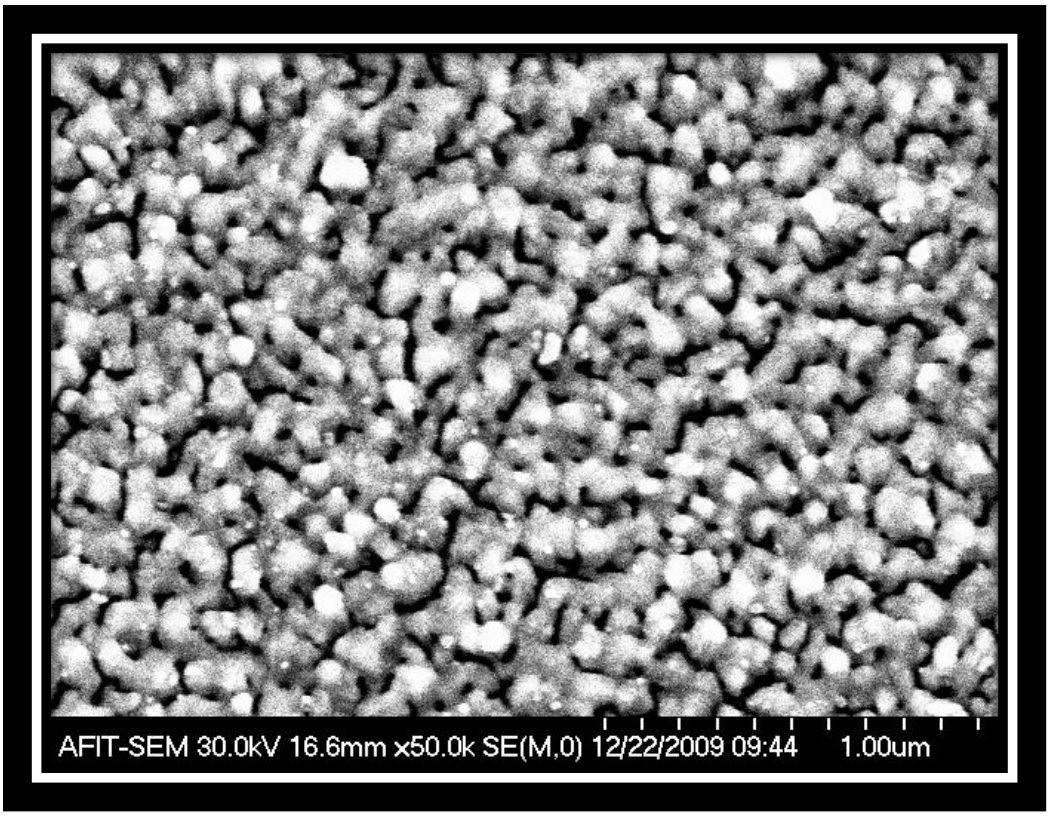

Figure 62 SEM image of silver nanoparticles on treated capillary tube 10 µL PPD. Silver nanoparticle size within the intended 10-50 nm range in size.

Figure 63 further highlights the contrast in images between the gold coated capillary tube treated with 10 µL PPD and the control sample. The control sample (top) has several peaks and valleys, measured through the AFM to be around 15 nm in size. There does not appear to be any color contrast in the image, characteristic of different materials located on the surface. There also does not appear to be any nanoparticle features other than the previously mention peaks and valleys due to gold evaporative coating. The 10 µL PPD sample (bottom image) not only has several nanoparticle features at approximately 100 nm in size, but also has dozens of smaller sized particles at approximately 15 nm in size. All features appear to be spherical in nature.

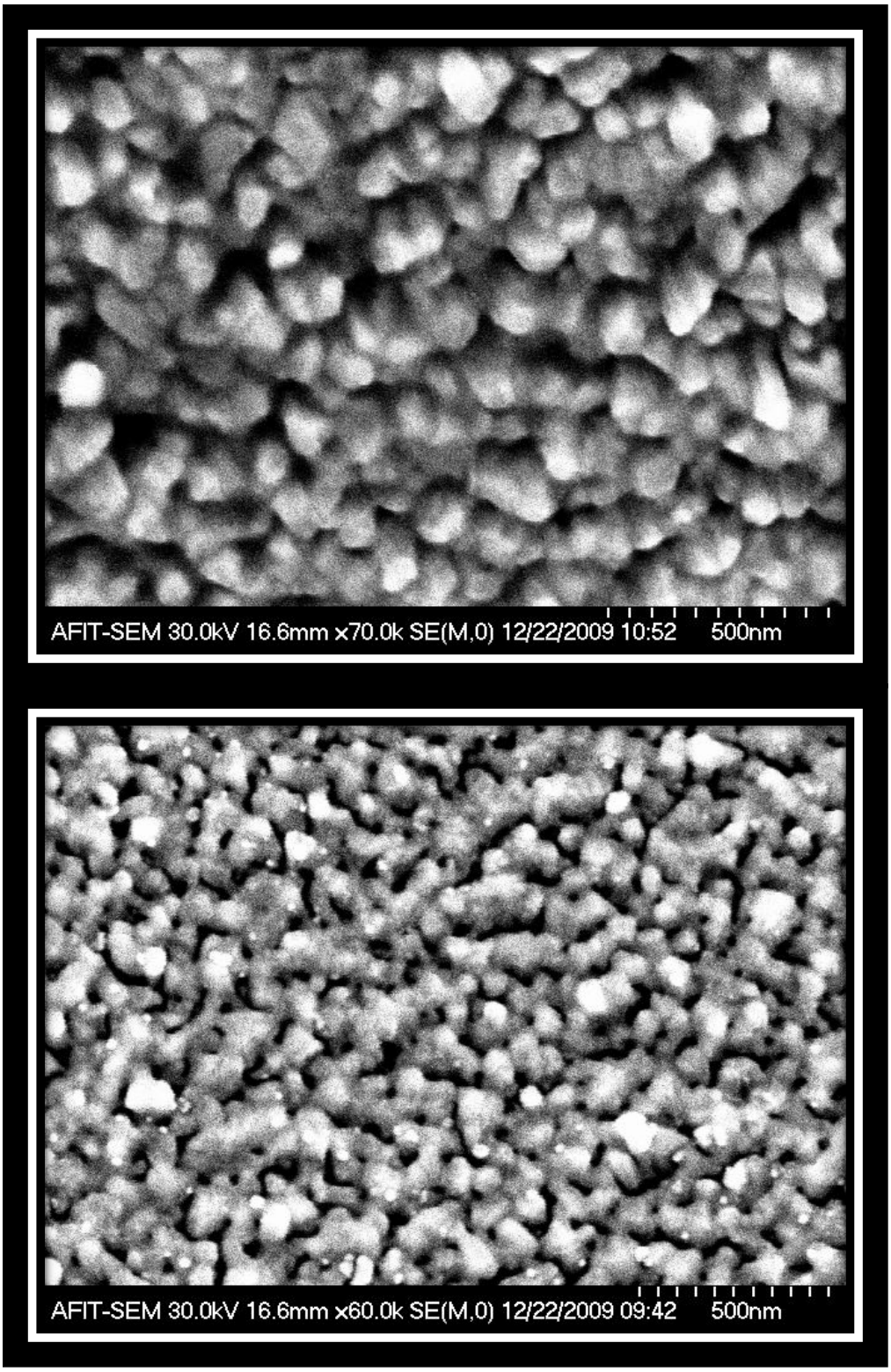

Figure 63: Contrast of sample with (bottom) and without (top) silver nanoparticles

4.7.2 SEM Imaging of Silver Nanoparticles Conclusion

A total of 9 gold coated capillary tube samples (2 cm) were imaged using a SEM. Five of these capillary tubes were treated with linker molecules of PPD and n-Heptylamine. Two of these samples were treated only with PPD. The intent of these linker molecules was to determine what control, if any, one could have over the distribution of silver nanoparticles. Silver nanoparticles of approximately 10-20 nm in size were then deposited on the surface of the capillary tube. An additional two samples were constructed as controls. Control I was a sample with only the gold deposition. Control II was a sample treated with water and then mixed with the silver nanoparticle colloid solution.

Clearly identified on several of the samples are distinct nanoparticle features. These large nanoparticle conglomerates are most likely silver, but are not the intended size based upon the assumed distribution of silver nanoparticles suspended within the colloid solution. One distinct variance in the constructed samples was the differences in linker mixing time. For the 10 μL PPD sample analyzed, the mixing time was 3 hours. For the 1:10, 1:100 and 1:1000 linker ratio samples, the mixing time was 12 hours. The SEM images of all the samples indicate that either the longer mixing time (12 hours) or the addition of n-Heptylamine add to the number of large nanoparticle conglomerates found on the surface.

The 10-20 nm sized nanoparticles, identified by Figure 61 as white dots, are also believed to be silver nanoparticles. These silver nanoparticles are within the intended size distribution. Figure 55 - Figure 60, at high magnifications, may also have these nanoparticles present, but the resolution may not have been clear enough to visually identify them. However, due to the large size of nanoparticle conglomerates also found on those surfaces, the desired field enhancement effects near those smaller nanoparticles may be negated. Finite element modeling of the electric field effects present on a surface imitating that obtained from silver nanoparticles deposition is

required. This analysis would provide a better understanding of the potential to create high local electric fields from a proven nanostructure capability.

4.8 AFM Images of Gold Coated Capillary Tubing with Silver Nanoparticles

AFM images were taken of the gold capillary tubes coated with silver nanoparticles the gold capillary tube sample treated with 1:100 linker ratio, as illustrated in Figure 60. This 1:100 linker ratio contained a distribution of nanoparticles in the size range of 100-700 nm. Figure 64 illustrates the AFM results of a 14 x 40 μm^2 scan of the surface. This image provides a region of interest in which one of the large silver nanoparticles exists, as indicated by the large feature located near the back of the image.

Figure 65 is a 3-Dimensional plot of the peak of interest. This plot demonstrates the full height of the object to be approximately 250 nm, with a width of 600 nm and a base of 2000 nm. It appears as if this object is most likely a silver nanoparticle conglomerate. This object displays many of the characteristics commonly found for the SEM images of the same sample. Although only a limited amount of surface area was imaged, this sample treated with 1:100 linker ratio does not appear to have many features which resemble unidentified objects found in the control samples, as determined through SEM imaging. Therefore it is unlikely this AFM image is of anything other than the nanoparticles also imaged through SEM.

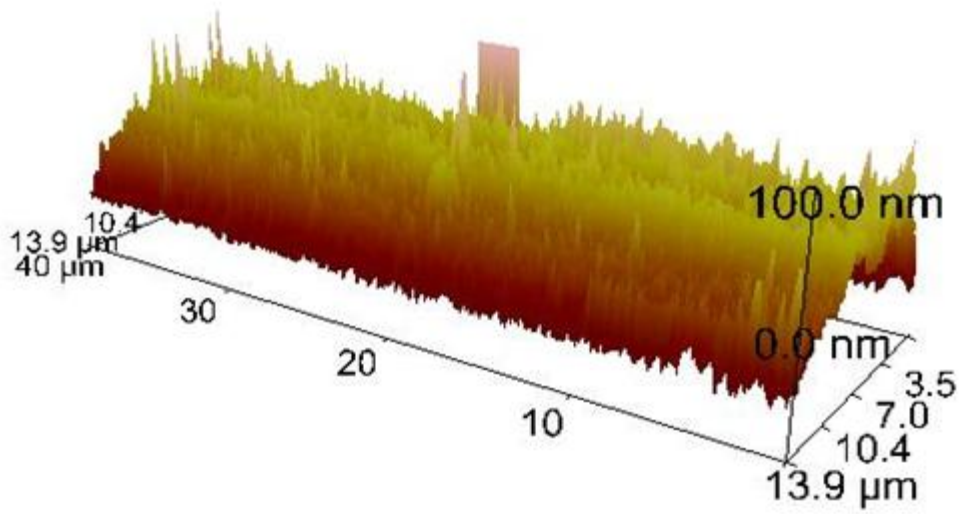

Figure 64: AFM image of gold coated capillary tube sample treated with 1:100 linker ratio

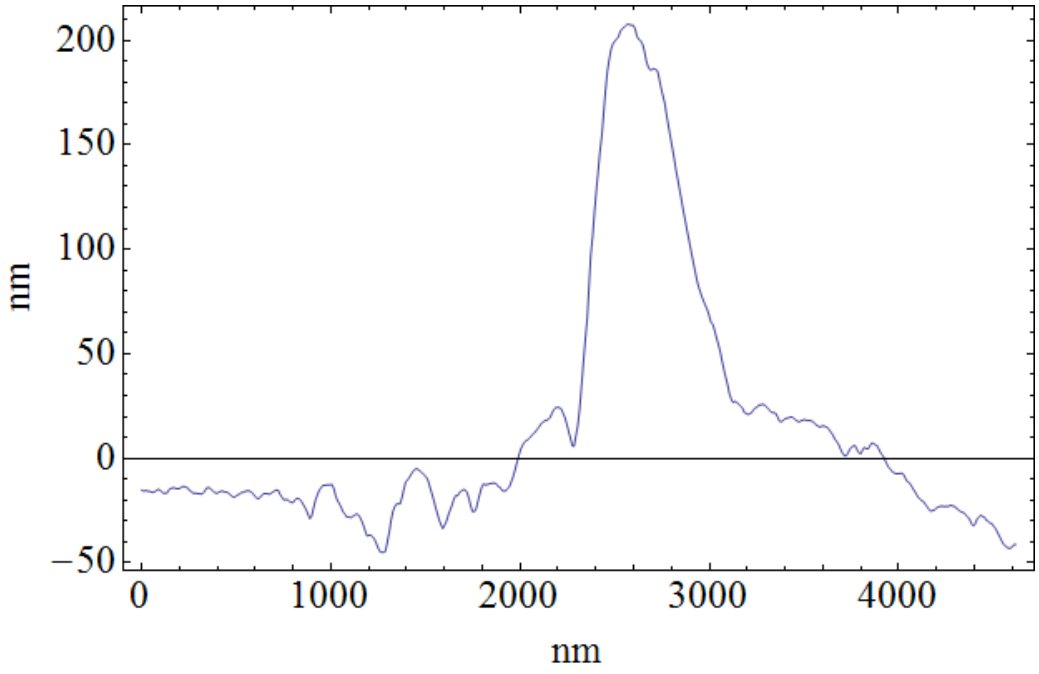

Figure 65: Quantitative plot of bump located in AFM image of gold coated capillary tube sample treated with 1:100 linker ratio

For Figure 64, the scale on this image along the horizontal plane is in μm, while the vertical axis is in nm. This causes the tips of many of these features to appear sharper than reality. The shape of these peaks appears similar to those of Figure 40, which is a sample not treated with silver nanoparticles. The key difference in these peaks compared to those found in Figure 41 is the height of these disperse features. Figure 66 is a 2-Dimensional inspection of a typical scan of a region found in Figure 64.

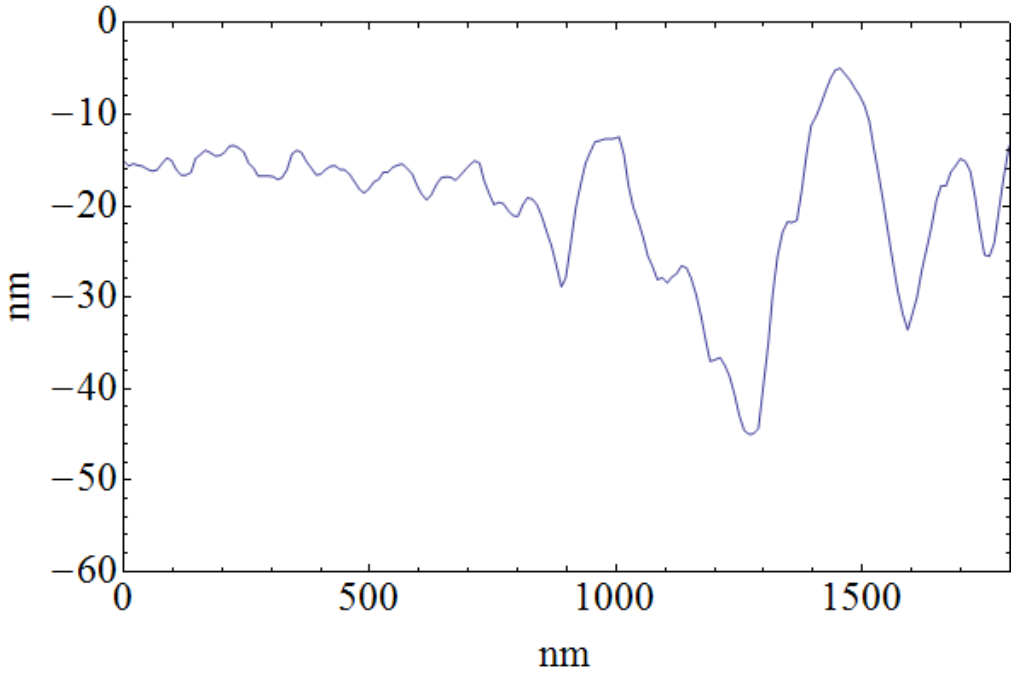

Figure 66: AFM image of surface smoothness for gold coated capillary tube treated with silver nanoparticles and 1:100 linker ratio

Figure 66 demonstrates how through the silver nanoparticle treatment onto the surface of these capillary tubes has increased the surface roughness. There are two possible explanations for this. This increased surface roughness could be caused from silver nanoparticle bonding to the surface. The approximate heights of this particular section appear very similar to larger nanoparticles imaged through the 10μL PPD sample which verified silver nanoparticle bonding.

The widths of these features are much wider than what would be expected for spherical nanoparticles. Conversely, each sample treated with silver nanoparticles underwent additional stages, in particular several mixing processes that may have etched or altered the gold surface. The etching of the surface was visually prevalent for the higher concentrations of PPD, in particular uder the 500 µL of PPD.

Figure 66 also does not provide any evidence to validate the formation of the smaller silver nanoparticles found at the surface of the 10µL PPD sample. The most likely explanation is that the diamond tipped cantilever is too strong and that the method of which the AFM machine scans the surface too interrogative to image these effects appropriately. Each data point captured from the scans also transverses 20 nm, which does not have the precision necessary to image potential nanoparticles 10-15 nm in size.

4.9 Conclusions Regarding Silver Nanoparticle Construction

The capability of depositing silver nanoparticles onto a gold coated capillary tube has been demonstrated. By using p-Phenylenediamine (PPD) and n-Heptylamine as linker molecules these silver nanoparticles were bonded to the capillary tube. These bonds were shown to have the ability to sustain connection over the course of several days while undergoing routine handling. The distribution of silver nanoparticles that were attached to the surface range from 10-700 nm in size. It appears that larger silver nanoparticle conglomerates of 100-700 nm in size can be deposited on the surface by mixing the gold coated capillary tube with 10 µL of PPD and 74.4 uL of n-Heptylamine in 50 mL of water for 24 hours, and then treated in a silver nanoparticle colloid solution for 12 hours. The colloid solution was made mixing 70 mL of water with 1.7 mg of $NaBH_4$ with 4.53m g of $AgNO_3$. Smaller silver nanoparticles ranging in size from 10-50 nm can be bonded to the surface of the capillary tube by mixing 10 µL of PPD in 50 mL of water for 24

hours and then treating with the silver nanoparticle colloid for 3 hours. These smaller nanoparticles are characteristic of the particle sizes known to be suspended within the colloid. Additional samples are required in order to further verify these results. A larger data set will be required, as well as adjustments in silver nanoparticle and linker mixing times. It is also recommended that a different colloid mixture be assembled using sodium citrate as a solution. Due to the increase in surface roughness found through silver nanoparticle and linker treatment, larger sized particles may be more appropriate. The sodium citrate solution provides a colloid with a silver nanoparticle size range centered on about 50 nm. These sized particles may be better suited for experimentation, but will require modeled electrostatic simulations to better determine the most appropriate size.

4.10 PAS measurements of gold coated capillary tubing

4.10.1 Overview

In order to verify that a certain amount of positronium can be formed on gold coated capillary tubes treated with silver nanoparticles, positronium formations must first be observed on gold coated capillary tubes. Positronium formations on the surface were verified through the combination PALS and PsARS measurements. The amount of positronium formation was also estimated.

To aid in the understanding of these measurements GEANT4 simulations were conducted. In particular, samples of capillary tubing with a radial field applied to the inside of the system, were conducted. This internal field could be established through electrical connection to the inner silver layer of the capillary tube, as well as the evaporated deposited layer on the surface. These electrical features may be used to increase the amount of positronium formation on the surface. The GEANT4 simulation will provide the theoretical predictions as to the increase or decrease in the number of positrons that thermalize near the material surface.

PsARS measurements, to include both coincidence and non-coincidence, of the gold coated capillary tube were made. These measurements were conducted in both a vacuum and non-vacuum environments. In the vacuum environment nearly all 3γ terms stem from a byproduct of positronium formations on the surface. Although the capillary tube is primarily not a metal, the positronium fraction in un-irradiated semiconducting materials is still close to the nominal $\frac{1}{372}$ value, at standard temperature. In the non-vacuum environment the outcome is much less known. Although nearly all positrons annihilating within or on top of the surface should result in 2γ events, a certain amount of positrons may moderate within the Ore gap. These slow positrons can interact with the surrounding air (in-between tube and vacuum chamber) forming positronium states in some cases.

Additionally, a digital PALS measurement of the gold coated capillary tube was conducted in vacuum. This measurement additionally verified the formation of positronium on the surface of the gold coated tube. This verification affirms that a similar gold coated capillary tube treated with silver nanoparticles has the potential to form positronium states within the silver nanoparticles.

4.10.2 GEANT4 Simulation of Gold Coated Capillary Tubing

A GEANT4 simulation of 10,000 positrons was conducted for a radially applied electric field correlating to a applied voltage of 0, 10 , and 100 volts between inner silver and outer gold layers of the capillary tube. The full geometry was implemented in the PositronCapillaryTubeDetector.cc file as demonstrated in Appendix F. The physics list was altered to only include positron scattering interactions. The electric field was established through a point specific calculation in which each sampled data point would recalculate the field determined to be

$$\bar{E}\text{field} = \text{Efield}\frac{\text{Position}(x,y)}{\text{Abs}(\text{Position}(x,y))} \tag{47}$$

for the specified x and y directions only. In order to decrease uncertainty in measurement due to non-continuous field calculation a step limiter of 1 μm was implemented. Each energy increment data point was exported to be analyzed using additional software tools. The number of positrons that thermilize within a specific thickness within the capillary tube is demonstrated by Figure 67.

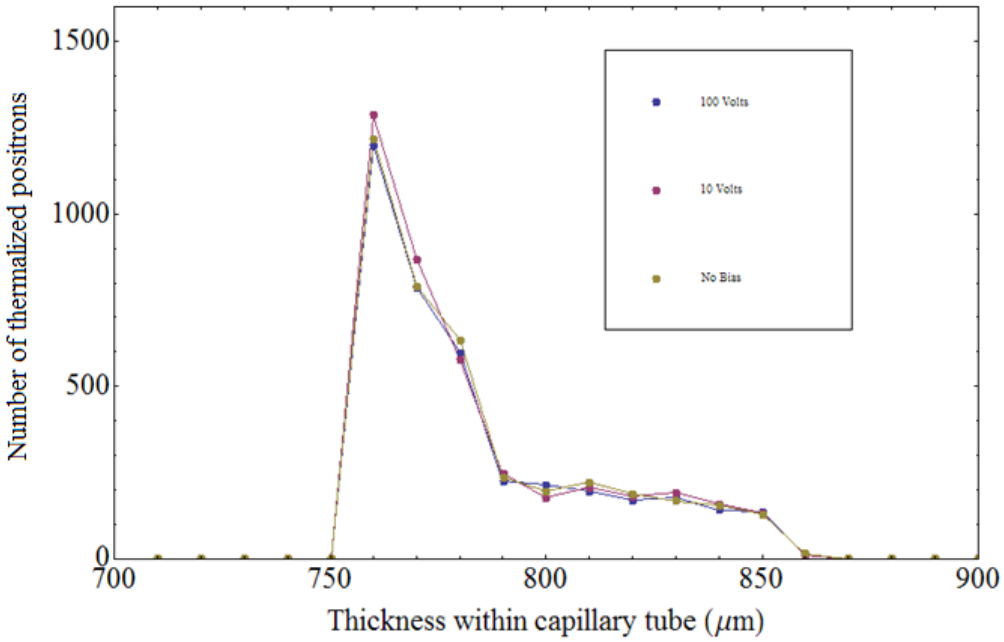

Figure 67: Thermalization range of positrons as determined through GEANT4 simulation

The results graphically highlighted by Figure 67 indicated that through application of an internal electric field within the capillary tube up to 100 volts, makes a statistically insignificant difference in the location of positron thermalization. Although in an applied field the positron will drift through a material, it appears that the number of positrons that thermalize near the end of the capillary tube (850 μm) remains nearly unchanged. However, because GEANT4 is insensitive to positron thermal energies, experimental evidence may reject this result.

4.10.3 PsARS measurements of gold coated capillary tubing

PsARS measurements were taken of a 15 cm gold coated capillary tube. The identical radioactive NaCl solution that was used for dodecaborate and copper samples was once again used to deposite ^{22}Na within the capillary tube using a 22 gauge syringe. A total of 0.26 µCi of ^{22}Na was intended to be contained within the tube. The sample was placed onto a designed holder, placed on top of tin foil held in contact with a hot plate.

The sample was then heated, causing a portion of the radioactive NaCl to evaporate within the capillary tube. Following full heating process, scanning the area near the capillary tube indicated that much of the radioactive NaCl evaporated out of the tube and did not reside within. This lost radioactivity was later estimated to be approximately 0.15 µCi, with approximately 0.10 µCi of ^{22}Na retained within the capillary tube sample.

The gold coated radioactive capillary tube was then soldered to a Kurt J. Lesker vacuum voltage feed-through with 2 ¾" flange size in two places. The first connection point was made with 22 gauge electrical wire with the 2.6 µm silver layer inside of the capillary tube. This connection was successfully tested for electrical conductivity. The second connection was made with thin electrical wire wrapped around both the gold coated capillary tubing and 22 gauge wire also soldered to the electrical feed-through. This connection was also tested for conductivity. Both positions were tested to make sure connections were isolated, that no readable current could be measured when bias was applied to one connection and not the other.

For the majority of capillary tube measurements the experiment will be conducted under vacuum. A Kurt J. Lesker 10" vacuum (Nipple) with 2 ¾" Flange and 1 ½" inner diameter was used as the vacuum chamber. Vacuum tubing (3ft) connected the chamber to a roughing pump. The roughing pump was used to reduce pressure from atmosphere to 10^{-3} Torr . A 4 pin electric

feed-through was connected to the chamber, for the designed use of having the ability to apply external electric fields within the vacuum chamber. A Varian multi-gauge reader was used to measure pressure from atmosphere to 10^{-3} Torr. A vacuum tee and valve connected the chamber to a Gamma Vacuum 10S ion pump to be used in experimentation requiring further reduced pressures. A wooden holder was designed to align the center of the chamber with the center of the NaI ring detector. The full vacuum configuration is depicted by Figure 68.

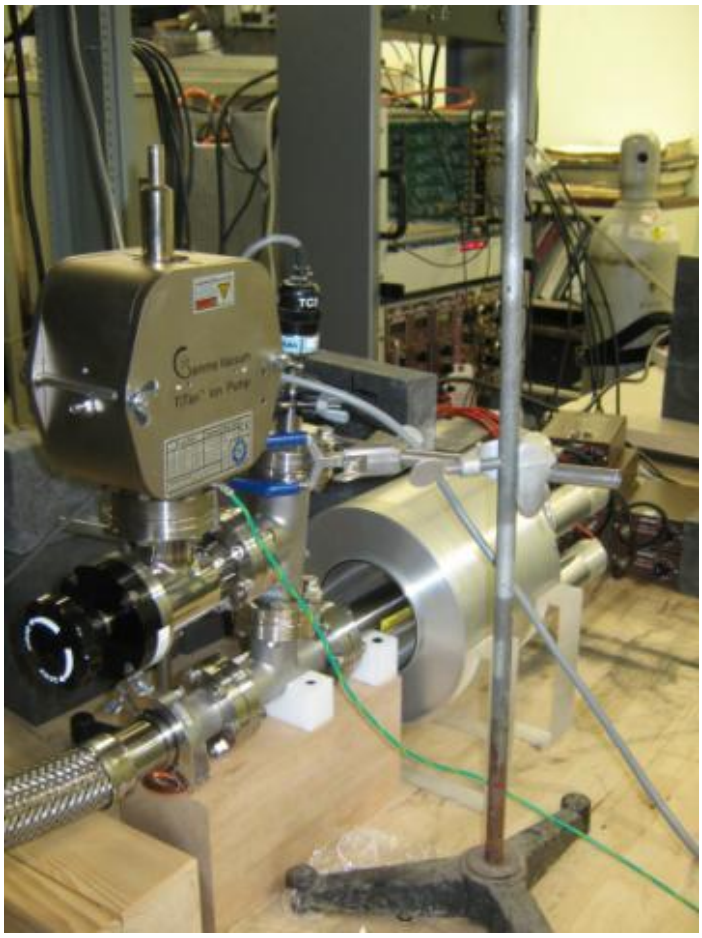

Figure 68: Vacuum setup

PsARS measurements were conducted using both coincidence and non-coincidence methods. Measurements were taken at vacuum level ($<10^{-3}$ Torr) and at 1 atm. The results of the measurements are indicated by Table VIII.

Table VIII: PsARS measurements of gold coated capillary tube

Pressure	Coincidence 3γ/2γ (1/372)	Non-Coincidence 3γ/2γ (1/372)
Vacuum	2.44	3.78
STP	2.92	3.85

As Table VIII indicates, both coincidence and non-coincident measurements agree that the PsARS measurements conducted in vacuum result in positronium formations on the surface of the gold coated capillary tube. The coincidence PsARS measurement also requires an additional geometrical correction factor in order to take into account the amount of capillary tubing not centered within the vacuum chamber. This correction factor was not applied, but is most likely the cause for the difference in 3γ/2γ ratio for the alternative method. The non-coincidence measurement better accounts for this geometrical correction factor by not requiring the capture of all simultaneous 3γ emissions, and hence better reflects the more appropriate 3γ/2γ ratio. Both measuring techniques takes into consideration the attenuation factors attributed to the 1/8" thickness of the steel vacuum chamber. The approximation to this factor can be determined by analyzing

$$I = I_o e^{-\mu\rho x} \tag{48}$$

in relation to 511 keV 2γ photons and approximately 300 keV 3γ photons. Where I is the final intensity, I_o is the initial intensity, μ is the mass attenuation coefficient, ρ is the density of material, and x is the propagation thickness.

Also of significance is the fact that the 3γ/2γ ratio did not decrease for non-vacuum measurements. Using the Varian multi-gauge reader, the pressure was accurately known, and yet positronium annihilations resumed without vacuum conditions. Because it is unlikely that such a

large number of 3γ events arose from continual positronium annihilation on the surface of the gold coated capillary tube, the more prominent explanation is that many of the positrons were moderated through the tube and ejected into the air environment. At low energies positrons can have large cross sections for positronium formations. This is especially true for the noble gases, as is demonstrated for Argon by Figure 69.

Equation (49) demonstrates how for probabilities not approaching unity, how the probability for positronium formation can be determined

$$\text{Prob} = n\sigma_{\text{Ps}}\text{dx} \tag{49}$$

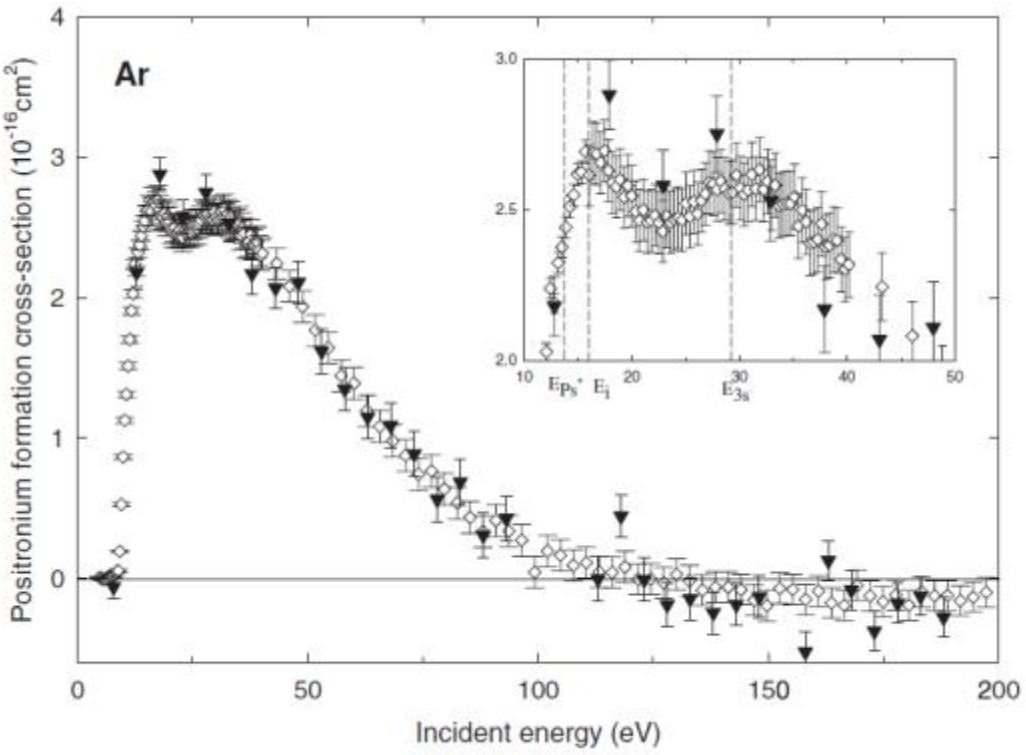

Figure 69: Positronium formation cross section for Argon [53]

Where n is the number density and σ_{Ps} is the cross section for positronium formation.

If the assumption is made that the total cross section for positronium is entirely due to Argon, which makes up approximately 1 percent of air atomic concentration, then the probability for

positronium formation within the 3 cm separation between capillary tube and vacuum chamber is 7.5 percent. Clearly there is a multitude of positrons within this Ore gap (6.8-100 eV) that undergo positronium formation.

4.10.4PALS of gold coated capillary tubing

Digital PALS measurements of the gold coated capillary tube were conducting using DigitalPALS1.16, an Igor Pro software program, produced and maintained by Dr. Michael Lindsay of Eglin AFRL. Digital PALS establishes a dual connection between two PALS detectors and a Tektronics oscilloscope in order to trigger off coincident events within a 100 ns window. An additional Igor Pro program DigitalPALStools1.3, also designed and maintained by Eglin AFRL, correlates the data points for the two detectors. This data is then imported and analyzed in PALSfit, a PALS lifetime least squares fit routine.

A PALS measurement of the gold coated capillary tube was conducted in vacuum ($<10^{-3}$ Torr) over 14 days, a total of 100,000 good counts were acquired. Figure 70 graphically illustrates the resultant PALS spectrum. As is clearly demonstrated, several longer lived positronium species are present in the material. Due to the relatively low number of counts (10^{6} standard) the PALsfit software program was unable to find a least squares fit in order to determine lifetimes and intensities. However, an approximation can be calculated by analyzing the number of positronium lifetime counts relative to the total number of counts. The intensity of ortho-positronium can be calculating the total number of counts in the predominate positronium term (47 ns) divided by the total number of positron lifetime counts, and multiplying by their relative lifetimes. This relationship is demonstrated by Equation (50).

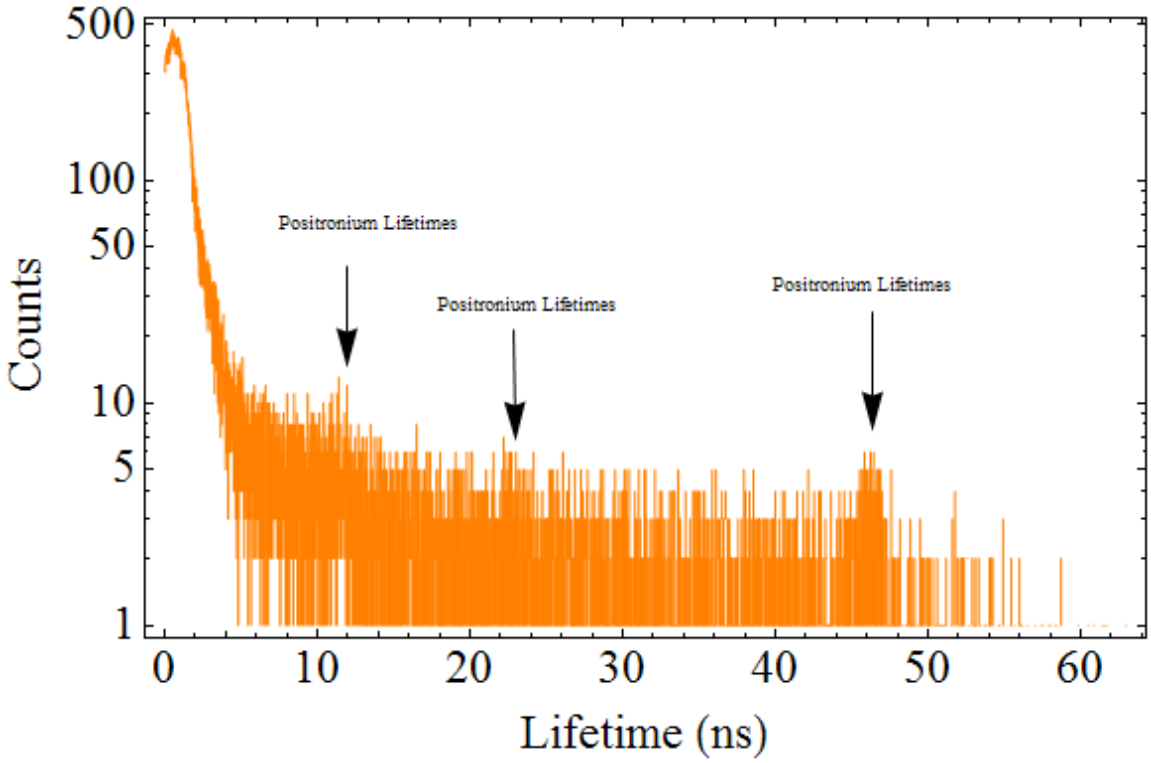

Figure 70: Lifetime spectrum obtained of gold coated capillary tube

$$\text{oPsIntensity} = \frac{\tau_{o-\text{Ps}}}{\tau_{e^+}} \frac{\text{counts}_{o-\text{ps}}}{\text{counts}_{e^+}} \tag{50}$$

According to Equation (50) the measured intensity of the 47 ns lifetime component is equal to 8.5 percent. It appears that at least 8.5 percent of the positrons emitted from the capillary tube are forming positronium states, most likely on the gold coated surface.

5 Conclusion

Coincident and non-coincident PsARS was applied to copper, dodecaborate solutions, and gold coated capillary tube samples. Both methods were verified to be a reliable measurement of 3γ/2γ ratios of annihilation radiation based upon the reproducibility of the $\frac{1}{372}$ copper ratio and aqueous solution results. Dodecaborate PsARS analysis indicates the formation of positronic

dodecaborate. Results also confirmed that positronium formation occurs at higher concentrations of dodecaborate. However, PsARS analysis neither confirms nor refutes the evidence to support para-positronium quenching at 10^{-2} M. It is possible that longer count times are required to further reduce uncertainty in measurements. If measurements were retaken, sample collection times of 12 hours should be performed as opposed to an hour and a half. Additional PALS measurements should also be performed in order to provide the insight into whether or not sample compositions have changed.

PsARS and PALS measurements of the gold coated capillary tube indicate a relatively large amount of positronium formation on the gold surface. The verification of positronium formations on the surface of these capillary tubes was essential in confirming that these radioactive tubes are capable of providing the environment necessary for future lifetime analysis with silver nanoparticles.

Both coincident and non-coincident PsARS in their current form can continue to be used for positronium formation studies, in particular on capillary tubing. Electric fields can be applied to the inner (silver) and outer (gold) conducting surfaces of the capillary tubing to determine whether or not any increase in positronium on the surface is observed. PsARS can perform positronium formation studies within semiconductors and ion implanted materials. By irradiating a sample and continuously annealing a system through incremental temperate ranges, the defect and ion concentration of several species can be determined by analyzing the increases and decreases in ortho-positronium intensity.

Both coincident and non-coincident PsARS in their current form can also be used to verify digital PALS positronium intensity values. This additional intensity verification can be used to form a better understanding of whether or not any 3γ efficiency correction factors are required for PALS measurements. This verification also increases the confidence of all lifetime data, which is currently used to determine semiconductor defect concentrations and porous void size.

Currently, the non-coincident PsARS is the preferred method due to the smaller uncertainty relative to coincident PsARS. However, by requiring all six channels within the DGF-4C modules to record 3γ counts, Coincident PsARS, has the potential to produce a 3γ spectrum within hours. A capability that is not currently being demonstrated anywhere in the world. This capability should be explored.

This research demonstrated the capability of constructed nanoparticle arrays of 10-700 nm in size onto gold coated capillary tubing. The ability to also control nanoparticle distributions was also demonstrated. Further research should focus on demonstrating proficiency of methods as well as testing sodium citrate mixtures and silver coated capillary tubes. This research provided the initial steps essential in developing the materials and expertise required to verify positronium lifetime extensions through interactions with external electromagnetic fields.

Appendix

Appendix A: PMT Bias

Table IX: Bias applied to NaI PMTs

PMT Temporary #	HV Bias (kV)
1	0.844
2	0.836
3	0.841
4	0.843
5	0.837
6	0.840

Appendix B: Channel Settings

Table X: Channel gain and decay time settings

Module 1	Gain [v/v]	Decay Time (µs)
Ch0	0.28	34.44
Ch1	0.30	39.81
Ch2	0.37	48.01
Ch3	0.30	38.73
Module 2		
Ch 1	0.36	33.52
Ch2	0.72	46.54

	Trigger Filter (µs)	Energy Filter (µs)
Rise Time	0.100	1.20
Flat Top	0.100	1.20
Threshold	20	

	Time (µs)
Trace Length	5.0
Delay	2.0
PSA Start	0.025
PSA End	4.975

Appendix C: Energy calibration

$$A + Bx + Cx^2 \tag{51}$$

Table XI: Calibration best fit curve for each DGF-4C channel

PMT	A	B	C
Module 1 Ch0	-1.5901	0.0163653	7.0101×10^{-8}
Module 1 Ch1	-4.401	0.0153285	1.24578×10^{-7}
Module 1 Ch2	-8.9334	0.0139532	1.0146×10^{-7}
Module 1 Ch3	-9.884	0.0122498	7.83594×10^{-8}
Module 2 Ch1	-10.2602	0.0134281	7.83594×10^{-8}
Module 2 Ch2	-15.3206	0.0177699	9.78552×10^{-9}

Appendix D: Instrinsic efficiency

$$\text{eff[x]}: = \frac{m}{\text{Log}[xb]} + c \tag{52}$$

Table XII: Intrinsic efficiency best fit curves

Channel	**M**	**B**	**C**
Mod1Ch0	1.47	0.84	0.2
Mod1Ch1	1.461	0.844	0.19
Mod1Ch2	1.444	0.848	0.2
Mod1Ch3	1.514	0.829	0.2
Mod2Ch1	1.375	0.868	0.174
Mod2Ch2	1.158	0.932	0.145

Appendix E: Igor PsARS Code

```
#pragma rtGlobals=1           // Use modern global access method.
//StrConstant DPT_CodeVersion="Digital2g3g_1.0.ipf"

Menu "Digital 2g3g"
"2g3gDistribution" ,LoadDigital2g3gdatFile()
End

Function LoadDigital2g3gdatFile()   // Saves the 2D coefficients for
both start-stop and stop-start aquasitions

      variable filenum
      Open /T=".dat"/M="Select 2g3g.dat File"/R filenum
      if (cmpstr(s_filename,"")==0) // if open dialog box is cancelled
or has an error upon file select, break function and return the error.
            Beep
            print "Import aborted!"
            return -1
      endif
      NewPath /Q/O g3gDataFilePath,
removelistitem((itemsinlist(s_filename,":")-1),s_filename, ":")
      LoadWave /K=1/Q/O/P=g3gDataFilePath/G/L={0,0,0,0,0}/N=datacolumn
stringfromlist((itemsinlist(s_filename,":")-1),s_filename, ":")

      Variable i =0,,j=0,k=0,stepk=0,l=0,stepl=0,stepk2=0,stepl2=0
      Variable
stepi,stepj,inputcountrate,g3gcorrectionminus,g3gcorrectionplus

      Duplicate /O datacolumn0 Module1Counts
      Duplicate /O datacolumn4 Module2Counts
      Duplicate /O datacolumn3 TimeDataMOD1
      Duplicate /O datacolumn7 TimeDataMOD2
      Duplicate /O datacolumn2 Module1ChannelData
      Duplicate /O datacolumn6 Module2ChannelData
      FindPeak/B=4/Q Module1Counts
      Variable max1=V_PEAKVal
      FindPeak/B=2/Q Module2Counts
      Variable max2=V_PEAKVal

      MAKE/O/N=(max1) MOD1CH0
      MAKE/O/N=(max1) MOD1CH1
      MAKE/O/N=(max1) MOD1CH2
      MAKE/O/N=(max1) MOD1CH3
      MAKE/O/N=(max2) MOD2CH1
      MAKE/O/N=(max2) MOD2CH2

      Do
            Stepi=Floor(i/4)
```

```
            MOD1CH0[Stepi]= -
1.59011+0.0163653*Module1ChannelData[i]+7.01019*10^-
8*(Module1ChannelData[i])^2
            MOD1CH1[Stepi]=-
4.40101+0.0153285*Module1ChannelData[i+1]+1.24578*10^-
7*Module1ChannelData[i+1]^2
            MOD1CH2[Stepi]=-
8.93341+0.0139532*Module1ChannelData[i+2]+1.01467*10^-
7*Module1ChannelData[i+2]^2
            MOD1CH3[Stepi]=-
9.8843+0.0122498*Module1ChannelData[i+3]+7.83594*10^-
8*Module1ChannelData[i+3]^2


            i+=4

      While (Stepi < max1)

            Do

            Stepj=Floor(j/2)

            MOD2CH1[Stepj]=-
10.26018+0.0134281*Module2ChannelData[j]+7.83594*10^-
8*(Module2ChannelData[j])^2
            MOD2CH2[Stepj]=-
15.3206+0.01776989*Module2ChannelData[j+1]+9.78552*10^-
9*(Module2ChannelData[j+1])^2

            j+=2

      While (Stepj < max2)
      //Duplicate /O datacolumn0 Positron3gCoincidenceTimeD
      //Duplicate /O datacolumn4 Positron2gCoincidenceTimeD
       MAKE/O/N=(max1) Positron3gCoincidence
       MAKE/O/N=(max1) Positron3gCoincidenceTimeD1//To determine time
distribution of 3 Gamma events
       MAKE/O/N=(max2) Positron2gCoincidence
       MAKE/O/N=(max2) Positron2gCoincidenceTimeD1 //To determine time
distribution of 2 Gamma events
       MAKE/O/N=(max1) Positron3gCoincidenceReal
       MAKE/O/N=(max2) Positron2gCoincidenceReal
       MAKE/O/N=(max1) Positron3gCoincidenceTimeD
       MAKE/O/N=(max2) Positron2gCoincidenceTimeD


       Do
            k+=1
            If( (MOD1CH0[k]<380) && (MOD1CH1[k]<380) &&
(MOD1CH2[k]<380)&&
(MOD1CH3[k]<380)&&(MOD1CH0[k]+MOD1CH1[k]+MOD1CH2[k]+MOD1CH3[k]>910
)&&(MOD1CH0[k]+MOD1CH1[k]+MOD1CH2[k]+MOD1CH3[k]<1110 ))
                        Positron3gCoincidence[stepk]=MOD1CH0[k]
                  Positron3gCoincidence[stepk+1]=MOD1CH1[k]
                        Positron3gCoincidence[stepk+2]=MOD1CH2[k]
```

```
                        Positron3gCoincidence[stepk+3]=MOD1CH3[k]

                        //Time Factor should not take into account
channel that doesn't record energy. Hence if-elseif statements
                        If (MOD1CH0[k]==0)
                              TimeDataMOD1[4*k-4]=TimeDataMOD1[4*k-3]
                  elseif(MOD1CH1[k]==0)
                        TimeDataMOD1[4*k-3]=TimeDataMOD1[4*k-4]
                        elseif(MOD1CH2[k]==0)
                        TimeDataMOD1[4*k-2]=TimeDataMOD1[4*k-4]
                        elseif(MOD1CH3[k]==0)
                        TimeDataMOD1[4*k-1]=TimeDataMOD1[4*k-4]
                        Endif


      Positron3gCoincidenceTimeD1[stepk/4]=Abs(TimeDataMOD1[4*k-4]-
TimeDataMOD1[4*k-3])+Abs(TimeDataMOD1[4*k-4]-TimeDataMOD1[4*k-
2])+Abs(TimeDataMOD1[4*k-4]-TimeDataMOD1[4*k-1])
                        If ( Positron3gCoincidenceTimeD1[stepk/4] <=1 )

      Positron3gCoincidenceTimeD[stepk2/4]=Positron3gCoincidenceTimeD1[
stepk/4]+1

      Positron3gCoincidenceReal[stepk2]=Positron3gCoincidence[stepk]

      Positron3gCoincidenceReal[stepk2+1]=Positron3gCoincidence[stepk+1
]

      Positron3gCoincidenceReal[stepk2+2]=Positron3gCoincidence[stepk+2
]

      Positron3gCoincidenceReal[stepk2+3]=Positron3gCoincidence[stepk+3
]


                        stepk2+=4

                  EndIf
            stepk+=4
         EndIf


      While (k < max1)

      Do
             l+=1
           If( (MOD2CH1[l]>460) && (MOD2CH2[l]>460) && (MOD2CH1[l]<560)
&& (MOD2CH2[l]<560) &&
(MOD2CH1[l]+MOD2CH1[l]<1110)&&(MOD2CH1[l]+MOD2CH1[l]>910))
                  Positron2gCoincidence[stepl]=MOD2CH1[l]
                        Positron2gCoincidence[stepl+1]=MOD2CH2[l]

      Positron2gCoincidenceTimeD1[stepl/2]=Abs(TimeDataMOD2[2*l-2]-
TimeDataMOD2[2*l-1])
```

```
                        If( (Positron2gCoincidenceTimeD1[stepl/2] <= 1
))

      Positron2gCoincidenceTimeD[stepl2/2]=Positron2gCoincidenceTimeD1[
stepl/2]+1

      Positron2gCoincidenceReal[stepl2]=Positron2gCoincidence[stepl]

      Positron2gCoincidenceReal[stepl2+1]=Positron2gCoincidence[stepl+1
]
                        stepl2+=2
                  EndIf
            stepl+=2
             EndIf

      While (l < max2)

       MAKE/O/N=(max1)
MOD1CH0_HIST,MOD1CH1_HIST,MOD1CH2_HIST,MOD1CH3_HIST
       MAKE/O/N=(max2) MOD2CH1_HIST,MOD2CH2_HIST
       MAKE/O/N=(1000) Positron3gCoincidence_HIST
       MAKE/O/N=(stepk/4) Positron3gCoincidenceTimeD_HIST
       MAKE/O/N=(1000) Positron2gCoincidence_HIST
       MAKE/O/N=(stepl/2) Positron2gCoincidenceTimeD_HIST
       MAKE/O/N=(1000) Positron3gCoincidenceReal_HIST
       MAKE/O/N=(1000) Positron2gCoincidenceReal_HIST

       Histogram/B={1,1,700  } MOD1CH0,MOD1CH0_HIST
       Histogram/B={1,1,700   } MOD1CH1,MOD1CH1_HIST
       Histogram/B={1,1,700  } MOD1CH2,MOD1CH2_HIST
       Histogram/B={1,1,700   } MOD1CH3,MOD1CH3_HIST
       Histogram/B={1,1,700  } MOD2CH1,MOD2CH1_HIST
       Histogram/B={1,1,700  } MOD2CH2,MOD2CH2_HIST
       Histogram/B={1,1,1000  }
Positron3gCoincidence,Positron3gCoincidence_HIST
       Histogram/B={1,1,10000 }
Positron3gCoincidenceTimeD,Positron3gCoincidenceTimeD_HIST
       Histogram/B={1,3,200  }
Positron3gCoincidenceReal,Positron3gCoincidenceReal_HIST
       Histogram/B={1,1,1000 }
Positron2gCoincidence,Positron2gCoincidence_HIST

Histogram/B={1,1,10000}Positron2gCoincidenceTimeD,Positron2gCoincidence
TimeD_HIST
       Histogram/B={1,1,1000 }
Positron2gCoincidenceReal,Positron2gCoincidenceReal_HIST

       inputcountrate=(493.949*3485.19)/4550
       g3gcorrectionminus= inputcountrate* inputcountrate*2.39*10^-
8*493.949

g3gcorrectionplus=0.412*(Positron3gCoincidenceTimeD_HIST[0]+Positron3gC
oincidenceTimeD_HIST[1])
      //Print "The uncalibrated 3g/2g  Ratio is",stepk/(2*stepl)
```

```
      //Print "The near calibrated 3g/2g  Ratio
is",Positron3gCoincidenceTimeD_HIST[0]/Positron2gCoincidenceTimeD_HIST[
0]
      //Print "The calibrated 3g/2g  Ratio
is",(Positron3gCoincidenceTimeD_HIST[0]-
g3gcorrection)/Positron2gCoincidenceTimeD_HIST[0]
      Print "The Factor off from 1/372 is",
2.13*((Positron3gCoincidenceTimeD_HIST[0]+Positron3gCoincidenceTimeD_HI
ST[1])/(Positron2gCoincidenceTimeD_HIST[0]+Positron2gCoincidenceTimeD_H
IST[1]))/(1/372)
      Print "3 g count
",Positron3gCoincidenceTimeD_HIST[0]+Positron3gCoincidenceTimeD_HIST[1]
       Print "2 g count
",Positron2gCoincidenceTimeD_HIST[0]+Positron2gCoincidenceTimeD_HIST[1]
      Print stepk, stepl,g3gcorrectionplus,g3gcorrectionminus
      Killwaves /Z
basename0,basename1,basename2,basename3,basename4,basename5,basename6,b
asename7,Positron2gCoincidenceTimeD1,Positron3gCoincidenceTimeD1
      Close filenum
      End
```

Appendix F: GEANT4 Detector Geometry Construction

PositronCapillaryTubeDetectorConstruction.cc

```
// ********************************************************************
// * License and Disclaimer                                           *
// *                                                                  *
// * The  Geant4 software  is  copyright of the Copyright Holders  of *
// * the Geant4 Collaboration.  It is provided  under  the terms  and *
// * conditions of the Geant4 Software License,  included in the file *
// * LICENSE and available at  http://cern.ch/geant4/license .  These *
// * include a list of copyright holders.                             *
// *                                                                  *
// * Neither the authors of this software system, nor their employing *
// * institutes,nor the agencies providing financial support for this *
// * work  make  any representation or  warranty, express or implied, *
// * regarding  this  software system or assume any liability for its *
// * use.  Please see the license in the file  LICENSE  and URL above *
// * for the full disclaimer and the limitation of liability.         *
// *                                                                  *
// * This  code  implementation is the result of  the  scientific and *
// * technical work of the GEANT4 collaboration.                      *
// * By using,  copying,  modifying or  distributing the software (or *
// * any work based  on the software)  you  agree  to acknowledge its *
// * use  in  resulting  scientific  publications,  and indicate your *
// * acceptance of all terms of the Geant4 Software license.          *
// ********************************************************************
//

#include "PositronCapillaryTubeDetectorConstruction.hh"
#include "PositronCapillaryTubeElectricField.hh"
#include "PositronCapillaryTubeFieldMessenger.hh"
```

```
#include "G4Material.hh"
#include "G4Box.hh"
#include "G4Tubs.hh"
#include "G4LogicalVolume.hh"
#include "G4ThreeVector.hh"
#include "G4PVPlacement.hh"
#include "globals.hh"
#include "G4UniformMagField.hh"
#include "G4FieldManager.hh"
#include "G4TransportationManager.hh"
#include "G4SDManager.hh"
#include "G4RunManager.hh"


PositronCapillaryTubeDetectorConstruction::PositronCapillaryTubeDetecto
rConstruction()
:solidWorld(0),  logicWorld(0),  physiWorld(0),
 solidsilverTarget(0), logicsilverTarget(0), physisilverTarget(0),
 silverTargetMater(0), solidGoldTarget(0), logicGoldTarget(0),
physiGoldTarget(0),
 goldTargetMater(0),solidsilicaTarget(0), logicsilicaTarget(0),
physisilicaTarget(0),
 silicaTargetMater(0),solidBufferTarget(0), logicBufferTarget(0),
physiBufferTarget(0),
 BufferTargetMater(0), fEmFieldSetup(0),
 stepLimit(0),
 fWorldLength(0.),  capillarylength(0.)
 {
  ;
}

PositronCapillaryTubeDetectorConstruction::~PositronCapillaryTubeDetect
orConstruction()
{
  delete stepLimit;
  delete fEmFieldSetup ;

}

G4VPhysicalVolume*
PositronCapillaryTubeDetectorConstruction::Construct()
{

  //------------------------------------------------------ materials

  G4double a, z,density;
  G4int nel,natoms;

  //Elements to be used
  G4Element* H = new G4Element("Hydrogen", "H", z=1., a=1.0079*g/mole);
  G4Element* O = new G4Element("Oxygen"  , "O", z=8., a= 16.00*g/mole);
  G4Element* C = new G4Element("Carbon"  , "C", z=6., a= 12.01*g/mole);
  G4Element*Si=new G4Element("Silicon", "Si",z=14.,a=28.0855*g/mole);

  //Silica
```

```
  G4Material* Silica = new G4Material("Silica", density= 2634*kg/m3,
  nel=2);
  Silica->AddElement(Si, natoms=1);
  Silica->AddElement(O, natoms=2);


  //acrylate
  G4Material* Acrylate = new G4Material("Acrylate", density=
  1.15*g/cm3, nel=3);
  Acrylate->AddElement(C, natoms=3);
  Acrylate->AddElement(H, natoms=3);
  Acrylate->AddElement(O, natoms=2);


  //Silver
  G4Material* Ag = new G4Material("Silver", z=47., a= 107.8682*g/mole,
  density= 10.49*g/cm3);

  //Gold
  G4Material* Au = new G4Material("Gold", z=79., a= 196.966569*g/mole,
  density= 19.3*g/cm3);

  //Vacuum
  G4Material*Va=new G4Material("Vacuum",z=1.,a=1.*g/mole,
  density=.00000000001*g/cm3);

 // Print all the materials defined.
 //
  G4cout << G4endl << "The materials defined are : " << G4endl <<
  G4endl;
  G4cout << *(G4Material::GetMaterialTable()) << G4endl;

 //------------------------------------------------------ volumes

 //--------- Sizes of the principal geometrical components (solids)  --


  silverTargetMater  = Ag;
  silicaTargetMater=Silica;
  BufferTargetMater=Acrylate;
  goldTargetMater=Au;
  fWorldLength= 1.2 *m;


//--------- Definitions of Solids, Logical Volumes, Physical Volumes


// World

  G4double HalfWorldLength = 0.5*fWorldLength;

  solidWorld= new
  G4Box("world",HalfWorldLength,HalfWorldLength,HalfWorldLength);
  logicWorld= new G4LogicalVolume( solidWorld, Va, "World", 0, 0, 0);
```

```
  //  Must place the World Physical volume unrotated at (0,0,0).
  //
  physiWorld = new G4PVPlacement(0,               // no rotation
                                 G4ThreeVector(), // at (0,0,0)
                                 logicWorld,      // its logical volume
                          "World",         // its name
                                 0,               // its mother  volume
                                 false,           // no boolean
operations
                                 0);              // copy number

  //--------------------------------
  // Inner  (Cylinder) Silver Layer
  //--------------------------------

  G4double capillaryinnerradius=.75*mm;
  G4double capillaryoutersilverradius=.750025*mm;
  G4double capillarylength=15*cm;



 //--------------------------------
  // Inner  (Cylinder) Silica Layer
  //--------------------------------

  G4double capillaryoutersilicaradius=.7800*mm;

  G4ThreeVector positionTargetSilica = G4ThreeVector(0,0,0);

  solidsilicaTarget = new
G4Tubs("Silica",capillaryoutersilverradius,capillaryoutersilicaradius,c
apillarylength,0*deg,360*deg);
  logicsilicaTarget = new
G4LogicalVolume(solidsilicaTarget,silicaTargetMater,"SilicaTarget",0,0,
0);
  physisilicaTarget = new G4PVPlacement(0,               // no rotation
                          positionTargetSilica,  // at (x,y,z)
                          logicsilicaTarget,     // its logical volume

                          "SilicaTarget",        // its name
                          logicWorld,      // its mother  volume
                          false,           // no boolean operations
                          0);              // copy number



 //--------------------------------
  // Outer  (Cylinder) Buffer Layer
  //--------------------------------

  G4double capillaryouterbufferradius=.8500*mm;

  G4ThreeVector positionTargetBuffer = G4ThreeVector(0,0,0);
```

```
  solidBufferTarget = new
G4Tubs("Buffer",capillaryoutersilicaradius,capillaryouterbufferradius,c
apillarylength,0*deg,360*deg);
  logicBufferTarget = new
G4LogicalVolume(solidBufferTarget,BufferTargetMater,"BufferTarget",0,0,
0);
  physiBufferTarget = new G4PVPlacement(0,               // no rotation
                        positionTargetBuffer,  // at (x,y,z)
                        logicBufferTarget,     // its logical volume

                        "BufferTarget",        // its name
                        logicWorld,      // its mother  volume
                        false,           // no boolean operations
                        0);              // copy number



  //------------------------------
  // Outer  (Cylinder) Gold Layer
  //------------------------------

  G4double capillaryoutergoldradius=.850250*mm;

  G4ThreeVector positionTargetGold = G4ThreeVector(0,0,0);

  solidGoldTarget = new
G4Tubs("Gold",capillaryouterbufferradius,capillaryoutergoldradius,capil
larylength,0*deg,360*deg);
  logicGoldTarget = new
G4LogicalVolume(solidGoldTarget,goldTargetMater,"GoldTarget",0,0,0);
  physiGoldTarget = new G4PVPlacement(0,               // no rotation
                        positionTargetGold,  // at (x,y,z)
                        logicGoldTarget,     // its logical volume

                        "GoldTarget",        // its name
                        logicWorld,      // its mother  volume
                        false,           // no boolean operations
                        0);              // copy number


  return physiWorld;
}

//....oooOOOOOooo........oooOOOOOooo........oooOOOOOooo........oooOOOOO
ooo......

void
PositronCapillaryTubeDetectorConstruction::setTargetMaterial(G4String
materialName)
{
  // search the material by its name
  G4Material* pttoMaterial = G4Material::GetMaterial(materialName);
  if (pttoMaterial)
     {silverTargetMater = pttoMaterial;
      logicsilverTarget->SetMaterial(pttoMaterial);
```

```
        silicaTargetMater = pttoMaterial;
      logicsilicaTarget->SetMaterial(pttoMaterial);
        BufferTargetMater = pttoMaterial;
      logicBufferTarget->SetMaterial(pttoMaterial);
        goldTargetMater = pttoMaterial;
      logicGoldTarget->SetMaterial(pttoMaterial);
      G4cout << "\n----> The target is " << capillarylength/cm << " cm
of "
             << materialName << G4endl;
    }
}
```

Bibliography

1. Reinhard Krause-Rehberg, Hartmut Leipner. *Positron Annihilation in Semiconductors: Defect Studies.* New York : Springer, 1999.

2. R. Krause-Rehberg and H. Leipner. *Positron Annihilation in Semiconductors: Defect Studies.* s.l. : Springer .

3. *Positron Annihilation and Electrical Conduction of Irradiated Polymer.* S. Fujita, M. Baba, K. Shinyama, and T. Suzuki. Hachinohe : IEEE, 1995.

4. *Performance of three-photon PET imaging: Monte Carlo simulations.* Krzysztof Kacperski and Nicholas M Spyrou. s.l. : Phys. Med. Biol, 2005, Vol. 50. 5679-5695 .

5. Ross, Matthew. *Development and optimization of a positron annihilation lifetime spectrometer to measure nanoscale defects in solids and borane cage molecules in aqueous solution.* Dayton : s.n., 2008.

6. LLNL. *Antimatter helps to protect our nuclear stockpile.* s.l. : Science & Technology Review, 1998.

7. Williams. *Simulantious ACAR and 2D DBAR Applied to SiC.* s.l. : AFIT, 2010. Publication in process.

8. *Positronium Molecule Formation, Bose-Einstein Condensation and Stimulated Annihilation.* Mills, Allen. Riverside : Nuclear Instruments and Methods in Physics Research B, 2002, Vol. 192.

9. Adamson, Paul. *A General Quantum Mechanical Method to Predict Positron Spectroscopy.* 2007.

10. *Long-Lived States of Positronium in Crossed electric and Magnetic Fields.* Ackerman. 2, s.l. : Physical Review, 1996, Vol. 78.

11. *Study of positronium hydride with a simple wavefunction:Application to the Stark effect of PsH.* Sech,C. Le, Silvi, B. Paris : Chemical Physics, 1998, Vol. 236. 77-85.

12. Krane, Kenneth. *Introductory Nuclear Physics.* Hoboken : John Wiley & Sons, Inc, 1988.

13. *Defects in Semiconductors Observed by 2D-ACAR and by a Slow-Positron Beam.* S. Tanigawa, A. Uedono, and L. Wei. Varenna : NATO Advanced Research Workshop, 1993.

14. Jean, Mallon,Scrader. *Principles and Applications of Positron & Positronium Chemistry.* s.l. : Wolrd Scientific Publishing Co, 2003.

15. *Coherent Production of Positronium Atom by Photon.* Kunashenko, Yu. Tomsk : Natural Science, 2004.

16. Bridgman, Charles J. *Introduction to the Physics of Nuclear Weapons.* Belvoir : DTRA, 2001.

17. *Time Distribution of Positron Annihilation in Liquids and Solids.* R. E. Bell and R. L. Graham. Chalk River : Physical Review, 1953, Vol. 90. 4.

18. Charton, Humberson. *Positron Physics.* s.l. : Cambridge University Press, 2001.

19. *Calculation of Positron Binding to Silver and Gold Atoms.* V.A. Dzuba, V. V. Flambaum, and C. Harabati. Sydney : Physical Review A, 2000, Vol. 62. 042504.

20. *Work Functions for Positrons in Metals.* Hodges, Stott. 1, s.l. : Physical Review B, Vol. 7.

21. *Experimental studies on positronium negative ions.* Nagashima. s.l. : Nuclear Instruments and Methods in Physics Research B, 2007.

22. *Theory of Positron Annihilation in Solids.* Ferrell, Richad A. 3, College Park : Reviews of Modern Physics, 1956, Vol. 28.

23. *The Three-Photon Annihilation of Positrons and Electrons.* DeBenedetti, Siegal. 4, 1954, Vol. 94.

24. *Three-Photon Annihilation of an Electron-Positron Pair.* A. Ore and J. L. Powell. 11, Chicago : Physical Review, 1949, Vol. 75.

25. *Spin and Polarization Effects in the Annihilation of Triplet Positronium.* Drisko, R. M. 6, Pittsburgh : Physical Review, 1955, Vol. 102.

26. *Direct Quantitative Observation of the Three-Photon Annihilation of a Positron-Negatron Pair.* Basson. 3, s.l. : Physical Review, 1954, Vol. 96.

27. *New High-Precision Comparison of Electron and Positron g Factors.* Dyck,Schwinberg, Dehmelt. 1, Seattle : Physical Review Letters, 1987, Vol. 59.

28. *A multicell trap to confine large numbers of positrons.* Surko,Greaves. La Jolla : Radiation Physics and Chemistry, 2003, Vol. 68. 419-425.

29. *Practical Limits on Positron Accumulation and the Creation of Electron-Positron Plasmas.* Greaves,Surko. Agoura Hills : Non-Neutral Plasma Physics , 2002, Vol. IV.

30. *External Electric Field Effect on Positronium Formation in some Polar and Nonpolor Polymers at Different Temperatures.* R. Yu, Y. Ito, T. Suzuki, V. Shantarovich, and K. Kondo. Tsukuba : Chemical Physics, 2006, Vol. 327.

31. *Electric-Field Dependence of Positronium Formation in Liquids and Polymers.* C. Wang, K. Hirata, J. Kawahara, and Y. Kobayashi. 22, Tsukuba : Physical Review B, 1998, Vol. 58.

32. J. Shertzer,J. Ackermann, P. Schmelcher. *Positronium in Crossed Electric and Magnetic Fields:the Existance of Long-Lived Ground State.* Worcester : s.n., 2008.

33. Knoll, Glenn F. *Radiation Detection and Measurement.* Hoboken : John Wiley & Sons,Inc, 2000.

34. Associates, X-Ray Instrumentation. *DGF-4C User's Manual.* Newark : s.n., 2002.

35. Sulham, Clifford. *Special Nuclear Material Imaging Using a High Purity Germanium Double Sided Strip Detector.* Dayton : AFIT, 2007.

36. Rothenbush, Fred. *Improved Multinuclide Imaging of Special Nuclear Material Using a High Purity Germanium Double Sided Strip Detector.* Dayton : AFIT, 2005.

37. *Investigations of Positronium Formation and Destruction Using PsARS.* W. Kauppila, J. Edwards, E. Miller, T. Stein, and E. Surdutovich. Detriot : Nuclear Instruments and Methods in Physics Research B, 2006, Vol. 247.

38. *Positron Annihilation Lifetime Spectroscopy of Dodecaborate Cage Molecules in Aqueous Nitrate Solutions.* Williams,Slaughter,Burggraf,Ross, Adamson, Petrosky . Dayton : IEEE NSS, 2009.

39. *Positron Annihilation Lifetime Spectroscopy of Dodecaborate Cage Molecules in Aqueous Nitrate Solutions* . C. Williams, R. Slaughter, L. Burggraf, P. Adamson, M. Ross, and J. Petrosky. Dayton : IEEE, 2009.

40. *Performance of Three-Photon PET Imaging: Monte Carlo Simulations.* Kryzysztof Kacperski and Nicholas Spyrou. London : s.n., 2005.

41. *Long-Lived States of Positronium in Crossed Electric and Magnetic Fields.* J. Ackermann, J. Shertzer, and P. Schmelcher. 2, Jena : Physical Review letters, 1997, Vol. 78.

42. *Positron Binding to Atomic Silver.* G. Ryzhikh and J. Mitroy. Casuarina : J. Phys. B: At. Mol. Opt. Phys., 1998, Vol. 31.

43. *Localization of the Electromagnetic Field in the Vicinity of Gold Nanoparticles: Surface Modification of Different Substrates.* P. Atanasov, N. Nedyalkov, T. Sakai, and M. Obara. Yokohama : Applied Surface Science, 2007, Vol. 254.

44. *GEANT4 Developments and Applications.* J. Allison, et al. s.l. : IEEE, 2006.

45. *GEANT4- A Simulation Toolkit.* S. Agostinelli, et al. s.l. : Nuclear Instruments and Methods A, 2003, Vol. 506.

46. *Geant4 Low Energy Electromagnetic Models for Electrons and Photons,.* P. Nieminen, et al. Geneva : CERN, 1999.

47. *GePEToS : A Geant4 Monte Carlo simulation package for Positron Emission Tomography.* S. Jani, et al. s.l. : IEEE Transactions on Nuclear Science, 2003.

48. *Silver Nanoparticle Effects in Biological Samples.* Pavel, I. 2010 (Awaiting Publication).

49. *Synthesis and Study of Silver Nanoparticles.* S. Solomon, et al. 2, Philadelphia : Journal of Chemical Education, 2007, Vol. 84.

50. *Rapid Delevery of Silver Nanoparticles Into Living Cells by Electroporation for Surface-Enhanced Raman Spectroscopy* . J. Lin, R. Chen, S. Feng, Y. Li, Z. Huang, S. Xie, Y. Yu. Fuzhou : Journal of Biosensors and Bioelectrons, 2009, Vol. 25.

51. J. A. Creighton, C. G. Blatchford, M. G. Albrecht. 75, s.l. : J. Chem. Soc.,Faraday Trans., 1979, Vol. 2.

52. S. George, B. Yoon. *Material Matters: Nanoscale Surface Modification.* s.l. : Aldrich Chemistry, 2009.

53. *Total positron-impact ionization and positronium formation from the noble gases.* G Laricchia, P Van Reeth, M Szłui ´nska and J Moxom1. London : J. Phys. B: At. Mol. Opt. Phys, 2002, Vol. 35.

54. *Hydrogen in Crossed Fields.* Cederbaum. 9, s.l. : Physical Review, Vol. 49.

55. Adamson, Paul. *A General Quantum Mechanical Method to Predict Positron Spectroscopy.*

REPORT DOCUMENTATION PAGE

Form Approved
OMB No. 074-0188

1. REPORT DATE *(DD-MM-YYYY*	2. REPORT TYPE	3. DATES COVERED *(From – To)*
25-03-2010	Master's Thesis	Sep 2009-Feb2010

4. TITLE AND SUBTITLE
Positron Annihilation Ratio Spectroscopy (PsARS) Applied to Positronium Formation Studies

5a. CONTRACT NUMBER

5b. GRANT NUMBER

5c. PROGRAM ELEMENT NUMBER

6. AUTHOR(S)
Slaughter, Robert C., 2nd Lieutenant, USAF

5d. PROJECT NUMBER

5e. TASK NUMBER

5f. WORK UNIT NUMBER

7. PERFORMING ORGANIZATION NAMES(S) AND ADDRESS(S)
Air Force Institute of Technology
Graduate School of Engineering and Management (AFIT/EN)
2950 Hobson Way
WPAFB OH 45433-7765

8. PERFORMING ORGANIZATION REPORT NUMBER
AFIT/GNE/ENP/10-M07

9. SPONSORING/MONITORING AGENCY NAME(S) AND ADDRESS(ES)
M. Lindsay
United States Air Force Research Laboratory
Energetic Materials Branch (AFRL/RWMER)
2306 Perimeter Rd
Eglin AFB, FL 32542-5910

10. SPONSOR/MONITOR'S ACRONYM(S)
AFRL/RWMER

11. SPONSOR/MONITOR'S REPORT NUMBER(S)

12. DISTRIBUTION/AVAILABILITY STATEMENT
Approved For Public Release; Distribution Unlimited

13. SUPPLEMENTARY NOTES

14. ABSTRACT

A Positron Annihilation of Radiation Spectrometer (PsARS) was developed and characterized. PsARS spectroscopy as well as digital Positron Annihilation Lifetime Spectroscopy (PALS) was applied to measure positronium formation on gold manoparticles deposited through an evaporative method onto a thin capillary tube. This gold coated capillary tube was designed to be used for positronium lifetime studies in local electric field experiments. High local electric fields can polarize a positron-electron pair, which may result in an extended lifetime of the positron. These fields may be created through the interaction of an external electric field with silver manoparticles deposited onto the surface of gold coated capillary tubes. The capability to control size and distribution of silver manoparticles on such a surface is demonstrated. PsARS analysis of potassium dodecahydrododecaborate (dodecaborate) solutions was also performed to verify positronic dodecaborate species as well as potential positronium quenching.

15. SUBJECT TERMS
Positron, Positronium, Annihilation, PsARS.

16. SECURITY CLASSIFICATION OF:			17. LIMITATION OF ABSTRACT	18. NUMBER OF PAGES	19a. NAME OF RESPONSIBLE PERSON
a. REPORT	b. ABSTRACT	c. THIS PAGE			Dr . Larry W. Burggraf
U	U	U	UU	152	19b. TELEPHONE NUMBER *(Include area code)* 937-255-3636 X4507